MEMS-Tunable VCSELs-Driven Terahertz Emitters Based on Conventional and Nanoelectrode Photomixers

Dem Fachbereich Elektrotechnik und Informationstechnik
der Technischen Universität Darmstadt
zur Erlangung der Würde eines
Doktor-Ingenieurs (Dr.-Ing.)
genehmigte

Dissertation

von

M.Sc.
Mohammad Tanvir Haidar
geboren am 12.12.1981
in Gopalganj, Bangladesch

Referent:	Prof. Dr.-Ing. Franko Küppers
Korreferent:	Prof. Dr.-Ing. Dr. rer. nat. habil. Harald Schenk

Tag der Einreichung:	21.06.2017
Tag der mündlichen Prüfung:	20.12.2017

D17
Darmstadt 2017

Haidar, Mohammad Tanvir: MEMS-Tunable VCSELs-Driven Terahertz Emitters Based on Conventional and Nanoelectrode Photomixers
Darmstadt,Technische Universität Darmstadt,
Jahr der Veröffentlichung der Dissertation auf TUprints: 2018
URN: urn:nbn:de:tuda-tuprints-000
Tag der mündlichen Prüfung: 20.12.2017

Acknowledgements

I am indebted to many people whose active support helped me to pursue this dissertation. First and foremost, I convey my heartfelt gratitude to Prof. Dr.-Ing. Franko Küppers who gave me the opportunity to work with the "LOEWE Sensors Towards Terahertz" program. It was not an easy decision to leave my early career in the industry, but his later support and mentoring soon authenticated my decision.

The successful completion of my project could not be possible without the contribution and supervision of Prof. Dr. rer. nat. Sascha Preu. I am blessed to work with him, and his excellence in almost every fields enriched me with real knowledge. I convey my gratitude to apl. Prof. Dr.-Ing. Rainer Michalzik from Ulm University, his excellent teaching and mentoring during my M.Sc. studies had enthused me working with VCSELs.

I would like to thank Dr.-Ing. Christian Gierl and Dr.-Ing. Holger Maune for the cooperation on different occasions. I am indebted to Andreas Semrad and also to Peter Kießlich, without their support my work would always be with paper and pencil. I would like to thank my colleagues Dr. habil. Arkadi Chipouline, Dr.-Ing. Ali Emsia, Dr. Quang Trung Le, Sujoy Paul, and Dr.-Ing. Karolina Zogal. Special thanks go to my other colleagues Julijan Cesar, Dr.-Ing. Shihab Al-Daffaie, Ahid S. Hajo, Mohammadreza Malekizandi, and PD Dr.-Ing. habil. Oktay Yilmazoglu who continuously cooperated me till the end. I also remember the cooperation of Maria Kaiser, Traudel Micus, and Dipl.-Ing. Eleonore Titow.

Lastly, my gratitude goes to my mother, my brothers and my wife for supporting me for what I am today. My father passed away in 2007, and he was my source of all enthusiasms. Today could have been the best day if he were by my side again.

Weiterstadt, 21.06.2017 Mohammad Tanvir Haidar

Erklärung laut §9 PromO

Ich versichere hiermit, dass ich die vorliegende Dissertation allein und nur unter Verwendung der angegebenen Literatur verfasst habe. Die Arbeit hat bisher noch nicht zu Prüfungszwecken gedient.

Weiterstadt, 21.06.2017

Kurzfassung

Kompakte, weit abstimmbare und modensprungfreie Laser werden für Dauerstrich-(CW) Terahertz-(THz) Quellen benötigt. Diese Arbeit beschreibt zum ersten Mal die Leistungsfähigkeit von mikroelektromechanisch abstimmbaren oberflächenemittierenden Lasern (MEMS-VCSEL) bei 1550 nm für den Einsatz in abstimmbaren CW-THz Photomischer-Systemen. Ein elektrothermisch abstimmbarer MEMS-VCSEL, mit einem Abstimmbereich von 64 nm (7,92 THz) und einer Seitenmodenunterdrückung (SMSR) von > 50 dB über den gesamten Abstimmbereich wurde mittels einer optischen Heterodyn-Methode in Verbindung mit einem Laser mit verteilter Rückkopplung (DFB) zum Treiben eines Photomischers verwendet. Die erreichte THz-Bandbreite von 4,74 THz wird nur durch den verwendeten Photomischer begrenzt. Diese Dissertation charakterisiert systematisch MEMS-VCSEL mit einem besonderen Augenmerk auf die relevanten Parameter des THz-Photomischens wie Abstimmbarkeit, Abstimmgeschwindigkeit, Linienbreite, Polarisation und Wellenlängenstabilität. MEMS-VCSEL zeigen eine ausgezeichnete Polarisationsunterdrückung (PSR) von > 20 dB und Linienbreite von < 50 MHz über den gesamten Abstimmbereich. Wegen der freihängenden Struktur des beweglichen Resonatorspiegels zeigen MEMS-VCSEL Wellenlängendrifts und –schwankungen. Eine Wellenlängenregelschaltung kompensiert die langsamen Drifts, während die schnellen Schwankungen eine Langzeitbandbreite von < 350 MHz aufweisen und somit für THz-Photomischen ausreichen. Die Schwankungen hängen von den mechanischen Eigenschaften des beweglichen Spiegels ab und werden in dieser Arbeit analysiert.

Das kleine aktive Volumen der VCSEL führt zu einer Ausgangsleistung von wenigen Milliwatt. Diese Arbeit untersucht weiterhin Nanoelektroden-basierte CW-Photomischer mit einem hohen Umwandlungswirkungsgrad der optischen Leistung in THz-Leistung. Diese Bauelemente haben etwa eine Größenordnung kleinere Bauelement-Kapazität im Vergleich zu einem herkömmlichen Photomischer mit Interdigitalelektroden, um die Verluste zu reduzieren und die Ausgangsleistung zu verbessern. Die Photomischer haben das Potential, einen ausreichenden Photostrom zu erzeugen, wenn ein VCSEL den 1 µm–2 µm großen Elektrodenabstand durch ein Linsensystem intensiv beleuchtet. Bei dieser Untersuchung wurde die

Dielektrophoresen-Technik (DEP) verwendet, um Silber-Nanodrähte als Nanoelektroden auszurichten und Photomischer bei 850 nm und 1550 nm mit entsprechenden Substratmaterialien herzustellen. Während die DC-Eigenschaften vielversprechend sind, konnte bisher kein THz-Signal aufgrund der ungeschützten Nanodrähte erzeugt werden. Die Arbeit schließt mit einer detaillierten Analyse der Fehlermechanismen und möglichen Lösungsvorschlägen ab.

Abstract

Continuous-wave (CW) terahertz (THz) photomixing setups require compact, widely tunable mode-hop-free driving lasers. This thesis reports, for the first time, on the performance of surface micromachined single-mode microelectromechanical system (MEMS)-tunable vertical-cavity surface-emitting lasers (VCSELs) around 1550 nm for application in a tunable THz CW photomixing system. An electrothermally tunable MEMS-VCSEL featuring a tuning range of 64 nm (7.92 THz) with a side-mode-suppression-ratio of > 50 dB over the entire tuning range is optically heterodyned with a distributed feedback (DFB) laser diode to drive the photomixing setup. The achieved THz bandwidth of 4.74 THz is yet only limited by the employed photomixers. This thesis addresses a systematic characterization of MEMS-VCSELs with a particular focus on the parameters relevant for THz photomixing, such as tunability, tuning speed, linewidth, polarization and wavelength stability. MEMS-VCSELs have excellent polarization-suppression-ratio of > 20 dB and a linewidth of < 50 MHz, respectively over the entire tuning range. Due to the suspended structure of the MEMS-tunable mirror, MEMS-VCSELs show wavelength drifts and fluctuations. A wavelength control circuit compensates the slow drifts while the fast fluctuations show a long-time-scale bandwidth of < 350 MHz which is still sufficient for THz photomixing. The fluctuations are functions of the mechanical properties of the tunable mirror and analyzed in this thesis.

The small active volume of VCSELs results in a low output power of few milliwatts. This thesis investigates the development of nanoelectrode-based CW photomixers with high optical to THz conversion efficiency. These devices have an order of magnitude lower capacitance to reduce the losses and improve the output power as compared to conventional interdigitated electrode structures. The photomixers have potential to produce sufficient photocurrent when VCSELs intensely illuminate the 1 µm–2 µm electrode gaps through lens systems. We first utilize dielectrophoresis technique to align silver nanowires as nanoelectrodes to fabricate the photomixers at 850 nm and 1550 nm using corresponding substrate materials. While DC characteristics look promising, so far no THz signal is generated due to the failure of the unprotected nanowires. The thesis concludes with a detailed analysis of the failure mechanisms with prospective solutions.

Contents

1 Introduction

The structure common to most vertical-cavity surface-emitting lasers (VCSELs) consists of two highly reflective distributed Bragg reflector (DBR) mirrors sandwiching a thin active gain region [1]. VCSEL was first suggested by Prof. Kenichi Iga in 1977, and GaInAsP/InP-based device at 1300 nm was first demonstrated by Soda et al. in 1979 [2]. The first room-temperature, continuous-wave (CW) operating GaAs-based VCSEL around 850 nm was demonstrated in the late 1980s by the same group [3]. Since then, VCSELs have been a topic of pioneer research and electrically driven CW operating VCSELs were reported in the wavelength range of 670 nm [4], 980 nm [5] and 1550 nm [6] to mid-infrared [7].

Figure 1.1 schematically shows the device structure of a conventional edge-emitting laser (EEL) and a VCSEL for comparison. The small cavity volume of VCSELs provides some advantages, such as ultralow threshold operation and low power consumption. Besides, they have single longitudinal mode operation with a low divergent circular beam leading to high fiber coupling efficiency [1, 8]. The stimulated emission perpendicular to the wafer surface enables the wafer-scale testing, easy bonding and mounting, as well as the small footprint of the VCSELs, leads to low fabrication cost and also easy fabrication into one-dimensional (1-D) and two-dimensional (2-D) arrays [8, 9]. Since the first commercialization of VCSELs by Honeywell in 1996, fixed cavity length VCSELs at different spectral bands have made their ways for a broad range of applications. Those include, for instance, short-range optical communication systems, high-speed local area networks (LANs), optical interconnects in data centers, laser mice, printers, active optical cables (AOC), mid board optical modules (MBOM), and embedded optical modules (EOM) [1, 10]. In the coming years, VCSELs are expected to contribute significantly in the area of displays, illuminations, optical sensing, optical information processing, and optical memory [1].

The invention of Erbium-doped fiber amplifier (EDFA) by the Southampton University group had changed the communications world first to introduce the wavelength division multiplexing (WDM) and later the dense WDM (DWDM) which had exploded the capacity of the backbone fiber systems [11]. Though GaAs-based 850 nm

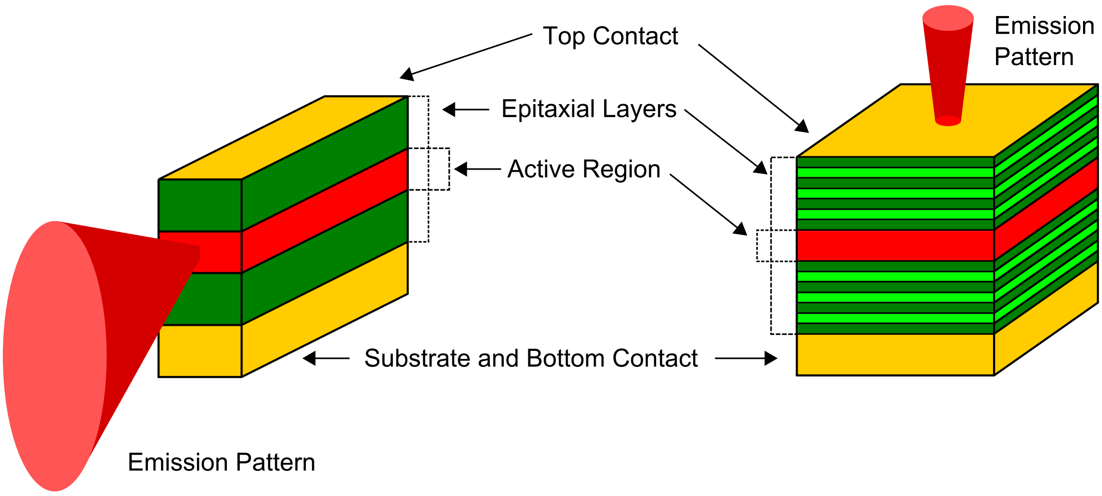

Figure 1.1: Device structures of EEL (left) and VCSEL (right).

VCSELs are intensively used in the short-range optical communication systems, notably for 10-Gbit/s Ethernet and high-performance computing systems (HPC), their multimode characteristics make them incompetent for the WDM/DWDM applications. However, DWDM transmitters require several fixed wavelength lasers closely spaced in wavelengths and also thermoelectric coolers to maintain wavelength stability [11]. This necessarily makes the whole system architecture complex. Thus it has been a long-sought to replace all those lasers by a single-mode, WDM-ready, broadband tunable laser source. Because of the large availability of optical components around 1550 nm, long-wavelength VCSELs became popular candidates for mode-hop-free broadband, CW tuning by utilizing their inherent longitudinal single-mode behavior. For the realization of such tunable VCSELs, one of the mirrors, e.g., the top mirror of a fixed cavity VCSEL is replaced by a microelectromechanical system (MEMS)-tunable mirror. Actuation of the MEMS component of the top mirror by electrothermal [12], electrostatic [13] or piezo-electric force [14], the resonator length, i.e., the emission wavelength can be changed. MEMS-tunable mirrors are typically cantilever [14] or membrane structures [15] utilizing high-contrast gratings (HCGs) [16] or DBRs [12]. By utilizing the surface micromachining technique, such a mirror membrane can be fabricated directly on top of a half-VCSEL structure consisting of the bottom DBR and thin active region [12]. Our group had demonstrated such surface micromachined electrically pumped 1550 nm MEMS-tunable VCSELs (MEMS-VCSELs) with CW mode-hop-free broadband tuning of $>$ 100 nm [12, 17]. Besides the optical communication systems as stated above, the transversal and longitudinal single-mode behavior of MEMS-VCSELs are very attractive for the applications in gas spectroscopy [18, 19, 20] and fiber-Bragg-grating sensors [21]. In addition to these established fields, this thesis deals with the application in terahertz (THz) photomixing systems using surface micromachined 1550 nm electrothermally MEMS-tunable VCSELs (MEMS-VCSELs).

THz applications between 100 GHz and 10 THz include non-invasive medical imaging, future high-frequency communications, spectroscopy, homeland security, earth, and space science among many other fields [22, 23]. Four major approaches generating THz sources are optical rectification, photomixing, semiconductor-based THz sources, i.e., quantum cascade laser (QCL), and solid-state electronics devices [22]. For applications where a large frequency coverage of up to several THz or a high spectral resolution is required, THz generation by heterodyne photomixing of two CW lasers is commonly used [24]. THz generation of < 50 GHz by photomixing of an optical beat in a photoconductive antenna (PCA) was first demonstrated by Brown and his colleagues in 1993 [25]. With the remarkable development of ultrafast photodiodes (PDs) [26], THz generation by heterodyne photomixing of several THz became possible. Figure 1.2 schematically shows a heterodyne photomixing setup where at the front end, an ultra-fast PD as transmitting photomixer (Tx) down-converts the optical beat note between two lasers at frequencies of ν_1 and $\nu_2 = \nu_1 + \nu_{\mathrm{THz}}$ into an alternating current (AC) component oscillating at ν_{THz} [26]. A suitably designed on-chip antenna converts that AC component into a free-space THz radiation. For detection, a receiving photomixer (Rx) mixes the received THz signal with the optical envelope of the beat signal that was previously used for THz generation, leading to a down-conversion of the THz field to a DC photocurrent as a read-out signal.

The unique advantage of photomixing systems is their inherently large tuning range: at 1550 nm (850 nm), one THz corresponds to a detuning of the two lasers by only about 8 nm (2.4 nm), i.e., by 0.52 % (0.28 %), achievable with many laser concepts. The large-scale availability of optical components around 1550 nm facilitates inexpensive generation of THz compared to established 850 nm systems. Telecom-wavelength compatible THz photomixers [27, 28, 29] represent an ideal optical-to-RF converter for this purpose. To fully exploit the frequency coverage of the photomixers, lasers with a broad tuning range of at least 3 THz, potentially 5 THz, are required [27]. The most common, compact choice are commercial narrow linewidth telecom wavelength lasers, such as the distributed feedback (DFB) laser diodes where tuning is achieved by temperature adjustment. However, telecom DFB lasers are typically tunable by about 0.6 THz [30]. By appropriate selection of the individual wavelengths, it has been shown that three such diodes are indeed sufficient covering a frequency span of up to 3 THz [30]. Larger spans would require even more diodes. Further, the system has to be reconfigured when another set of diode pairs is used, aggravating performing a broad frequency scan. An alternative

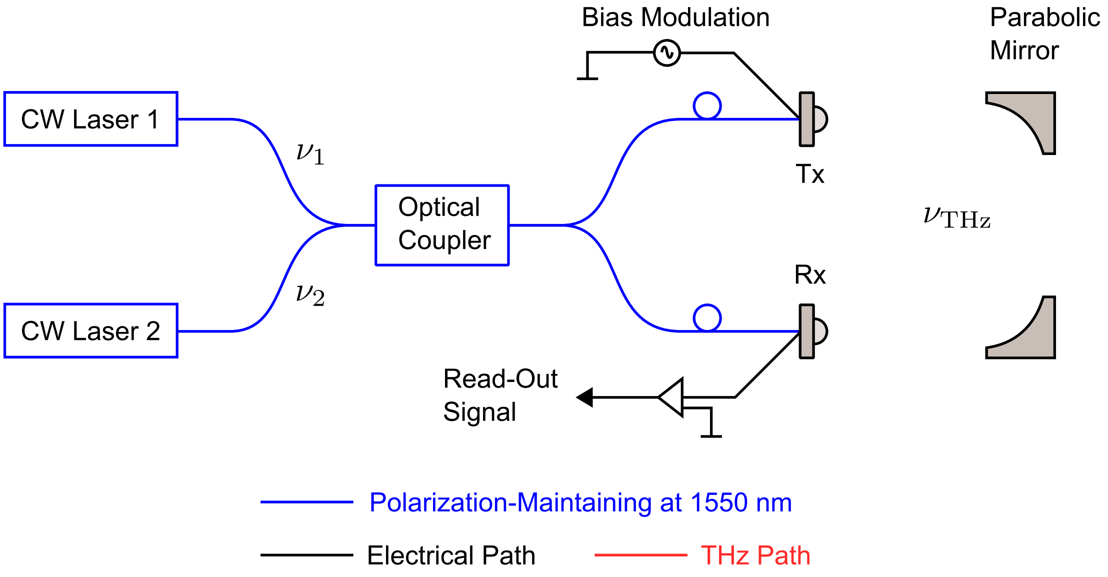

Figure 1.2: Schematic of heterodyne CW photomixing setup.

is grating tuned sources [31]. Due to the requirement of an external grating, these lasers are fairly bulky with little potential for chip-sized integration. Recent developments in compact semiconductor lasers may solve this issue in future THz systems. Such lasers include, e.g., sampled grating distributed Bragg reflector (SG-DBR) laser diodes [32], Y-branch laser diodes [33], and MEMS-VCSELs [34]. The latter are developed towards THz applications in this thesis.

1.1 Motivation

It is evident that compact, widely tunable mode-hop-free driving lasers will benefit CW THz signal generation by heterodyne photomixing process. Key parameters of MEMS-VCSELs important for the THz photomixing system are compared to those of DFB lasers employed in commercial CW THz photomixing systems from TOPTICA Photonics [35] and are listed in Tab 1.1. MEMS-VCSELs featuring electrothermal tuning range of several 10 nm, i.e., several THz [12, 17, 36] excel the tuning range of DFB lasers (2 nm–5 nm) [30, 35]. The single-mode behavior is characterized by the side-mode-suppression-ratio (SMSR) which is of > 50 dB for the presented MEMS-VCSELs over the entire tuning range. Compared to the slow thermal tuning of DFB lasers (25 GHz/s), the electrothermal tuning speed of MEMS-VCSELs (entire tuning range in < 10 ms) is quite faster pronouncing the photomixed bandwidth

Table 1.1: Key parameters for lasers requried for CW THz photomixing system.

Key Parameter	MEMS-VCSELs	DFB Lasers [30, 35]
Tuning Range	64 nm–81 nm	2 nm–5 nm
Single-Mode Behavior	SMSR $>$ 50 dB	SMSR $>$ 50 dB
Tuning Speed	Entire Tuning Range in $<$ 10 ms	25 GHz/s
Emission Linewidth	$<$ 50 MHz	500 kHz–5 MHz
Polarization Stability	Stable	Highly Stable
Wavelength Stability	Drifts/Fluctuations	Fairly Stable
Optical Output Power	$<$ 3 mW	10 mW–100 mW

scanning with an unprecedented rate. As outlined in the preceding section, SG-DBR or Y-branch lasers also show broadband tunability, however, the corresponding thermal tuning is much slower than the electrothermal tuning of MEMS-VCSELs. The other inherent advantages, such as small-footprint, on-wafer testing, simple coupling to fiber, low power consumption, easy bonding, and packaging make MEMS-VCSELs much more attractive than the SG-DBR or Y-branch lasers.

Three of the key features of the constituting laser diodes deployed in CW THz photomixing systems are emission linewidth, polarization stability, and wavelength stability. In this thesis, these key parameters of MEMS-VCSELs for THz photomixing applications are particularly evaluated, characterized, and tailored to the experimental needs. On the one hand, MEMS-VCSELs show excellent polarization stability which is required for the THz photomixing system. On the other hand, few tens of MHz linewidth of MEMS-VCSELs is sufficient for this kind of application. In contrast, the major challenge for the THz photomixing system is the wavelength drifts and fluctuations of MEMS-VCSELs. These arise from the suspended top DBR mirror structure of MEMS-VCSELs which reacts to acoustic noises causing drifts in observed wavelength as well as the natural Brownian motion of the mirror itself giving rise to fast frequency fluctuations. However, a wavelength control circuit is implemented compensating the unwanted wavelength variation to a level sufficient for the THz photomixing system.

The goal of this work is to demonstrate a miniaturized tunable THz photomixing system benefitting from the unprecedented tuning bandwidth of MEMS-VCSELs with fast tuning speed. Since MEMS-VCSELs typically emit only a few mW of output power, I have parallelly worked on developing nanoelectrode-based CW THz photomixers [37] with improved optical to THz conversion efficiency. These devices are realized by dielectrophoretically aligned silver nanowires as nanoelectrodes. Two of the major benefits of such devices are their small capacitances as well as their ability to be driven by the low optical power of VCSELs. With the successful development of these CW THz photomixers, the hope for implementing MEMS-VCSELs-based miniaturized THz photomixing setup is the key goal of this thesis.

1.2 Thesis Overview

The thesis is structured as follows:

Chapter two reviews theoretical fundamentals of VCSELs. Few important output characteristics of fixed cavity VCSELs are displayed in light with the discussed theory for the later understanding of the behavior of MEMS-VCSELs with CW tuning.

Chapter three addresses a systematic characterization of MEMS-VCSELs with a particular focus on the key parameters required for application in tunable THz photomixing. These include broadband tuning characteristics, spectral purity, linewidth analysis, wavelength stability, and polarization stability.

Chapter four discusses theoretical fundamentals for photomixing and THz signal generation. The following sections report ultra-broadband tunable THz system where a CW photomixer is either driven by a MEMS-VCSEL and a fixed cavity VCSEL or by a MEMS-VCSEL and a DFB laser. The direct power detection with a Schottky diode or homodyne field detection with a photoconductor cover several THz and directly benefit from the unprecedented bandwidth of MEMS-VCSELs.

Chapter five discusses the fabrication of nanoelectrodes-based CW photomixers (NW-photoconductors) where dielectrophoresis technique aligns silver nanowires as nanoelectrodes. While characterizing, these devices fail due to the failure of silver nanowires, and thus, detailed failure mechanisms are explained in this chapter followed by prospective solutions.

Chapter six concludes the work with a highlight on achieved goals and provides an outlook towards the implement of miniaturized tunable THz photomixing setup based on MEMS-VCSELs.

2 Theoretical Fundamentals

This chapter begins with the amplitude and resonance condition required for the self-stimulated laser oscillation at an example of a Fabry-Pérot laser cavity. Fundamental theories for VCSELs are covered, and a short overview of the major output characteristics of a fixed cavity VCSEL is displayed. In the last part of this chapter, theoretical fundamentals of transverse mode resonators are presented related to the basic structure of tunable cavity VCSELS, i.e., MEMS-VCSELs presented in this work.

2.1 Fabry-Pérot Resonator

In a laser resonator, a supply of energy to the active layer by pumping with light or by an electric current can cause amplification [38]. The following self-sustained oscillation or laser action can be produced by providing feedback with two plane mirrors. Figure 2.1 shows a schematic of such a Fabry-Pérot resonator illustrating the propagation of monochromatic plane waves with the complex propagation

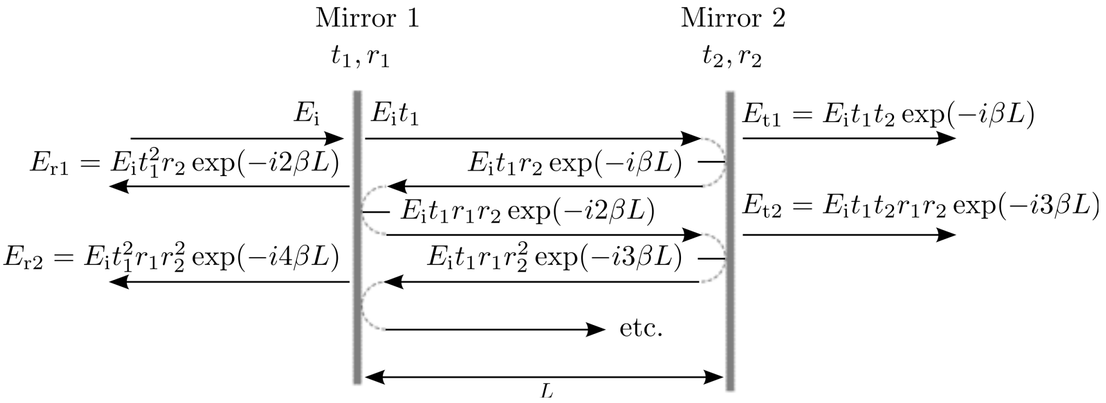

Figure 2.1: Schematic of Fabry-Pérot resonator illustrating superposition of transmitted and reflected waves [38].

constant β. The two mirrors are spaced at a geometrical distance of L defining the resonator length. The amplitude reflection coefficients for the two mirrors are r_1 and r_2, respectively, whereas t_1 and t_2 denote the corresponding amplitude transmission coefficients. An incident wave with the complex amplitude E_i is partially reflected by the first mirror, whereas the transmitted one enters the resonator encountering many times reflections at these two mirrors. By using superposition principle, the resultant transmitted wave with the complex amplitude E_t can be written as [38]

$$E_\mathrm{t} = E_\mathrm{i} \frac{t_1 t_2 \exp(-i\beta L)}{1 - r_1 r_2 \exp(-i2\beta L)}, \tag{2.1}$$

with

$$\beta = \frac{2\pi n}{\lambda} - i\frac{\alpha}{2}, \tag{2.2}$$

given by the spatial averages of the intensity attenuation coefficient, α and refractive index, n. The real part of β is known as wavenumber, k. In the limiting case when the denominator of Eq. (2.1) becomes zero, a finite amplitude incident wave produces an infinitely large amplitude transmitted wave (or reflected wave in Fig. 2.1) [38]. By considering that E_i is generated inside the resonator, the sustained propagation of $E_\mathrm{i} t_1 t_2 \exp\{-i\beta L\}$ is possible by means of a feedback as in the denominator of Eq. (2.1). Based on this discussion, the self-stimulation condition for the laser oscillation is

$$r_1 r_2 \exp\big(-i2\beta L\big) = 1. \tag{2.3}$$

Inserting Eq. (2.2) in Eq. (2.3), one obtains

$$r_1 r_2 \exp\big(-\alpha L\big) \exp\big(-i4\pi n L/\lambda\big) = 1. \tag{2.4}$$

Since Eq. (2.4) represents the feedback to sustain lasing, it must reproduce the amplitude and phase to replicate E_i after one complete roundtrip through the resonator. We, therefore, express α as the sum of the gain g of the laser transition and inrinsic loss coefficient, α_i so that,

$$\alpha = \alpha_\mathrm{i} - g. \tag{2.5}$$

Inserting this in Eq. (2.4) and comparing the magnitude gives the amplitude condition of

$$r_1 r_2 \exp\big[\,(g - \alpha_\mathrm{i})\,L\big] = 1. \tag{2.6}$$

The imaginary part (phase) of Eq. (2.4) should be an integer multiple of 2π constituting the resonance condition

$$4\pi n L/\lambda_\mathrm{q} = 2\pi q \quad \text{with} \quad q = 1, 2, 3, \ldots \tag{2.7}$$

or,

$$L = q \cdot \frac{\lambda_\mathrm{q}}{2n}. \tag{2.8}$$

Equation (2.8) determines the permissible wavelengths λ_q for the resonator fulfilling the resonance condition and termed as the eigenmodes of the system. The index q represents the longitudinal/axial mode order of the resonator. The value of q gives the number of half wavelengths fitting into the resonator. The threshold gain of the laser is obtained from Eq. (2.6) as

$$g_\mathrm{th} = \alpha_\mathrm{i} + \frac{1}{L}\ln\left(\frac{1}{r_1 r_2}\right) = \alpha_\mathrm{i} + \frac{1}{L}\ln\left(\frac{1}{\sqrt{R_1 R_2}}\right), \tag{2.9}$$

with intensity reflection coefficient $R_{1,2} = |r_{1,2}|^2$. The mode spacing between two neighboring longitudinal modes is known as the free spectral range (FSR) which is given in the wavelength domain by,

$$\lambda_\mathrm{q} - \lambda_\mathrm{q+1} = FSR_\lambda \approx \frac{\lambda_\mathrm{q}^2}{2nL} = \frac{\lambda_\mathrm{q}^2}{2L_\mathrm{opt}} \tag{2.10}$$

with $nL = L_\mathrm{opt}$ as the optical resonator length. Likewise, the FSR in the frequency domain is given by,

$$FSR_\nu = \frac{c}{2L_\mathrm{opt}}, \tag{2.11}$$

with c as the speed of the light in the medium. Instead of n, as a matter of fact, the spatial average of the group refractive index

$$n_\mathrm{gr} = n - \lambda\frac{dn}{d\lambda} \tag{2.12}$$

should be used elsewhere. The second term in Eq. (2.12) is known as the material dispersion which we will neglect unless otherwise stated.

We have, so far, discussed the founding equations of the Fabry-Pérot resonator. In Sec. 2.2, we will make use of these equations for a fixed cavity length VCSEL.

2.2 Vertical-Cavity Surface-Emitting Lasers

2.2.1 Relative Confinement Factor

The plane-parallel Fabry-Pérot resonator described in Sec. 2.1 has infinite lateral directions. Such a resonator does not exist in reality, and mostly all of the practical

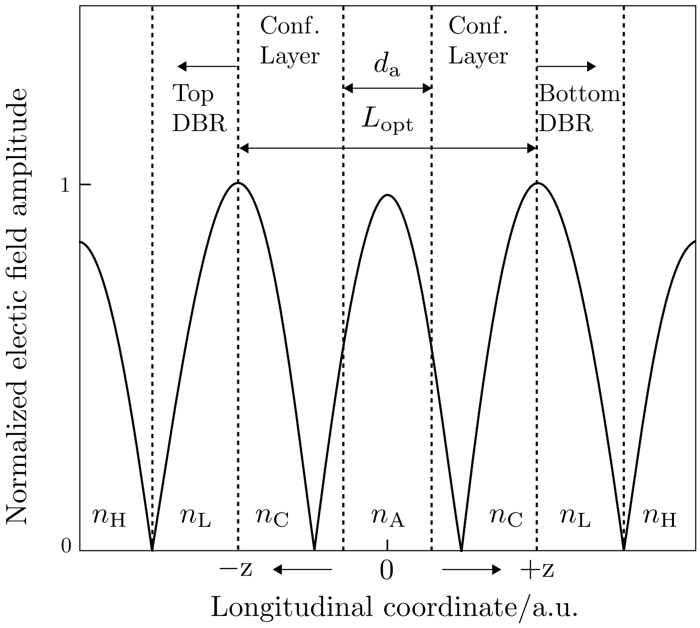

Figure 2.2: Schematic of a simplified fixed cavity length VCSEL structure with active gain layer thickness, d_a. Spatial distribution of the normalized electric field amplitude are also exemplarily shown [39].

resonators have mirrors with limited lateral sizes with circular or rectangular symmetry. Fig. 2.2 schematically shows a simplified structure of a fixed cavity length VCSEL consisting of few nanometers thick multi-quantum well (MQW) layers active gain medium and two highly reflective DBRs of limited lateral sizes. The reflected waves from the DBRs form a standing wave pattern along the resonator optical length of L_{opt} where maxima of the electric field amplitude are obtained at both ends of it. For optimum coupling between the electrons and photons, the active layer with thickness d_a should be placed in an antinode of the standing wave pattern. Note that, splitting of the active region into segments separated by $\lambda/2n$ must be avoided, otherwise carrier injection efficiency would suffer due to the poor overlap with the standing wave pattern [39]. Taking this into account, the shortest symmetric cavity for the VCSEL structure would be one wavelength thick with $q = 2$ in Eq. (2.8),

$$L = \frac{\lambda_q}{n}. \tag{2.13}$$

In an EEL, the active gain medium extends over the full cavity length. In contrast, the size of the MQW structure, d_a in the VCSEL structure is smaller than the total resonator (cavity) length of L_{opt}, requiring the remaining cavity to be enclosed by higher bandgap layers termed as carrier confinement layers. The lower refractive indexes of these layers ensure optical confinement. Based on this fact, the interaction of the thin MQW layers to the standing wave of the electric field inside the cavity plays a vital role. The average gain seen by the lasing mode generally termed as the confinement factor, $\mathit{\Gamma}$ which is the ratio of the volume of active region, V_a to that of the cavity mode, V_p. For a three-dimensional resonator structure, $\mathit{\Gamma}$ is written as

$$\mathit{\Gamma} = \mathit{\Gamma}_\mathrm{xy} \cdot \mathit{\Gamma}_\mathrm{z} = \frac{V_\mathrm{a}}{V_\mathrm{p}}, \tag{2.14}$$

where $\mathit{\Gamma}_\mathrm{xy}$ and $\mathit{\Gamma}_\mathrm{z}$ represent the lateral and longitudinal confinement factors, respectively. The lateral confinement factors equal to unity due to the large dimensions compared to the longitudinal direction. In the present case, the longitudinal confinement factor ($\mathit{\Gamma} \approx \mathit{\Gamma}_\mathrm{z}$) is given by the ratio of the active layer thickness to the total cavity length as [40],

$$\mathit{\Gamma}_\mathrm{z} = \frac{\int_{d_\mathrm{a}} \mid E\left(z\right) \mid^2 \mathrm{d}z}{\int_{L} \mid E\left(z\right) \mid^2 \mathrm{d}z}, \tag{2.15}$$

with the electric field $E(z)$ of the standing wave given by

$$E(z) = E_0 \cos\left(kz\right). \tag{2.16}$$

To evaluate Eq. (2.16), we need to consider the integrals over one period with appropriate multiplication factor. If d_a is composed of MQW layers with individual quantum well (QW) thickness of t, the multiplication factor for the numerator will be d_a/t, similarly, for the denominator, this would be $L/(\lambda/2)$ [40]. For a VCSEL with MQW layers, Eq. (2.15) then becomes

$$\mathit{\Gamma}_\mathrm{z} = \frac{\frac{d_\mathrm{a}}{t} \int_{d_\mathrm{a}} \cos^2\left(kz\right) \mathrm{d}z}{\frac{L}{\lambda/2} \int_{\lambda/2} \cos^2\left(kz\right) \mathrm{d}z}. \tag{2.17}$$

After integration, this expression yields,

$$\mathit{\Gamma}_\mathrm{z} = \frac{d_\mathrm{a}}{L} \left\{ 1 + \frac{\sin\left[\pi\left(\frac{t}{\lambda/2}\right)\right]}{\pi\left(\frac{t}{\lambda/2}\right)} \right\} = \frac{d_\mathrm{a}}{L} \mathit{\Gamma}_\mathrm{r}. \tag{2.18}$$

Therefore, the relative confinement factor or gain enhancement factor is defined by

$$\mathit{\Gamma}_r = \left\{ 1 + \frac{\sin\left[\pi\left(\frac{t}{\lambda/2}\right)\right]}{\pi\left(\frac{t}{\lambda/2}\right)} \right\}. \tag{2.19}$$

For each QW layer ($d_\mathrm{a} = \sum t$) placed along the electric field maxima, the optical amplification can be doubled, i.e., $\Gamma_\mathrm{r} \rightarrow 2$. For the active medium with the thickness equal to an integer multiple of half-wavelength e.g., $d_\mathrm{a} = q\lambda / (2n)$ as in EELs, one obtains $\Gamma_\mathrm{r} = 1$.

2.2.2 Distributed Bragg Reflectors

Due to the short optical cavity of the VCSELs, highly reflective DBRs are required. The DBR consists of a number of quarter-wave layers in an alternating sequence with high and low refractive indexes. To retain the optical confinement, the first layer, as seen from the carrier confinement layer in the VCSEL cavity has to be with low refractive index of n_L, as shown in Fig. 2.2. In order to achieve high reflectivities, an integer multiple of layer pairs is required, which finally terminates to a substrate with refractive index n_S. For the top mirror, the end layer is usually air, making $n_\mathrm{S} = 1$. For the bottom mirror, if refractive index of the substrate is larger than that of the last quarter-wave layer, an extra low refractive index layer should be added in between. The index sequences for the top mirror can be written as $n_\mathrm{C} \mid (n_\mathrm{L} \mid n_\mathrm{H})_{M_\mathrm{t}} \mid n_\mathrm{S}$ with M_t is the number of layer pairs [39]. For the bottom mirror with layer pairs of M_b, the index sequences are $n_\mathrm{C} \mid (n_\mathrm{L} \mid n_\mathrm{H})_{M_\mathrm{b}} \mid n_\mathrm{L} \mid n_\mathrm{S}$ [39]. The intensity reflection coefficient for the top or bottom mirror $R_\mathrm{t,b}$ at the Bragg wavelength λ_0 can be written as [41]

$$R_\mathrm{t,b} = \left(\frac{1 - b_\mathrm{t,b}}{1 + b_\mathrm{t,b}}\right)^2, \tag{2.20}$$

with

$$b_\mathrm{t,b} = \prod_{i=0}^{2M_\mathrm{t,b}} \left(\frac{n_\mathrm{L}}{n_\mathrm{H}}\right), \tag{2.21}$$

referring to the geometrical products of the low-to-high index ratios of every interface in the DBR. Note that, $2M_\mathrm{t,b}$ denotes the total number of quarter-wave layers. The orientation of the layer pairs for both of the mirrors then leads to

$$b_\mathrm{t} = \frac{n_\mathrm{S}}{n_\mathrm{C}} \left(\frac{n_\mathrm{L}}{n_\mathrm{H}}\right)^{2M_\mathrm{t}} \qquad \text{and} \qquad b_\mathrm{b} = \frac{n_\mathrm{L}^2}{n_\mathrm{C} n_\mathrm{S}} \left(\frac{n_\mathrm{L}}{n_\mathrm{H}}\right)^{2M_\mathrm{b}}. \tag{2.22}$$

Equation (2.20) can be used to calculate the peak reflectivities for both of the mirrors.

The DBR is a passive linear network due to the fixed-phase relationship among all the constituting quarter-wave layers. As seen from the cavity, the reflected waves from different interfaces of the DBR superimpose to one another constituting the total reflectivity. The frequency and time response of the DBR (as seen from the high index material inside the resonator) is described by its complex amplitude reflection coefficient [39]

$$r\left(\omega\right)=\sqrt{R\left(\omega\right)}\exp\Big[i\varphi\left(\omega\right)\Big], \tag{2.23}$$

where $R\left(\omega\right)$ and $\varphi\left(\omega\right)$ are real functions of the angular frequency ω. With help of the inverse Fourier transform, it can be shown that for a real impulse, the magnitude and phase of the function $r\left(\omega\right)$ are real and odd functions of the frequency, respectively. Like any linear system, the DBR has a delayed response time τ_{DBR} and the fixed-phase associated with it is $\varphi_0=\omega_0\tau_{\mathrm{DBR}}$. Equation (2.23) then can be written as [42]

$$r=\sqrt{R\left(\omega_0\right)}\exp\Big[-i\left(\omega-\omega_0\right)\tau_{\mathrm{DBR}}\Big]. \tag{2.24}$$

By placing an equivalent fixed-phase mirror at a distance L_{DBR} deep inside the DBR, the reflection delay can be taken into account. Since the wave traverses the distance to the equivalent mirror and back, it can be shown that, $\varphi_0=-2\beta L_{\mathrm{DBR}}$. As the reflection phase varies almost linearly around the center wavelength (odd function of frequency), a Taylor series approximation around its phase φ_0 gives [43]

$$L_{\mathrm{DBR}}=-\frac{1}{2}\frac{\partial\varphi}{\partial\beta}\approx\frac{\lambda_{\mathrm{B}}}{4\Delta n}, \tag{2.25}$$

where the approximation is made for the highly reflective mirror, such as, the DBR of the VCSELs with $\Delta n=n_{\mathrm{H}}-n_{\mathrm{L}}$. Based on this discussion, the effective cavity length L_{eff} is given by

$$L_{\mathrm{eff}}=L+L_{\mathrm{DBR,t}}+L_{\mathrm{DBR,b}}, \tag{2.26}$$

with $L_{\mathrm{DBR,t}}$ and $L_{\mathrm{DBR,b}}$ representing the penetration depth for the top and bottom DBRs, respectively.

2.2.3 Threshold and Operational Characteristics

Since Eq. (2.9) represents the threshold gain for a simple Fabry-Pérot resonator, this has to be extended for the VCSELs considering the appropriate confinement factors and L_{eff}. Before that, we distinguish the intrinsic lossess α_{ia} in the active medium (i.e., MQW layers) and α_{ip} in the passive medium. Equation (2.5) is then extended for a VCSEL as,

$$\alpha=\Gamma\Gamma_{\mathrm{r}}\Big(\alpha_{\mathrm{ia}}-g_{\mathrm{th}}\Big)+\Big(1-\Gamma\Big)\alpha_{\mathrm{ip}}. \tag{2.27}$$

Inserting Eq. (2.27) in Eq. (2.6), we obtain the threshold condition for VCSELs by

$$\begin{aligned} \Gamma\Gamma_{\mathrm{r}}g_{\mathrm{th}} &= \Gamma\Gamma_{\mathrm{r}}\alpha_{\mathrm{ia}} + \frac{1}{L_{\mathrm{eff}}}\left[\alpha_{\mathrm{ip}}\left(L_{\mathrm{eff}} - d_{\mathrm{a}}\right)\right] + \frac{1}{L_{\mathrm{eff}}}\ln\frac{1}{\sqrt{R_1R_2}}, \\ &\approx \alpha_{\mathrm{ip}} + \frac{1}{L_{\mathrm{eff}}}\ln\frac{1}{\sqrt{R_1R_2}} = \alpha_{\mathrm{ip}} + \alpha_{\mathrm{m}}, \end{aligned} \tag{2.28}$$

with the mirror loss abbreviated as $\alpha_{\mathrm{m}} = \frac{1}{L_{\mathrm{eff}}}\ln\left(1/\sqrt{R_1R_2}\right)$ [43]. The approximation in Eq. (2.28) is valid with $L_{\mathrm{eff}} \gg d_{\mathrm{a}}$ and $\alpha_{\mathrm{ia}} \ll g_{\mathrm{th}}$. Knowing the threshold gain, its relation to the photon lifetime τ_{ph} is given by

$$\frac{1}{\tau_{\mathrm{ph}}} = v_{\mathrm{gr}}\Gamma\Gamma_{\mathrm{r}}g_{\mathrm{th}} \approx v_{\mathrm{gr}}\left[\alpha_{\mathrm{ip}} + \frac{1}{L_{\mathrm{eff}}}\ln\frac{1}{\sqrt{R_1R_2}}\right] = v_{\mathrm{gr}}\left(\alpha_{\mathrm{ip}} + \alpha_{\mathrm{m}}\right). \tag{2.29}$$

Note that, for the stimulated emission (above threshold), the gain seen by the cavity mode cannot be described by Eq. (2.28). This is because, under steady-state operation, the gain above the threshold must be equal to that under the threshold operation. This can be expressed as

$$g\left(I_{\mathrm{b}} > I_{\mathrm{th}}\right) = g_{\mathrm{th}}, \tag{2.30}$$

where I_{b} and I_{th} are the bias and threshold currents of the VCSELs. If Eq. (2.30) were not satisfied, the field amplitude in the laser would increase infinitely. Certainly this cannot happen and therefore, the equation

$$N\left(I > I_{\mathrm{th}}\right) = N_{\mathrm{th}}. \tag{2.31}$$

must alo be fulfilled where N represents the electron density.

Next, the basic operational characteristics of the VCSELs will be discussed by means of few important steady-state equations. The emitted optical power P_{opt} with electrically injected bias current I_{b} above the threshold current is given by

$$P_{\mathrm{opt}} = \eta_{\mathrm{i}}\left(\frac{\alpha_{\mathrm{m}}}{\alpha_{\mathrm{ip}} + \alpha_{\mathrm{m}}}\right)\frac{h\nu}{e}\left(I_{\mathrm{b}} - I_{\mathrm{th}}\right); \qquad I_{\mathrm{b}} > I_{\mathrm{th}}, \tag{2.32}$$

with the internal quantum efficiency η_{i} expressing the fraction of the injected carriers reaching the active region for radiative recombination, elementary charge e, lasing frequency ν and Planck's constant h. By defining

$$\eta_{\mathrm{d}} = \eta_{\mathrm{i}}\left(\frac{\alpha_{\mathrm{m}}}{\alpha_{\mathrm{ip}} + \alpha_{\mathrm{m}}}\right), \tag{2.33}$$

Eq. (2.32) is simplified to

$$P_{\mathrm{opt}} = \eta_{\mathrm{d}} \frac{h\nu}{e} \left(I_{\mathrm{b}} - I_{\mathrm{th}} \right); \qquad I_{\mathrm{b}} > I_{\mathrm{th}}, \tag{2.34}$$

with the differential quantum efficiency (DQE) η_{d}. The DQE above the laser threshold represents the fraction of the injected electrons producing external coherent emission through the top or bottom DBRs. For the case that the bottom DBR is totally reflecting, the available power is obtained through the top DBR. Equation. (2.34) shows that the emitted power is a linear function of the bias current above threshold and is generally termed as the light-current (L-I) curve of the lasers. The linearity holds with the assumption that the internal efficiency, confinement factor, cavity losses and gain-current relationship remain constant [43]. In General, the DQE is

$$\eta_{\mathrm{d}} = \frac{e}{h\nu} \frac{dP_{\mathrm{opt}}}{dI_{\mathrm{b}}}; \qquad I_{\mathrm{b}} > I_{\mathrm{th}}, \tag{2.35}$$

where the differential is termed as the slope efficiency (SE) being a direct measure of the DQE since the term $h\nu/e$ is constant. However, accurate estimation of η_{d} requires the capture of the full output power, hence, a large-area PD is often used.

The operating voltage V_{LD} of VCSELs across the terminals is given by

$$V_{\mathrm{LD}} = I_{\mathrm{b}} R_{\mathrm{s}} + V_{\mathrm{d}} + V_{\mathrm{s}}, \tag{2.36}$$

with the differential series resistance, $R_{\mathrm{s}} = dV_{\mathrm{LD}}/dI_{\mathrm{b}}$, ideal diode voltage, V_{d} which is equal to the quasi-Fermi level separation, and current-independent series voltage, V_{s}. The input electrical power, P_{in} of VCSELs is the product of the bias current and V_{LD}, this equals to

$$P_{\mathrm{in}} = V_{\mathrm{LD}} I_{\mathrm{b}} = I_{\mathrm{b}}^2 R_{\mathrm{s}} + I_{\mathrm{b}} V_{\mathrm{d}} + I_{\mathrm{b}} V_{\mathrm{s}}, \tag{2.37}$$

from which the dissipated electrical power, P_{dis} is calculated by

$$P_{\mathrm{dis}} = P_{\mathrm{in}} - P_{\mathrm{opt}} = P_{\mathrm{in}} \left(1 - \eta_{\mathrm{c}} \right), \tag{2.38}$$

with wall-plug or conversion efficiency (CE) as

$$\eta_{\mathrm{c}} = P_{\mathrm{opt}} / I_{\mathrm{b}} V_{\mathrm{LD}}. \tag{2.39}$$

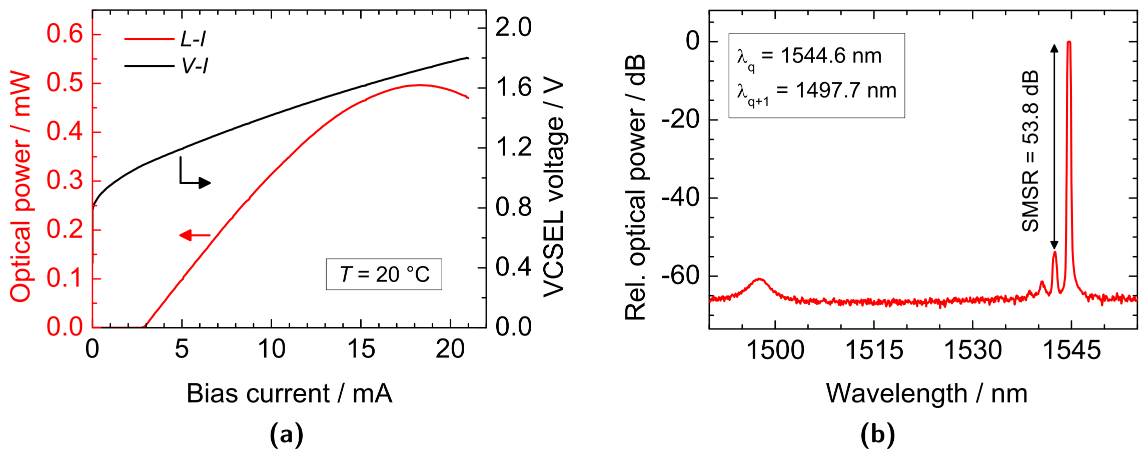

Figure 2.3: (a) *L-I-V* characteristics of a fixed cavity length packaged VCSEL with plane-plane DBR mirrors. (b) Single emission spectra show highly single-mode characteristics.

2.2.4 Output Characteristics of VCSELs

Emission Characteristics

At this point, we show few important characteristics at an example of a fixed cavity length packaged VCSEL with plane-plane DBR mirrors[1]. Its CW light-current-voltage (*L-I-V*) characteristics are shown in Fig. 2.3a. Threshold current and threshold voltage are 2.8 mA and 1.08 V, respectively under stabilized temperature of $T = 20\,^\circ\mathrm{C}$. The linearity of the *P–I* curve above the threshold current is hindered by the thermal rollover of the device [44]. Figure 2.3b shows the emission spectra with $I_\mathrm{b} = 14\,\mathrm{mA}$. Due to the short optical cavity of the VCSELs, the resulting FSR of 46.9 nm inherently supports only one longitudinal mode to lase within the gain spectrum of the active region. SMSR of $\approx 60\,\mathrm{dB}$ to the next higher-order longitudinal mode at 1497.5 nm justifies the previous statement. SMSR is in excess of 53 dB to the next higher-order transverse mode depicts the high spectral purity of this long-wavelength VCSEL.

---

[1] VERTILAS GmbH

Emission Linewidth

Under steady state operation of the lasers, there are still fluctuations of the photon densities due to the presence of the spontaneous emission. This leads to an instantaneous variations of the output power $\delta P\left(t\right)$. This is usually known as relative intensity noise (RIN) and given by

$$\mathrm{RIN} = \frac{\delta P_{\mathrm{opt}}\left(t\right)^2}{P_{\mathrm{opt}}^2}. \tag{2.40}$$

Besides, lasers suffer from the phase fluctuations which are caused by the spontaneous emission as well as carrier density fluctuations. These affect the output wavelength of the lasers and a finite spectral bandwidth, known as linewidth, is observed. THz photomixing based on optical heterodyning of two lasers requires narrow linewidth from each participating laser which is discussed in the following section.

A grating-based optical spectrum analyzer (OSA) does not have the required resolution to measure the linewidth of lasers. Instead, there are methods to characterize the linewidth, such as, optical heterodyne, delayed self-homodyne and delayed self-heterodyne (DSH) methods [45]. To demonstrate the DSH technique which is used in this work, the emitted electric field $E\left(t\right)$ of a laser is mixed with its own time-delayed electric field $E\left(t-\tau_{\mathrm{d}}\right)$. The subsequent autocorrelation function is given by [43]

$$\langle E\left(t\right)E\left(t-\tau_{\mathrm{d}}\right)^*\rangle \propto \exp\Big(i\omega\tau_{\mathrm{d}}\Big)\exp\Big(-\left|\tau_{\mathrm{d}}\right|/\tau_{\mathrm{coh}}\Big), \tag{2.41}$$

with the laser coherence length of τ_{coh}. The first term in Eq. (2.41) is the interference fringes due to the coherence mixing while the latter diminishes the fringes for $\tau_{\mathrm{d}} \gg \tau_{\mathrm{coh}}$, i.e., for sufficiently long delay, the two electric fields become uncorrelated. The DSH technique exactly works on this principle where it takes the fiber-coupled laser beam. The input beam is internally splitted by a directional coupler where one of the two output ports is connected to an acousto-optic modulator (AOM) which shifts the laser frequency by an amount of ν_{AOM}. The other port is connected to a long fiber (decorrelation fiber) providing the required delay discussed above. At the end, another directional coupler combines these two uncorrelated laser beams and its output is fed to a PD where multiplication of the two electric fields are accomplished. This is equivalent to a convolution in the frequency domain. The photocurrent spectrum contains the direct detection and heterodyned signal. A radio-frequency (RF) electrical spectrum analyzer (ESA) displays the desired signal

Table 2.1: Intrinsic linewidth calculation using the DSH technique.

Measured Full-Width Point	DSH Spectral Width
$-3\,\mathrm{dB}$	$2\Delta\nu_{\mathrm{L}}$
$-10\,\mathrm{dB}$	$2\sqrt{9}\Delta\nu_{\mathrm{L}}$
$-20\,\mathrm{dB}$	$2\sqrt{99}\Delta\nu_{\mathrm{L}}$

centered around ν_{AOM} with finite spectral width arising from the intrinsic and extrinsic noise characteristics from both of the interfering signals. The linewidth is defined from the full-width at half-maximum (FWHM) of the DSH signal, $\Delta\nu_{\mathrm{DSH}}$, however, $\Delta\nu_{\mathrm{DSH}}$ is twice as wide as the original laser linewidth [46]. Therefore, $\Delta\nu_{\mathrm{DSH}}$ must be divided by a factor of two assuming the ideal spectral profile is of Lorentzian-shaped

$$|E(\nu)|^2 \sim \frac{1}{1+\left[\dfrac{\nu-\nu_{\mathrm{AOM}}}{\Delta\nu_{\mathrm{L}}/2}\right]^2}, \tag{2.42}$$

where $\Delta\nu_{\mathrm{L}} \approx \Delta\nu_{\mathrm{DSH}}/2$ is the intrinsic linewidth of the laser. $\Delta\nu_{\mathrm{L}}$ is expressed by the modified Schawlow-Townes formula as [47]

$$\Delta\nu_{\mathrm{L}} = \frac{\pi h\nu n_{\mathrm{sp}}}{P_{\mathrm{opt}}\left(2\pi\tau_{\mathrm{ph}}\right)}\left(1+\alpha_{\mathrm{H}}^2\right), \tag{2.43}$$

with n_{sp} as the spontaneous emission factor and α_{H} as the linewidth enhancement factor. Equation (2.43) predicts that the linewidth is inversely proportional to P_{opt}, and ideally, the linewidth as a function of P_{opt} should pass through the origin. In reality, this never approaches to zero, rather has a residual linewidth when extrapolated for $P_{\mathrm{opt}} = \infty$ [48].

In order to show the effect of $1/f$ frequency noise [49] due to frequency jitter of the lasers, or noise arising from the measurement setup and environment, a term $\delta\nu(t)$ can be included in the denominator of Eq. (2.42) as $\nu - \nu_{\mathrm{AOM}} + \delta\nu(t)$ [45]. When $\nu - \nu_{\mathrm{AOM}}$ is comparable to $\delta\nu(t)$, the DSH spectra around its center is significantly influenced. For large values of $\nu - \nu_{\mathrm{AOM}}$, effect of $\delta\nu(t)$ is less pronounced. In this context, the intrinsic linewidth of the lasers can be approximated from the measured full-widths corresponding to frequencies further away from ν_0, as summarized in Tab. 2.1. The correspondence of the intrinsic linewidth to the full-width at different points of the DSH signal is further clarified with a DSH spectrum of the packaged

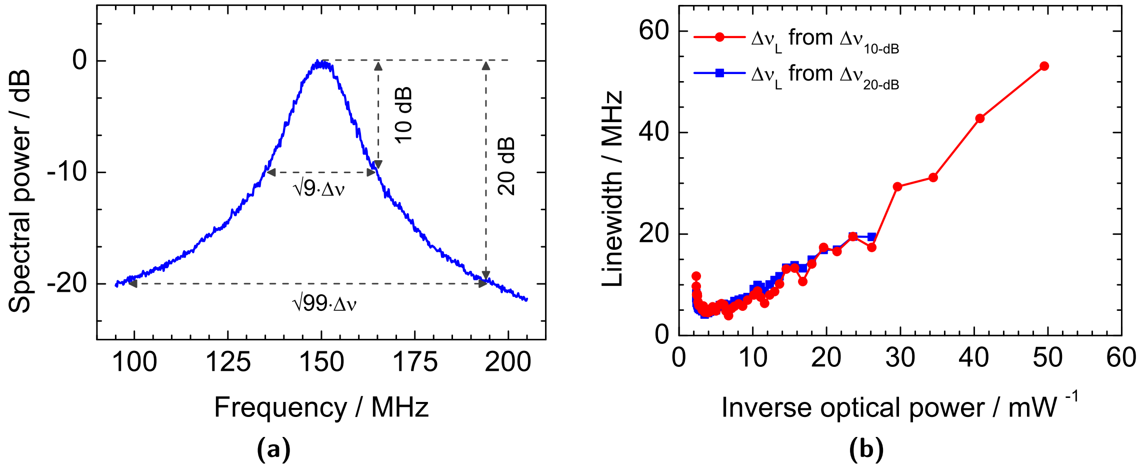

Figure 2.4: (a) DSH spectra of the fixed cavity length VCSEL with $I_b = 5\,\mathrm{mA}$ and (b) calculated linewidth as a function of inverse output power.

VCSEL as shown Fig. 2.4a with $I_b = 5\,\mathrm{mA}$. In order to investigate the linewidth variation of the packaged VCSEL as a function of the bias current (with increasing P_{opt}), a DSH setup[2] is used with $\nu_{\mathrm{AOM}} = 150\,\mathrm{MHz}$ and a decorrelation fiber length of 5 km. The acquired data are of Lorentzian shaped indicating that the influence of the extrinsic noise is not significant. Therefore, the linewidth ($\approx \Delta\nu_L$) is extracted using the relations shown in Tab. 2.1. Values for $\Delta\nu_L$ acquired from the $-10\,\mathrm{dB}$ and $-20\,\mathrm{dB}$ widths are plotted as a function of the inverse optical power as depicted in Fig. 2.4b. These two sets of data correlate very well. However, extracting the intrinsic linewidth of the unpackaged MEMS-VCSELs is not so straightforward using the relation shown in Tab. 2.1. Various noise sources affecting the linewidth of the MEMS-VCSELs are discussed in Sec. 3.3. Based on the discussion covered here, the subsequent interpretation of the linewidth of the MEMS-VCSEL will be highlighted in Sec. 3.5.

Temperature Behavior

As discussed in the preceding section, the emission wavelength of the VCSELs is governed by the cavity resonance, and not by the peak wavelength, λ_g of the material gain as observed in the conventional EELs. An increase of the operating temperature of the semiconductor lasers shifts the spectral emission to longer

---

[2] ADVANTEST, Q73321/M

wavelengths. This effect is usually termed as redshift while the opposite effect with decreasing temperature is known as blueshift. With a constant bias current, the differential of the emission wavelength with respect to the temperature (see Eq. (2.8)) is

$$\frac{d\lambda_{\mathrm{q}}}{dT} = \frac{d}{dT}\left(\frac{2}{q}nL\right) \approx \frac{2L}{q}\frac{dn}{dT} = \frac{\lambda_{\mathrm{q}}}{n}\frac{dn}{dT}. \tag{2.44}$$

Since $dn/dT > 0$, Eq. (2.44) estimates the thermal redshift of laser diodes. As a consequence, the thermal wavelength shift of VCSELs is mainly dominated by the average refractive index change of the DBRs and inner cavity. This wavelength shift depends also on the thermal expansion of the semiconductor layers, however, is insignificant compared to the first one. As illustrated in Fig. 2.5a, the thermal wavelength-shift, e.g., thermal tuning $\Delta\lambda_{\mathrm{T}}$ of the fixed cavity length VCSEL ($I_{\mathrm{b}} = 14\,\mathrm{mA}$) is measured over a temperature range from 20 °C–40 °C. The linear fit to these data extracts $\Delta\lambda_{\mathrm{T}}/\Delta T = 0.106 \pm 0.003\,\mathrm{nm/K}$. In Fig. 2.5b, the wavelength-shift as a function of the bias current is shown. The blue-shift up to the threshold current is due to the well-known Burstein-Moss band-filling effect, however, the redshift above that point is a quadratic function of the bias current indicating the internal heating of the VCSEL. For the I_{b} ranging from 2.9 mA–20 mA, a tuning of 5.69 nm is observed indicating the internal heating of 53.6 °C of the device in excess of the stabilized temperature. A useful measure of the internal heating for any laser diode is given by the thermal resistance

$$R_{\mathrm{th}} = \frac{\Delta T}{P_{\mathrm{dis}}} = \frac{C_1}{C_2}, \tag{2.45}$$

where $C_1 = \Delta\lambda_{\mathrm{T}}/\Delta P_{\mathrm{dis}}|_T$ and $C_2 = \Delta\lambda_{\mathrm{T}}/\Delta T|_{P_{\mathrm{dis}}} = 0.106 \pm 0.003\,\mathrm{nm/K}$. The redshift in Fig. 2.5b has a two-segment linear dependence when plotted against the dissipated power using Eq. (2.38). $C_1 \approx 0.180\,\mathrm{nm/mW}$ is estimated by the corresponding linear fit. From the values of C_1 and C_2, $R_{\mathrm{th}} \approx 1.7\,\mathrm{K/mW}$ is calculated for the exemplary VCSEL. During the operation at elevated temperature, bandgap, E_{g} shrinkage according to $\partial E_{\mathrm{g}}/\partial T < 0$ redshifts the overall gain profile of the MQW layers denoted by $\partial\lambda_{\mathrm{g}}/\partial T$. Usually $\Delta\lambda_{\mathrm{g}} > \Delta\lambda_{\mathrm{T}}$, therefore, relative wavelength-shift between the cavity mode and gain spectrum for the VCSELs is observed under varying temperature of operation.

The typical temperature range of operation for this VCSEL is from 0 °C–70 °C, therefore, the achievable tuning range for this VCSEL is limited to $\Delta\lambda_{\mathrm{T}} = 7.42\,\mathrm{nm}$ at best. The tuning range of the fixed cavity length packaged VCSEL is indeed fairly limited. Therefore, it will be phrased as non-tunable VCSEL throughout this work. Besides, the tuning speed is of practical importance and is required to be

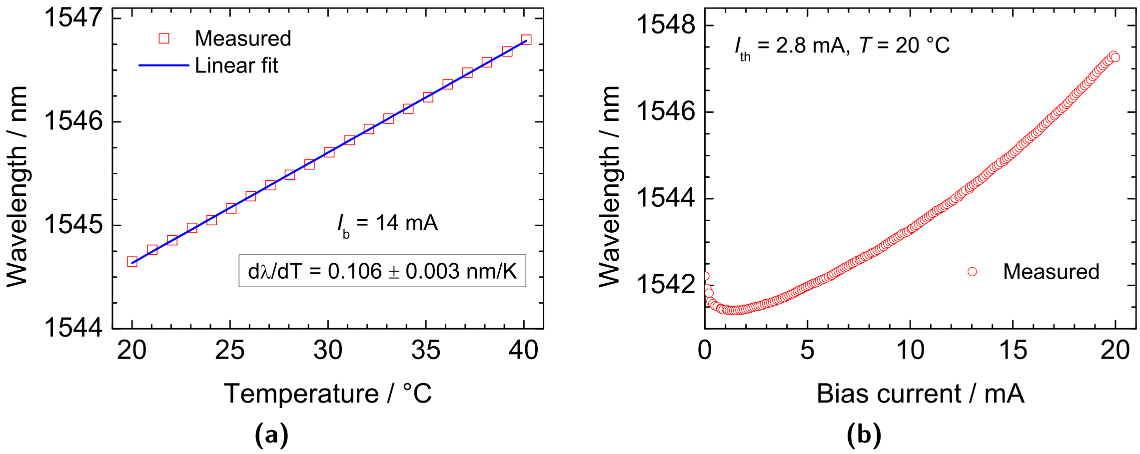

Figure 2.5: (a) Redshift (thermal tuning) of the fixed cavity length VCSEL as a function of the operating temperature. (b) Redshift of the same VCSEL as a function of the bias current indicating internal heating of the device.

much faster than the thermal tuning speed for most communication applications. A MEMS tunable VCSEL meets these requirements where the electrothermal actuation of its MEMS component tunes the wavelength over a broader spectral range with faster tuning speed.

2.3 Transverse Mode Resonators

In the following, we will discuss a plane-concave, circularly symmetric stable resonator relevant to the structure of a 1550 nm tunable VCSEL used in this work. The stability of a resonator is read by its g-parameters [50]. The g-parameters of the plane and concave mirrors with radius of curvatures (*RoC*) ρ_1 and ρ_2, respectively are [50]

$$g_{1/2} = 1 - \frac{L_{\text{opt}}}{\rho_{1/2}}, \tag{2.46}$$

where L_{opt} is the optical length of the resonator. The stability of this resonator is given by

$$0 < g_1 g_2 < 1. \tag{2.47}$$

With the boundary conditions imposed by this pair of mirrors, there are certain field distributions on the mirrors representing the steady-state solutions, i.e., eigensolutions. The round trips of these eigensolutions are described mathematically by

Kirchhoff integral whose solutions represent the eigenmodes of the resonator [50]. The complete set of solutions can be expressed as Laguerre-Gaussian modes [51] with a circularly symmetric Gaussian beam as the fundamental eigenmode. Since transverse higher-order modes also satisfy the boundary conditions for the resonator, the eigenmodes are characterized by the transverse mode numbers with indexes p, l and the axial/longitudinal mode order q, where p, l, q are integers. These modes are characterized by transverse electro-magnetic (TEM) modes of TEM_{plq}, where both the electric and magnetic field vectors are perpendicular to each other and the wavevector [50]. Since q is a large number, the notation TEM_{pl} is used to indicate the radial and azimuthal nodes of the intensity distributions for a circularly symmetric resonator. The field distribution for the fundamental TEM_{00} mode, therefore, is given by the complex envelope of the Gaussian beam as a function of the axial and radial position z and $\rho = \sqrt{x^2 + y^2}$, respectively [51],

$$E\left(\rho{,}z\right) = \frac{E_1}{q\left(z\right)} \exp\left[\frac{-ik}{2}\frac{\left(x^2+y^2\right)}{q\left(z\right)}\right] \exp\left(-ikz\right), \tag{2.48}$$

with E_1 as a constant and the q-parameter of the beam $q\left(z\right)$ as,

$$q\left(z\right) = z + iz_0, \tag{2.49}$$

where z_0 is known as the Rayleigh length. The q-parameter can alternatively be written in terms of its real and imaginary part by [51]

$$\frac{1}{q\left(z\right)} = \frac{1}{R\left(z\right)} - i\frac{\lambda}{\pi w^2\left(z\right)}, \tag{2.50}$$

with beam width radius $w\left(z\right)$ and *RoC* of the wavefront $R\left(z\right)$. Inserting Eq. (2.50) in Eq. (2.48) yields [50, 51],

$$E\left(\rho{,}z\right) = E_0\frac{w_0}{w\left(z\right)} \exp\left[\frac{-ik}{2}\frac{\left(x^2+y^2\right)}{R\left(z\right)}\right] \exp\left[-\frac{\left(x^2+y^2\right)}{w^2\left(z\right)}\right] \exp\left(-ikz\right), \tag{2.51}$$

with a new constant $E_0 = E_1/iz_0$ and w_0 as the beam waist radius. While propagating, $w\left(z\right)$ diverges in both directions from w_0 and its energy is confined about its propagation/longitudinal axis (z axis). The beam width $w\left(z\right)$ is given by

$$w\left(z\right) = w_0\sqrt{1+\left(\frac{z}{z_0}\right)^2}, \tag{2.52}$$

where $z_0 = \pi w_0^2/\lambda$. The wavefront normals of the propagating wave are paraxial rays and characterized by the *RoC* as

$$R(z) = z\left[1 + \left(\frac{z_0}{z}\right)^2\right]. \tag{2.53}$$

Equation (2.53) implies that the Gaussian beam is a plane wave at $z = 0$ and transforms into a spherical wave for $z = \infty$. To put in a simple way, the field distribution in plane 1 (at $z = 0$) is a real Gaussian distribution with

$$E_1(\rho,0) = E_0 \exp\left[-\frac{(x^2+y^2)}{w_0^2}\right] \exp(-ikz), \tag{2.54}$$

where the beam waist radius is $w_0 = w(0)$. The field distribution at a distance z from the first plane then can be expressed by Eq. (2.51).

For this fundamental mode, its beam radius with propagation can be calculated by using ABCD law [50]. Equation (2.52) gives the beam radius at any point inside the resonator. Besides, the beam radii on both mirrors can be expressed through the respective g-parameters, optical spacing and wavelength of operation as

$$w_{00,u}^2 = \frac{\lambda L_{\text{opt}}}{\pi}\sqrt{\frac{g_v}{g_u(1-g_u g_v)}}; \quad u,v = 1,2; \quad u \neq v. \tag{2.55}$$

If a plane mirror (mirror 1, $u = 1$) is placed at $z = 0$, the beam waist radius of the TEM$_{00}$ mode is $w_0 = w_{00,1} = w(z=0)$. Similarly, the beam width radius (greater than the beam waist radius at mirror 1) at a concave mirror (mirror 2, $u = 2$), spaced at optical distance L_{opt} can also be deduced using Eq. (2.55). We have intentionally used the example of a plane-concave resonator for being the basis of a MEMS-VCSEL. For higher-order transverse-modes, the beam radii on these mirrors can be calculated by [50]

$$w_{pl,u} = w_{00,u}\sqrt{2p+l+1}; \qquad u = 1,2. \tag{2.56}$$

In order to calculate the beam radius at location z between the two mirrors, Eq. (2.56) can be extended by [50]

$$w_{pl,u}(z) = w_{00,u}\sqrt{2p+l+1}\sqrt{1+\left(\frac{z}{z_0}\right)^2}, \qquad u = 1,2, \tag{2.57}$$

with beam waist radius (at mirror 1) defined by Eq. (2.55) at the plane mirror. Figure 2.6 schematically shows a plane-concave resonator with electric field distributions of the fundamental and higher-order transverse modes. The beam waist

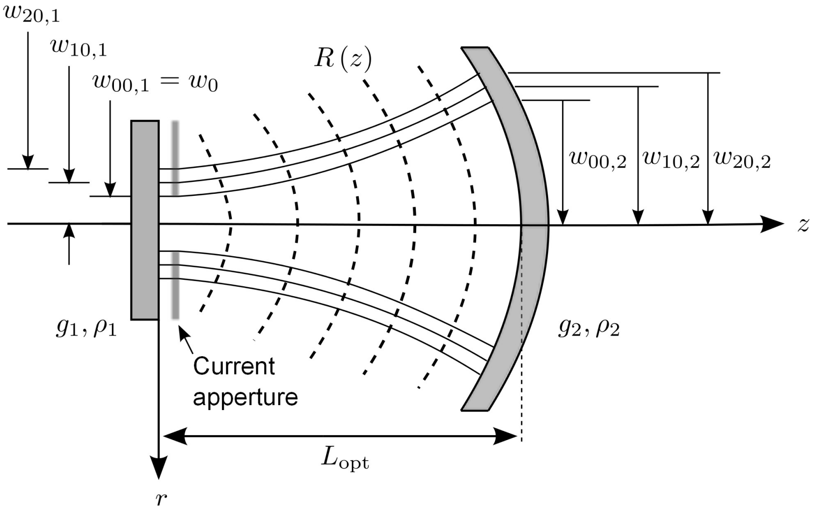

Figure 2.6: Schematic of a plane-concave resonator with Gaussian beam propagation. The beam waist $w_{00,1}$ of the fundamental mode is at the plane mirror while $w_{00,2}$ represents the beam width radius at the concave mirror at a distance of L_{opt}. The same set of parameters are also shown for two higher-order transverse-modes.

radius of the fundamental mode is located at the plane mirror indicated by $w_{00,1}$, while the beam width radius, after propagating the resonator length, is $w_{00,2}$ at the concave mirror. The same set of parameters are also shown for two higher-order transverse-modes.

We have, so far, considered the resonator without any limiting aperture. In a practical resonator, the bias current pumps the active gain medium through a defined aperture.

3 MEMS-Tunable VCSELs at 1550 nm

The short cavity length of VCSELs leads to an inherently large longitudinal mode spacing. Few nanometers thermal tuning of a fixed cavity length VCSEL is presented in Sec. 2.2.4. To realize continuous mode-hop-free tuning over a wide wavelength span, a special measure needs to be incorporated into the optical cavity design. In this context, we use an optical cavity design for VCSELs where a fixed-plane bottom DBR mirror and a MEMS-based concave DBR mirror sandwich the fixed cavity along with a variable-length air gap. The combination of the MEMS-based concave DBR and air gap act as a tunable mirror structure when electrical actuation of the MEMS thermally modulates the length of the air gap. Thus, the resonant wavelength of the cavity is tuned. The bottom DBR along with the fixed semiconductor cavity is known as half-VCSEL[1]. Surface micromachining technique realizes the fabrication of tunable mirror structure on top of the half-VCSEL to accomplish a full laser structure operating around the center wavelength of 1550 nm.

In this chapter, the basic structure of MEMS-tunable VCSELs (MEMS-VCSELs) is presented. Detailed characterization of the on-wafer, electrically-injected MEMS-VCSELs are presented including electrothermal tuning characteristics, wavelength fluctuations analysis, wavelength stabilization technique, emission linewidth analysis, and spectral purity.

3.1 Device Structure

3.1.1 Half-VCSEL Structure

The term half-VCSEL stems from the fact that one of the mirrors to accomplish a full laser structure is absent. A cross-sectional schematic of the half-VCSEL structure

---

[1] VERTILAS GmbH

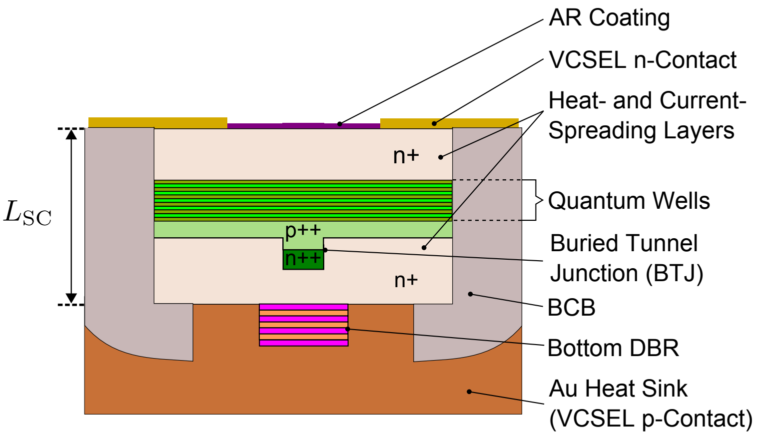

Figure 3.1: Cross-sectional schematic of a half-VCSEL structure.

is shown in Fig. 3.1. It is commonly composed of a semiconductor cavity (SC) containing few AlInGaAs-based MQW layers, a buried tunnel junction (BTJ) [6], two InP heat- and current-spreading layers and the integrated bottom DBR mirror. The optical length of the SC will be termed as L_{SC}. Quarter-wavelength ($\lambda_0/4$) thick anti-reflection (AR) coating is used between the SC-air interface, where λ_0 is the center wavelength (Bragg wavelength) of the reflectivity bandwidth. The half-VCSEL is mounted on an electroplated gold substrate. To enhance high-speed operation, it is essential to reduce the parasitic resistance and capacitance of the device. The semiconductor (InP) around the mesa is replaced by a low-dielectric-constant passivation layer of Benzocyclobutene (BCB) eliminating the parasitic capacitances. Besides, the half-VCSEL shows comparably low ohmic resistance, since high-conducting n-material replaces most of the low-conducting semiconductor p-material due to the BTJ structure. The MQW layers of the active gain medium are grown with a compressive strain to achieve low transparency carrier densities and higher differential gain [52]. The optical cavity length of the half-VCSEL is $3\lambda_0$.

The lateral current confinement is accomplished by incorporating a circular BTJ in the center part of the device serving as current aperture. The tunnel junction layers consist of few nanometer thick, highly doped p^{++}-InGaAlAs/n^{++}-InGaAs. Using a BTJ is advantageous in a number of ways. Since the free carrier absorption, α_{fc} rises with the square of wavelength, the p-conducting semiconductor material appears lossy at this wavelength of operation. This is shown as [53]

$$\alpha_{\text{fc}} = \frac{\lambda^2}{n} \frac{e^3}{4\pi^2 \varepsilon_0 c^3} \left[\frac{N_{\text{dop}}}{m_{\text{e}}^2 \mu_{\text{e}}} + \frac{P_{\text{dop}}}{m_{\text{h}}^2 \mu_{\text{h}}} \right] \tag{3.1}$$

where masses and mobilities of electron and hole are m_{e}, m_{h} and μ_{e}, μ_{h}, doping concentrations in the n- and p-type materials are N_{dop}, P_{dop}, and e, ε_0 and c are the natural constants. The BTJ, therefore, facilitates the replacement of the lossy p-conducting material around its mesa with the regrowth of n-conducting material [53]. This is schematically shown in Fig. 3.1. As a consequence, a reverse-biased $p^{++}n$-junction is formed in the outer part of the mesa confining the pump current effectively through the BTJ diameter, d_{BTJ}. With pumping, the electrons in the valence band of the p-doped material tunnel to the conduction band of n-doped material, thus the generated holes are carried to the active zone, and recombination takes place. Though heavily doped materials inherently feature high optical losses, the thin BTJ, as well as its placement at one of the nodes of the optical standing wave, reduces the free-carrier absorption significantly. However, as the resonator length changes with electrothermal tuning (see Sec. 3.1.3), the node of the standing wave pattern moves away from the BTJ. This degrades the confinement factor and contributes to increased threshold gain. The advantage of deploying the BTJ reflects the output characteristics of MEMS-VCSELs with small differential series resistance and threshold voltage [9].

A VCSEL can be approximated as a cylindrical step-index optical fiber with the core refractive index, n_{core} of lateral dimension equal to d_{BTJ}, and with cladding refractive index, n_{clad} of the outer part of BTJ mesa [54]. The mode cutoff frequency is determined by the normalized frequency parameter, V as

$$V = \frac{\pi d_{\text{BTJ}}}{\lambda} \sqrt{n_{\text{core}}^2 - n_{\text{clad}}^2}, \tag{3.2}$$

with single-mode emission condition of $V < 2.405$ (assuming no optical losses). The beam waist w_0 of the fundamental Gaussian mode is related to V and d_{BTJ} by [54]

$$w_0 = \frac{d_{\text{BTJ}}}{2\sqrt{\ln(V)}}. \tag{3.3}$$

For $V < 2.405$, the relation of $d_{\text{BTJ}} > 2w_0$ is obtained from Eq. (3.3). For presented half-VCSELs, $d_{\text{BTJ}} = 14\,\mu\text{m}$ is designed. The relatively large value of d_{BTJ} is primarily intended to extract higher single-mode output power. However, this generally should come at the expense of higher-order transverse modes due to the index

Table 3.1: Half-VCSEL parameters.

Parameter	Symbol	Value
Bottom DBR Reflectivity	$R_{\mathrm{DBR,b}}$	$\approx 100\,\%$
BTJ Diameter	d_{BTJ}	$14\,\mu\mathrm{m}$
Linear Expansion Coefficients	$\alpha_{\mathrm{th,BCB}}$	$42 \cdot 10^{-6}/\mathrm{K}$
	$\alpha_{\mathrm{th,InP}}$	$4.6 \cdot 10^{-6}/\mathrm{K}$
	$\alpha_{\mathrm{th,Au}}$	$14.2 \cdot 10^{-6}/\mathrm{K}$

guiding caused by the BTJ [55, 56]. There are methods to reduce the index guiding, for example, planarization of the overgrown BTJ [57]. In this way, gain guiding of the fundamental mode is increased with respect to that of the lateral higher-order transverse modes. In other words, the loss of the higher-order modes will be too high to compete with the fundamental mode, and single-mode emission is ensured despite having a large diameter BTJ.

The bottom DBR mirror consists of alternating fluoride- and sulphide-based dielectric layers with each layer thickness of $\lambda_0/4$. For high-speed BCB MEMS-VCSELs, the bottom mirror consists of ZnS/CaF_2-based dielectric materials with alternating index difference of 0.85 [56]. To achieve a broader reflectivity bandwidth around the center wavelength, the integrated bottom DBR mirror terminates to a gold substrate. The combination of dielectric DBR layers with metal is also called hybrid DBR. From the discussion in Sec. 2.2.2, the first layer seen from the optically dense InP material is CaF_2 layer with lower refractive index. Then the alternating sequence of DBR requires an even number of layer pairs terminated to the gold. There is an additional phase shift of π at the interface of the last ZnS and gold layers [58]. To avoid this unwanted phase shift, an additional CaF_2 layer is used. With this combination, the intensity reflection coefficient/reflectivity of the bottom plane mirror, $R_{\mathrm{DBR,b}}$, becomes nearly 100 % over the entire tuning range. Table 3.1 summarizes some useful parameters of half-VCSELs will be needed to discuss the experimental characterization in Sec. 3.2.

3.1.2 MEMS-Tunable DBR Mirror Structure

Based on the surface micromachining technique, we fabricate the top DBR mirror supported through four suspension beams over the exit aperture of the half-VCSEL.

Table 3.2: Growth direction of dielectric DBR layers of a MEMS-tunable DBR mirror, the center wavelength of the reflection bandwidth is 1550 nm.

Air

Number of Pairs	Material	Geometrical Thickness / nm	Refractive Index	Stress / MPa
6	$\mathrm{Si_aN_b}$	203.2	1.907	-81
	$\mathrm{Si_cO_d}$	271.2	1.429	-105
5	$\mathrm{Si_aN_b}$	205.9	1.882	+132
	$\mathrm{Si_cO_d}$	271.2	1.429	-105
0.5	$\mathrm{Si_aN_b}$	205.9	1.882	+132

Ni Sacrificial Layer

Half-VCSEL

An electrically injected current actuates the MEMS component on top of this mirror, the subsequently generated heat causes thermal expansion of the DBR mirror altering the air gap. In other words, tuning is accomplished for a MEMS-VCSEL by changing its resonator length through the actuation of its MEMS component. In the following, the fabrication of the MEMS-tunable DBR mirror structure is presented.

$\mathrm{Si_aN_b}/\mathrm{Si_cO_d}$-based dielectric layers are deposited using low-temperature ($< 100\,^{\circ}\mathrm{C}$), plasma-enhanced chemical vapor deposition (PECVD) on a Ni sacrificial layer. The deposition starts with a $\lambda_0/2$-thick $\mathrm{Si_aN_b}$ layer, followed by 22 $\lambda_0/4$-thick, alternating layers of $\mathrm{Si_cO_d}$ and $\mathrm{Si_aN_b}$, respectively. Note that we use optical thicknesses for simplicity. Intentional stress gradients (tensile/compressive) are incorporated during the growth of these layers. The first 5.5 pairs in the growth direction have tensile stress while the remaining have compressive stress. Table 3.2 highlights the order of deposition with respective parameters. The alternating refractive index contrast among the first 5.5 pairs is $\Delta\bar{n}_{\mathrm{DBR,t}} = 0.45$, whereas the next six pairs have a contrast of 0.47. Taking this into account, the peak reflectivity can be calculated by Eqs. (2.22) (with $n_{\mathrm{S}} = 1, n_{\mathrm{C}} = 1$) and (2.20). A transfer matrix-based 1-D simulation is used to plot the reflectivity, $R_{\mathrm{DBR,t}}$ of the top DBR as a function of wavelength as displayed in Fig. 3.2. The peak reflectivity obtained at 1550 nm is 99.77 %. The reflectivity is larger than 99.5 % for a wavelength range of 1478 nm–1629 nm as shown by the inset of Fig. 3.2. It is worth mentioning that the simulation might differ than

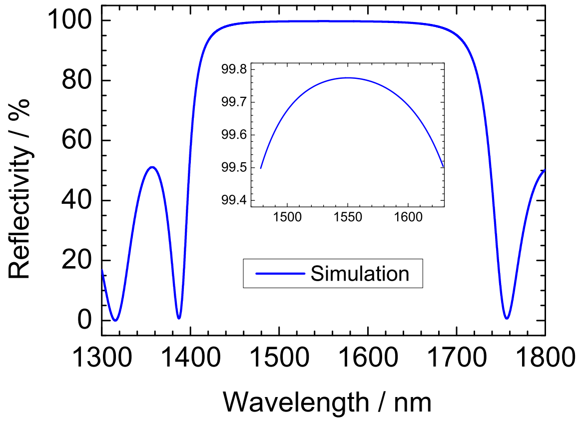

Figure 3.2: Simulation of the intensity reflection coefficient, $R_{\mathrm{DBR,t}}\left(\lambda\right)$ of the top DBR mirror. Inset is the zoom in view of $R_{\mathrm{DBR,t}}\left(\lambda\right)$ over a smaller wavelength range showing more than 99.5 % reflectivity over the whole lasing range.

the practical reflection measurement. This is due to the inaccuracy in thickness of any layer occurred during the deposition by the PECVD. An approximate thickness error of 3 % is reported in Ref. [59].

After the deposition of the dielectric DBR layers, several processing steps are required to pattern a fully functional device. The steps are briefly tabulated in Tab. 3.3 [58]. After deposition of DBR layers, thin layers of Cr and Au are thermally evaporated. The subsequent processings (photolithographic structuring and wet chemical etching) open a circular-shaped hole in the metal electrode with a diameter of 50 µm serving as an exit aperture for the light. Next, a 600 nm thick Ni layer is sputtered onto this structure. The following photolithographic step defines the characteristic geometry of the top DBR (a circular dish connected to four beams) with Ni layer on top as an etch-mask layer. The following dry etching for the unwanted DBR layers is performed with the Ni sacrificial layer acting as etch-stop layer. The structured diameter of the circular dish is 110 µm (with encompassed exit aperture for light), the length and width of each beam are 150 µm and 60 µm, respectively. As one of the final steps, both Ni layers are simultaneously wet-etched. At this point, intentional stress gradients incorporated during the growth of the dielectric layers deflect the DBR mirror vertically. The four flexible beams support the suspension of the mirror, and an overall concave bending is achieved with a pre-calculated *RoC*. At equilibrium, the amount of the deflection is denoted by L_{air}. As the very final step, the device is dried in a critical point dryer to eliminate any capillary force causing the bottom part of the mirror sticking to the half-VCSEL surface. Throughout this thesis, the suspended MEMS-tunable DBR mirror structure will be termed

Table 3.3: Processing steps for tunable MEMS-VCSELs [58].

Half-VCSEL structure	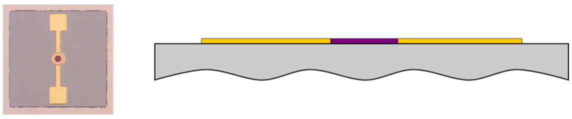
400 nm thick Ni sacrificial layer sputtering (lithography) and structuring (wet etching)	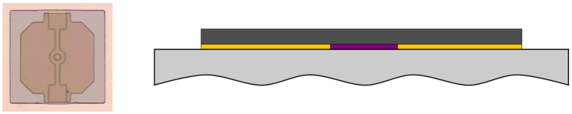
Si_aN_b/Si_cO_d layer pairs deposition by low temperature PECVD	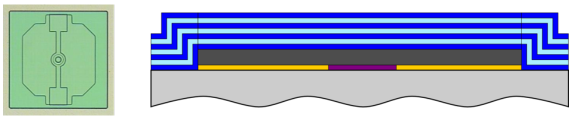
Cr/Au layers evaporation and structuring	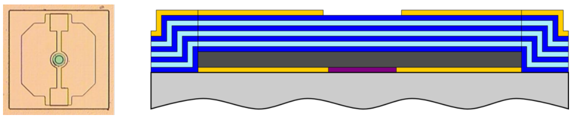
600 nm thick Ni layer sputtering, patterned with photolithography as an etch-mask for mirror (as well as Cr/Au layers) and suspension beams structuring	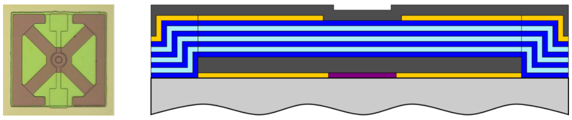
Dry etching of DBR, Ni layers removing (etch-mask and sacrificial layers), mirror released due to intrinsic stress gradients and suspended by beams, critical point drying	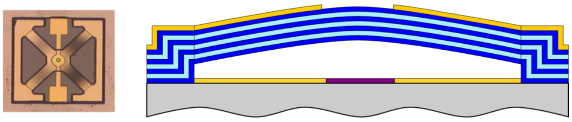

Table 3.4: MEMS-tunable DBR mirror (membrane) parameters.

Parameter	Symbol	Value
Membrane DBR Reflectivity	$R_{\mathrm{DBR,t}}$	$> 99.5\,\%$
Material Density	ρ_{m}	$2.3\,\mathrm{g/cm^3}$
Membrane Thickness	h_{m}	$5.3\,\mu\mathrm{m}$
Suspension Beam Length	l_{m}	$150\,\mu\mathrm{m}$
Suspension Beam Width	w_{m}	$60\,\mu\mathrm{m}$
Membrane Diameter	d_{m}	$110\,\mu\mathrm{m}$
Membrane Mass	m_{m}	$0.55\,\mu\mathrm{g}$
Linear Expansion Coefficients	$\alpha_{\mathrm{th,SiN}}$ $\alpha_{\mathrm{th,SiO}}$	$2.3 \cdot 10^{-6}/\mathrm{K}$ $0.5 \cdot 10^{-6}/\mathrm{K}$

as membrane DBR, or simply as a membrane. Table 3.4 highlights some useful parameters of the membrane which will be needed to discuss the experimental characterization in Sec. 3.2.

3.1.3 Electrothermal Tuning Mechanism

A fully fabricated MEMS-VCSEL, as schematically shown in Fig. 3.3, has a plane-concave Fabry-Pérot resonator with the optical cavity length of

$$L_{\mathrm{opt}} = L_{\mathrm{DBR,b}} + L_{\mathrm{SC}} + L_{\mathrm{air}} + L_{\mathrm{DBR,t}}. \tag{3.4}$$

A laser diode controller (LDC)[2] injects a bias current, I_{b} for electrical pumping of the active medium of MEMS-VCSELs. Another LDC provides the heating/tuning current, I_{MEMS} through the electrodes of the membrane (membrane actuation current). The subsequent Joule heating, P_{heat} causes the thermal expansion of the membrane which in turn alters the air gap by an amount of ΔL_{air}. A change in the air gap tunes the emission wavelength and thus, electrothermal tuning, $\Delta\lambda_{\mathrm{ET}}$, is shown as

$$\Delta\lambda_{\mathrm{ET}} \propto \Delta L_{\mathrm{air}} \propto P_{\mathrm{heat}} = I_{\mathrm{MEMS}}^2 \cdot R_{\mathrm{MEMS}}, \tag{3.5}$$

---

[2] ILX Lightwave, 3722B

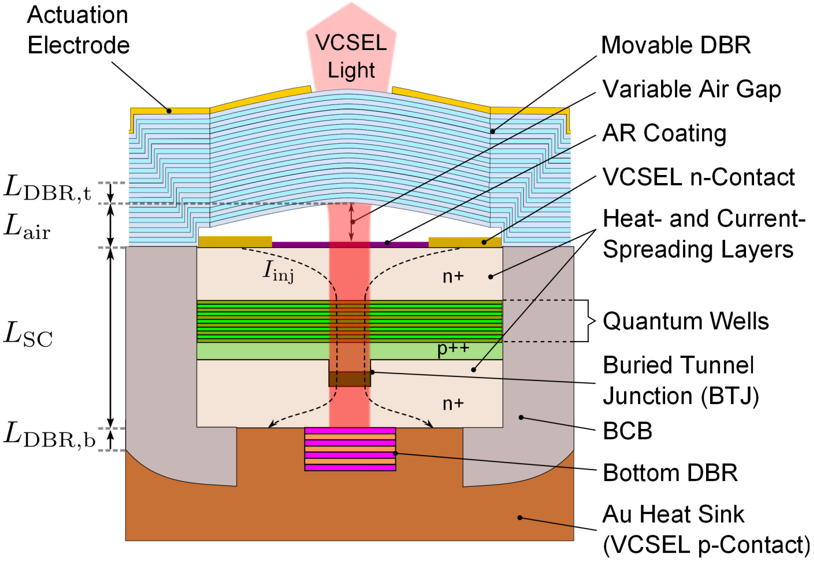

Figure 3.3: Cross-sectional schematic of a MEMS-VCSEL structure.

where $R_{\mathrm{MEMS}} \approx 20\,\Omega$ is the electrical resistance of the electrodes evaporated on top of the membrane. From Eq. (3.5), the wavelength tuning is quadratically and linearly related to I_{MEMS} and P_{heat}, respectively. The phase fronts of the fundamental Gaussian mode follow the mirror geometries during CW tuning. To validate this, we first show the relation of the beam waist at the bottom plane DBR mirror as a function of the RoC of the membrane by putting $u = 1, v = 2$ and, $g_1 = 1$ in Eq. (2.55) as [60]

$$w_0 = \sqrt{\frac{\lambda_0}{\pi}\sqrt{L_{\mathrm{opt}}\left(RoC - L_{\mathrm{opt}}\right)}}. \tag{3.6}$$

To estimate the RoC of the membrane, a confocal microscope investigates the geometry of a MEMS-VCSEL at ambient temperature and pressure. Figure 3.4a shows the three-dimensional image of the MEMS-VCSEL. Figure 3.4b shows the diagonal scan along two suspension beams from which L_{air} of $\approx 6.1\,\mu\mathrm{m}$ is measured. The following fit with a circular function extracts the RoC of $1615.80 \pm 0.01\,\mu\mathrm{m}$. Using $\lambda_0 = 1550\,\mathrm{nm}$, $L_{\mathrm{opt}} = L_{\mathrm{SC}} + 6.1\,\mu\mathrm{m}$, $L_{\mathrm{DBR,b}} = 0.45\,\mu\mathrm{m}$, $L_{\mathrm{DBR,t}} = 0.77\,\mu\mathrm{m}$, and $RoC \approx 1615.80\,\mu\mathrm{m}$, Eq. (3.6) predicts a beam waist of $w_0 \approx 8.27\,\mu\mathrm{m}$ at the plane mirror. Thus, $2w_0$ of the TEM$_{00}$ mode is larger than the designed d_{BTJ}. Under this situation, the angle of divergence will increase at the aperture edges, an increased fraction of power will hit the aperture after each round trip constituting the diffraction losses [50]. This loss, however, will be pronounced even more for the higher-order transverse modes. By controlling the deposition parameters such as pressure, temperature, inductively-coupled plasma (ICP) power, RF power and

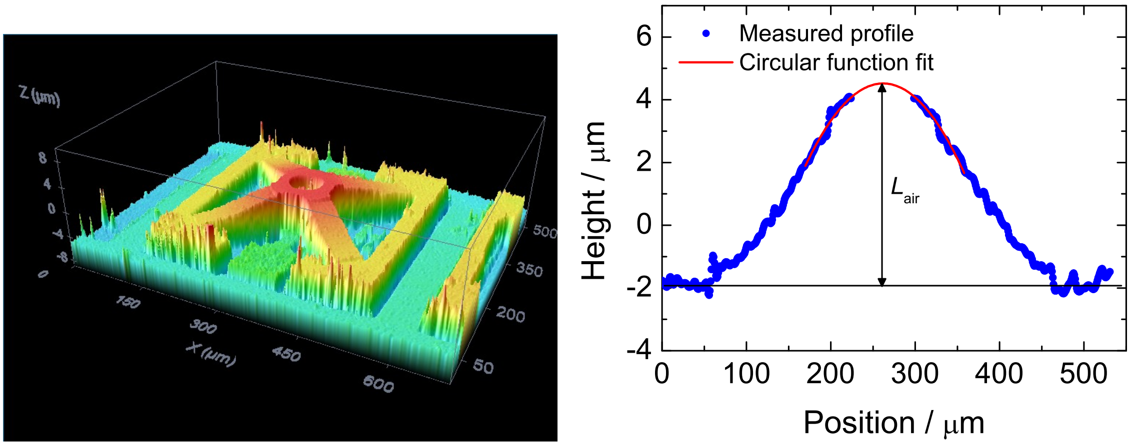

(a) **(b)**

Figure 3.4: (a) Confocal microscope image shows the membrane profile of a MEMS-VCSEL. (b) The diagonal scan along two suspension beams shows $L_{\text{air}} \approx 6.1\,\mu\text{m}$, the following fit with a circular function extracts the $RoC = 1615.80 \pm 0.01\,\mu\text{m}$.

flow rate of the gasses in the PECVD chamber, the stress in the dielectric layers can be changed in order to achieve the desired RoC to fulfill Eq. (3.6).

The fabricated MEMS-VCSEL is of external-cavity (EC) configuration due to the use of AR coating at the SC-air interface [61, 62]. The shift of the resonance wavelength with a given change in air gap thickness is given by [63]

$$\frac{\Delta\lambda}{\lambda_0} = \frac{\gamma_{\text{c}} \Delta L_{\text{air}}}{L_{\text{DBR,b}} + L_{\text{SC}} + \gamma_{\text{c}} \left(L_{\text{air}} + L_{\text{DBR,t}}\right)}, \tag{3.7}$$

with phase coupling factor $\gamma_{\text{c}} = d\varphi_{\text{eff}}/d\varphi_{\text{air}}$ where φ_{eff} and φ_{air} are the reflected phase from the membrane and round-trip phase in the air gap, respectively. For an ideal AR coating, we obtain of $\gamma_{\text{c}} = 1$. In the EC structure, therefore, no phase shift occurs at the SC-air interface, and an uninterrupted cavity sustains between the two DBR mirrors. Consequently, the actuation mechanism invokes the linear tuning scaled with the air gap thickness. Mode-hop-free CW tuning of the single-mode emission is thus accomplished by electrothermal actuation of the membrane. Note that, due to the AR coating, the EC structure becomes sensitive to any imperfections of the membrane [61].

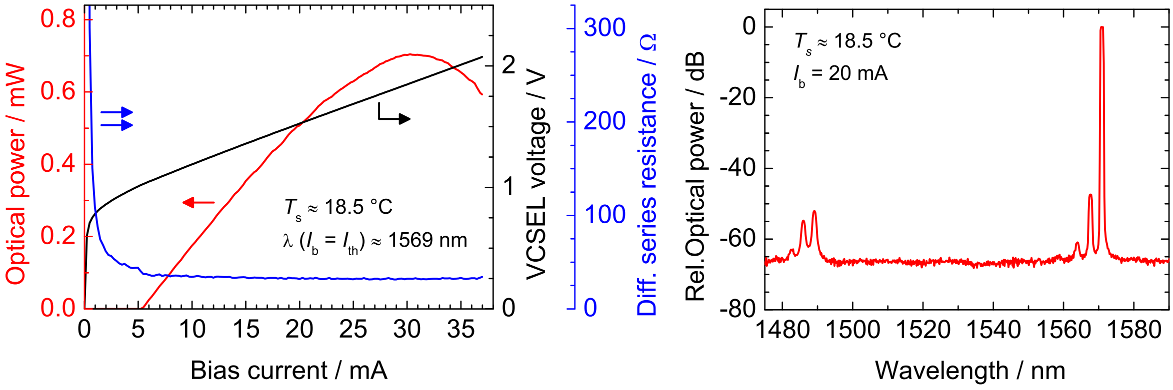

(a) **(b)**

Figure 3.5: (a) *L*-*I*-*V* characteristics of the MEMS-VCSEL with $I_{\text{MEMS}} = 0\,\text{mA}$, the outer y-axis corresponds to the differential series resistance. (b) Single emission spectra with $I_\text{b} = 20\,\text{mA}$ and $I_{\text{MEMS}} = 0\,\text{mA}$.

3.2 Experimental Characterization

3.2.1 Electrothermal Tuning Characteristics

Figure 3.5a shows the *L*-*I*-*V* characteristics of a MEMS-VCSEL under stabilized substrate temperature of $T_\text{s} \approx 18.5\,°\text{C}$. The CW power of the MEMS-VCSEL is coupled to a standard single-mode fiber (SMF) via an AR coated lens, followed by an in-line isolator to reduce back-reflections. Threshold current and voltage are 5.22 mA and 1.01 V, respectively. The incorporation of the BTJ replacing much of the lossy p-materials and better heat sinking lead to differential series resistance of less than 41 Ω under lasing operation. The driving voltage remains below 1.9 V up to the maximum coupled power of 0.7 mW before thermal rollover. The output power is as high as 1 mW when coupled with a multi-mode fiber (MMF). MEMS-VCSELs are longitudinally single-mode lasers. Figure 3.5b shows the emission characteristic with $I_\text{b} = 20\,\text{mA}$ and $I_{\text{MEMS}} = 0\,\text{mA}$ where the MEMS-VCSEL emits in the fundamental mode confirmed by a far-field measurement [17]. The spectral distance to the next higher-order longitudinal mode (FSR) is about 82 nm with SMSR in excess of 52 dB. The SMSRs are in excess of 47 dB with respect to the higher-order transverse modes, thus, the MEMS-VCSEL is in single-mode operation. The greatly suppressed transverse modes also bear the information that the phase fronts of the fundamental mode have an effective match to the resonator structure. However, $2w_0 > d_{\text{BTJ}}$ is predicted by Eq. (3.6) which is, however, perfectly valid

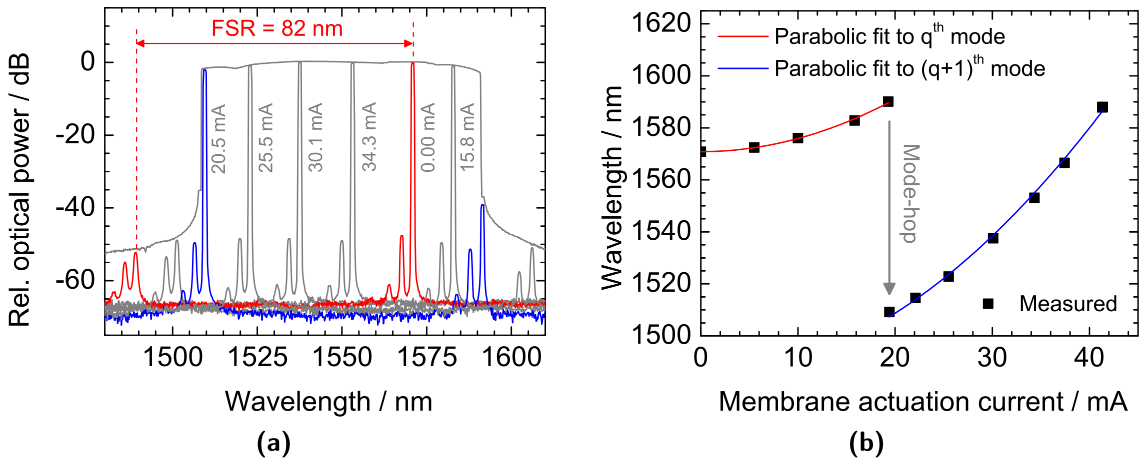

Figure 3.6: (a) Electrothermal tuning of the MEMS-VCSEL with a CW tuning range of 81 nm as indicated by the envelope of the peak fundamental emission. The FSR of this device is 82 nm. (b) Parabolic fit showing that emission wavelength is quadrically related to I_{MEMS}.

for the passive resonators ignoring many active resonator elements [64]. The phase fronts of the fundamental mode will match better to the resonator structure with an appropriately engineered *RoC* of the membrane. By controlling the parameters of the PECVD, this can be ensured and such a MEMS-VCSEL is reported in Ref. [17] with the threshold current, output power and tuning range of 2.6 mA, 3.2 mW and 107 nm, respectively.

Figure 3.6a illustrates the electrothermal tuning of the on-wafer MEMS-VCSEL. The peak emission wavelength of the longitudinal mode-order q is at $\lambda_{\text{q}} \approx 1571$ nm as already shown in Fig. 3.5b with the next higher-order $(q+1)^{\text{th}}$ mode located at about 1489.2 nm. The corresponding FSR amounts to a THz bandwidth of 10.47 THz. With an increase of the membrane current, the emission peak of the q^{th} mode (as well as that of the other mode) continuously moves toward the higher wavelengths accomplishing a mode-hop-free tuning up to 1590 nm. This is depicted by the envelope of the peak fundamental emission captured by the OSA. With further increase of the membrane current, the q^{th} mode competes with its counterpart for the gain. The peak emission wavelength of $\lambda_{\text{q+1}} \approx 1509$ nm for $I_{\text{MEMS}} =$ 20.5 mA (blue trace) depicts the situation where a longitudinal mode-hop occurs. For the membrane current ranging from 20.5 mA–42 mA, mode-hop-free CW tuning of this mode can be accomplished up to $\lambda_{\text{q+1}} \approx 1590$ nm ($\approx$ 81 nm). Note that, several emission spectra with different membrane currents are shown for better understanding of the tuning characteristics of the MEMS-VCSEL. The corresponding peak emission wavelength as a function of the membrane current is shown in Fig. 3.6b. To demonstrate the quadratic behavior of the emission wavelength versus actuation current (see Eq. (3.5)), a parabolic fit with $(a + b \cdot I^2_{\mathrm{MEMS}})$ is used, where a and b correspond to the wavelength at 0 mA (with no heating power) and tuning efficiency of a certain mode, respectively. For q^{th} mode, the fit extracts the tuning efficiency of $0.050 \pm 0.001\,\mathrm{nm/mA^2}$ where this is $0.059 \pm 0.001\,\mathrm{nm/mA^2}$ for the $(q+1)^{\mathrm{th}}$ mode.

For practical applications, longitudinal mode-hop-free tuning is desired. Blueshift of the MEMS-VCSEL with an increase of the substrate temperature can move the q^{th} mode (as in Fig. 3.6a) to the short-wavelength side of its tuning range. This blueshift is in contrast to the typical redshift of semiconductor lasers (see Fig. 2.5a). As explained in Sec. 2.2.4, the redshift of conventional semiconductor lasers is governed by the increase of the refractive index and thermal expansion of the semiconductor materials defining the cavity length. The principle remains the same for MEMS-VCSELs, however, the emission wavelength is mainly governed by the position of membranes. The half-VCSEL materials, such as Au, BCB encapsulation, and InP semiconductor have different thermal expansion coefficients than those of the dielectrics of the membrane [17, 65]. As summarized in Tabs. 3.1 and 3.4, the thermal expansion coefficients of half-VCSEL materials (mainly governed by the BCB) are larger than those of the membrane dielectrics. For an increase of the substrate temperature, consequently, the lateral expansion of the half-VCSEL pulls down the suspended membrane decreasing the air gap. This overcompensates the increase of the optical length of the SC and causes blueshift. This also depends on the mechanical properties of the membrane, in particular, its geometry, stiffness, mass and curvature which strongly rely on the details of the device processing. Figure 3.7 shows the blueshift of the lasing wavelength as a function of the substrate temperature. The corresponding CW power is also shown in the same figure. Several mode-hops are observed while the measured data with almost linear relation represent certain longitudinal modes. For instance, a linear fit to the lasing wavelengths from 27 °C–35 °C shows a blueshift of $d\lambda/dT_{\mathrm{s}} = -9.50 \pm 0.07\,\mathrm{nm/K}$. To enable an uninterrupted CW tuning (avoiding longitudinal mode-hops) for the MEMS-VCSEL as shown in Fig. 3.6a, the substrate temperature can be changed to $\approx 26\,°\mathrm{C}$ so that the lasing takes place at $\lambda_{\mathrm{q}} \approx 1509\,\mathrm{nm}$ with $I_{\mathrm{MEMS}} = 0\,\mathrm{mA}$. The subsequent electrothermal actuation, thus, allows the mode-hop-free tuning of the respective mode up to $\lambda_{\mathrm{q}} \approx 1590\,\mathrm{nm}$. To accompany this broadband tuning, the corresponding mechanical displacement, Δx of the membrane from its equilibrium

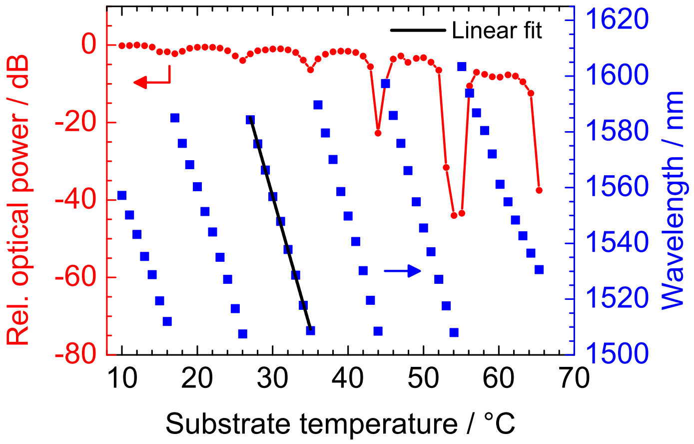

Figure 3.7: Blueshift of the lasing wavelength with varying substrate temperatures. The linear fit shows a blueshift of $d\lambda/dT_\mathrm{s} = -9.50 \pm 0.07\,\mathrm{nm/K}$.

position is given by [66]

$$\Delta x = \frac{\Delta\nu\lambda}{2FSR_\nu}, \tag{3.8}$$

where $\Delta\nu$ and λ are the peak frequency difference and center wavelength of the tuning range, respectively. Since $\Delta\nu \approx FSR_\nu$ for this MEMS-VCSEL, the corresponding mechanical displacement of the membrane amounts to $\approx 775\,\mathrm{nm}$.

Due to the short optical cavity of VCSELs, a single longitudinal cavity mode spectrally overlaps with the gain bandwidth of the active medium [67]. The emission wavelength of VCSELs, therefore, is determined by the cavity resonance and not by the gain peak as in conventional EELs. The output power, as shown in Fig. 3.7, has the highest value (except for higher temperature) in the middle of the respective tuning range. In other words, starting from the short-wavelength side of the tuning range (of certain longitudinal mode), the output power gradually increases due to the better spectral alignment of the cavity resonance and laser gain. The maximum power corresponds to the best alignment followed by its gradual decrease towards the long-wavelength side of the tuning range. Note that, the peak of the gain bandwidth also experiences a redshift with increasing temperature, however, is negligible with the temperature-induced mechanical movement of the membrane.

The variation of the threshold current over the entire tuning range of the MEMS-VCSEL is measured and plotted in Fig. 3.8a. An approximate parabolic shape is traced out by the threshold current and can again be described by the cavity detuning. At both edges of the tuning range, cavity detuning is the highest concerning the wavelength of maximum gain for a fixed temperature of operation. Besides,

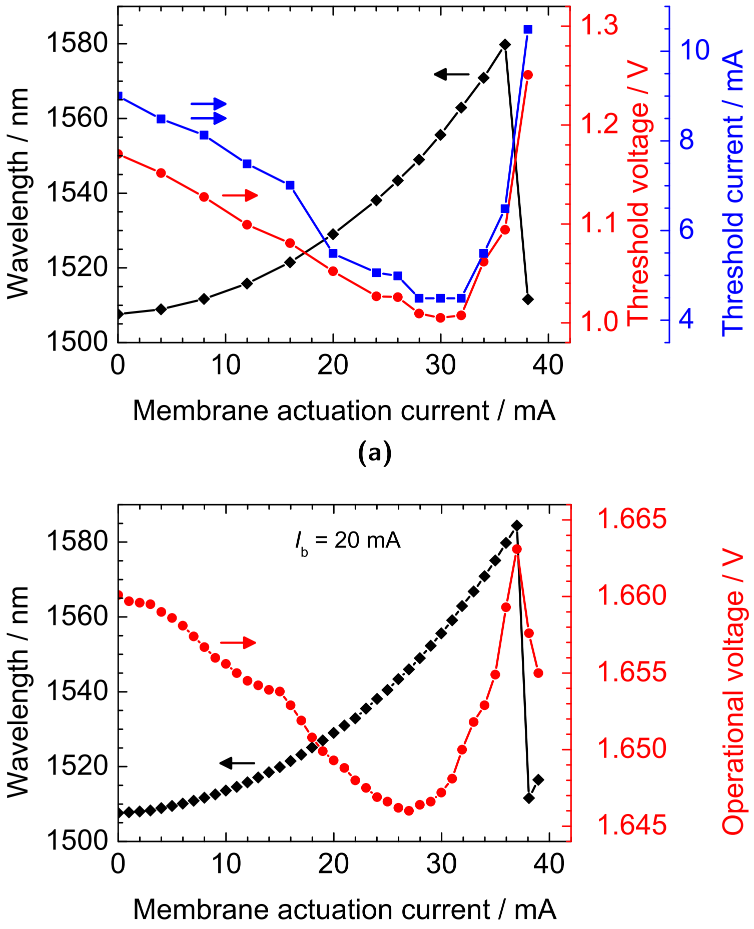

(a)

(b)

Figure 3.8: (a) Threshold current and voltage, and emission wavelength of the MEMS-VCSEL as a function of I_{MEMS}. (b) Emission wavelength and operating voltage above threshold ($I_b = 20\,\mathrm{mA}$) as a function of I_{MEMS}.

the confinement factor reduces as the node of the standing wave pattern moves away from its optimum position (for $\lambda_q = 1550\,\mathrm{nm}$) located at the center of the BTJ. Moreover, the losses of the mirrors away from the center frequency are higher. As a whole, the non-optimized interaction between the electrical and optical fields accounting for the total losses increase the threshold gain, i.e., threshold current. As a function of the membrane current, I_{th} gradually reduces to a minimum indicating zero detuning with the gain peak and increases again for the opposite reasoning. The variation of the threshold voltage, as also illustrated in the same figure, follows the same pattern traced out by the threshold current. In Fig. 3.8b, the voltage, V_{LD}

of the MEMS-VCSEL operated far above the threshold ($I_b = 20\,\text{mA}$) is also plotted over the tuning range. We see that the profiles of the threshold parameters (current and voltage) correlate very well with that of V_{LD}. During the stimulated emission, however, the laser dynamics are not influenced by the threshold parameters. Recalling Eq. (2.36), V_{LD} is a function of the series resistance, R_s and diode voltage, V_d (assuming $V_s = 0$). For a fixed bias current of operation, V_{LD} should be ideally constant. From Fig. 3.8b, V_{LD} is not constant and varies by an amount of few millivolts. The reason for such a small deviation is from the combined variations of the R_s and V_d, though it looks to be governed by the change of V_d, i.e., the separation of the quasi-Fermi level. We believe, thus, the profile of the operating voltage represents the effective gain seen by the cavity resonance.

3.2.2 Temperature Tuning Characteristics

Figure 3.9a shows wavelength tuning of the MEMS-VCSEL for three different substrate temperatures. For $T_s = 25\,^\circ\text{C}$, the membrane current ranging from 0 mA–33 mA enables the CW, mode-hop-free tuning for the q^{th} mode while the further increase of the I_{MEMS} brings the $(q+1)^{\text{th}}$ mode to lase to its short-wavelength side of the respective tuning range. For $I_{\text{MEMS}} = 0\,\text{mA}$, when the substrate temperature is changed from 25 °C to 35 °C, the MEMS-VCSEL experiences a large blueshift of 95 nm (see Fig. 3.7). Thus, the longitudinal mode order is reduced by one from q^{th} mode to $(q-1)^{\text{th}}$ mode for which the peak emission wavelength is 1523 nm with $I_{\text{MEMS}} = 0\,\text{mA}$ as shown by the blue trace in Fig. 3.9a. The shortening of the optical cavity with increasing temperature is accompanied by an increase of the FSR, i,e., an increase of the tuning range. Due to this reason, the subsequent CW tuning of this mode shifts the next longitudinal mode-hop to a longer wavelength with $I_{\text{MEMS}} = 34.8\,\text{mA}$. This can alternatively be understood by comparing the mode-hop current of $(q+1)^{\text{th}}$ and q^{th} modes for 25 °C and 35 °C, respectively. In a similar fashion for $T_s = 45\,^\circ\text{C}$, the membrane current of 37.2 mA induces a mode-hop from $(q-2)^{\text{th}}$ mode to $(q-1)^{\text{th}}$ mode indicating that the FSR keeps increasing with an increase of the substrate temperature. The increase of the FSR is in agreement with the plot in Fig. 3.7 where an intuitive comparison among the lengths of all open-squared diagonal-lines reflects the statement.

Next, we investigate the CW tuning power as a function of the membrane current for different substrate temperatures as shown in Fig. 3.9b. For a given temperature change, the redshift of the peak gain wavelength is larger than that of the cavity resonance, i.e., $d\lambda_g/dT_s > d\lambda/dT_s$. Due to this reason, the initial wavelengths of

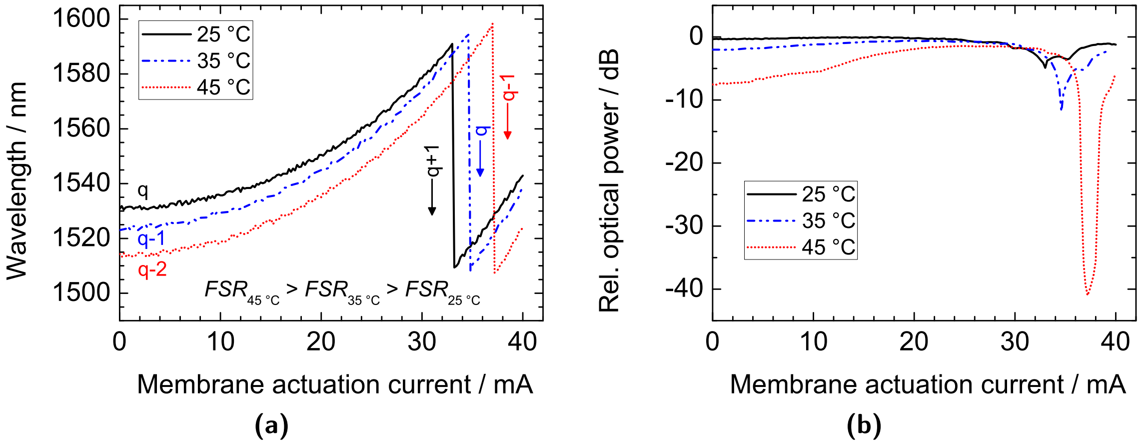

Figure 3.9: (a) Peak emission wavelength and (b) corresponding CW power as functions of the membrane actuation current for different substrate temperatures.

the different modes for $I_{\mathrm{MEMS}} = 0\,\mathrm{mA}$ see reduced gain with increasing temperature. This can be best understood with the power profile for $T_{\mathrm{s}} = 45\,°\mathrm{C}$, where a reduction of power at the beginning of the CW tuning is explicit. A complementary understanding can again be achieved with the experimental result as illustrated in Fig. 3.7. To demonstrate, lasing of the longitudinal mode around 40 °C desists at the beginning of its tuning range. This becomes more pronounced with the next mode around 50 °C. Beyond 60 °C, the power, as well as tuning range, are drastically reduced.

The increase of the FSR does not necessarily mean to increase the CW tuning and power. As a matter of fact, both depend on the initial deflection of the membrane. If the initial deflection fulfills the better matching of the phase fronts to the resonator geometry, increase or decrease of the substrate temperature will not improve the CW power and tuning of the MEMS-VCSEL. In most cases, the membrane deflection is not optimum. Therefore, the optimum operating condition can be tuned with the appropriate substrate temperature.

Characteristic Temperature

It is of practical importance to know the characteristic temperature T_0 of the lasers which is given by

$$T_0 = (T_{\mathrm{i}} - T_{\mathrm{j}}) / \ln \left(I_{\mathrm{th}}(T_{\mathrm{i}}) / I_{\mathrm{th}}(T_{\mathrm{j}}) \right) \tag{3.9}$$

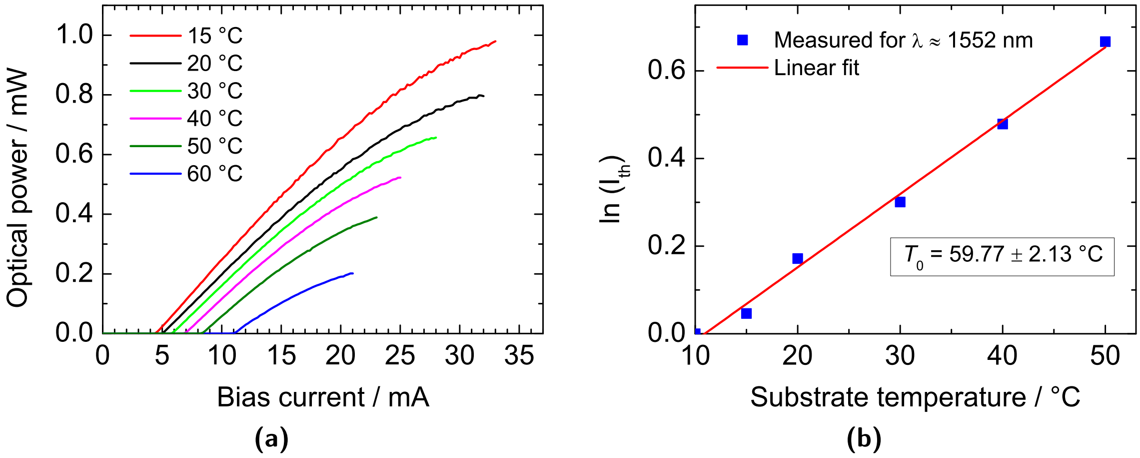

(a) **(b)**

Figure 3.10: (a) *L-I-V* at different substrate temperatures. (b) Characteristic temperature of the MEMS-VCSEL.

with $I_{\text{th}}(T_{\text{i}})$ as the threshold current at temperature T_{i}. T_0 predicts the reliable operation of any laser under elevated temperature. To calculate T_0, we measure the *L-I* characteristics at different substrate temperatures while keeping the emission wavelength at 1552 nm by adjusting the membrane current. *L-I* characteristics at different temperatures are presented in Fig. 3.10a. The obtained threshold currents are normalized with $I_{\text{th}}\left(T_{\text{j}} = 10\,°\text{C}\right)$, and the natural logarithm of those versus the substrate temperature is plotted in Fig. 3.10. The inverse of the slope of the linear fit to this curve yields $T_0 = 59.77 \pm 2.13\,°\text{C}$ for the presented MEMS-VCSEL. This value is in agreement with the deteriorated performance of the MEMS-VCSEL over 55 °C, as observed in Fig. 3.7.

3.2.3 Electrothermal Frequency Response

The electrothermal tuning of MEMS-VCSELs is a linear function of the dissipated heat of the membrane. The linearity in tuning, however, is limited by the thermal inertia of the membrane. Therefore, the frequency response of a MEMS-VCSEL is investigated by monitoring its peak emission in response to a sinusoidal modulation of the membrane actuation current of

$$I_{\text{MEMS}}\left(t\right) = I_{\text{MEMS}} + I_{\text{pp}} \sin\left(2\pi f_{\text{mod}} t\right), \tag{3.10}$$

where I_{pp} is the peak-to-peak amplitude of the modulation current. The MEMS-VCSEL is biased with $I_{\text{b}} = 20\,\text{mA}$ and $I_{\text{MEMS}} = 25\,\text{mA}$ at $T_{\text{s}} = 22\,°\text{C}$. The corre-

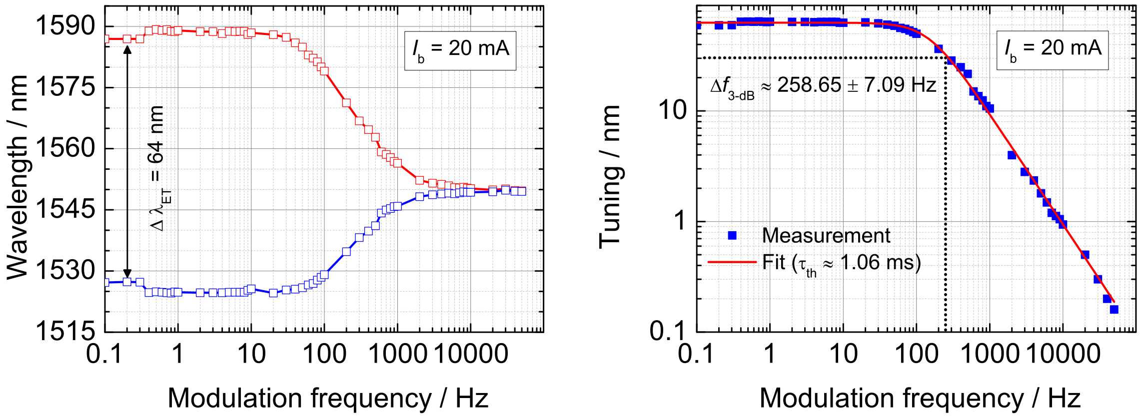

(a) **(b)**

Figure 3.11: Electrothermal frequency response of the MEMS-VCSEL for initial wavelength excursion of $\Delta\lambda_{\mathrm{ET}} = 64\,\mathrm{nm}$. (b) First-order low-pass filter behavior of the modulation performance.

sponding static lasing is at $\approx 1550\,\mathrm{nm}$. With $I_{\mathrm{pp}} = 20\,\mathrm{mA}$, the membrane oscillates between 15 mA and 35 mA and results in a wavelength variation between 1525 nm and 1589 nm at low modulation frequencies as illustrated in Fig 3.11a. With increasing modulation frequency, the initial wavelength variation of $\Delta\lambda_{\mathrm{ET}} = 64\,\mathrm{nm}$ reduces gradually and finally merges to the static lasing wavelength of 1550 nm. This behavior stems from the thermal inertia of the membrane itself. The time cycle for heat generation and dissipation (tuning) inside the membrane are approximately in phase to that of the modulation current at low frequency. At a high frequency of operation, the membrane cannot respond to the fast-changing modulation cycles resulting in the static emission from the DC actuation of the membrane. The thermal inertia of the membrane follows a low-pass filter behavior of the first order of,

$$\Delta\lambda(f) = \frac{\Delta\lambda_{\mathrm{ET}}}{\sqrt{1 + 3\left(f/f_{\mathrm{mod,\,3\text{-}dB}}\right)^2}}, \tag{3.11}$$

with a 3 dB frequency of

$$f_{\mathrm{mod,\,3\text{-}dB}} = \sqrt{3}/(2\pi\tau_{\mathrm{th}}), \tag{3.12}$$

where τ_{th} is the thermal time constant of the membrane. With Eq. (3.11), the corresponding fit to the experimental data extracts of $f_{\mathrm{mod,3\text{-}dB}} = 258.65 \pm 7.09\,\mathrm{Hz}$ featuring $\tau_{\mathrm{th}} = 1.06\,\mathrm{ms}$, as illustrated in Fig. 3.11b. Since the tuning of MEMS-VCSELs results from the power dissipation (i.e., thermal expansion) of the membrane, a factor of $\sqrt{3}$ is employed in Eq. (3.12). In practice, large-signal modulation of the membrane current and the subsequent tuning of MEMS-VCSELs are very attractive for many practical applications. Such as spectroscopy of NH_3 and CO are demonstrated in Ref. [19] with broadband tuning of a MEMS-VCSEL with a scan rate of as high as 5 Hz limited by the deployed data acquisition system.

3.2.4 Polarization Properties

The photomixing process requires two lasers of the same polarization. Usually, photomixing setups are therefore constructed using polarization-maintaining (PM) fibers. The laser sources, therefore, need to be polarization stable. At the one hand, polarization stability for MEMS-VCSELs is achieved by incorporating a certain degree of anisotropic gain/loss in the MQW layers to break the polarization degeneracy [68]. The incorporated anisotropy avoids polarization switching between the low-indexed crystal directions of the active medium. On the other hand, the membrane itself can act as a polarization selective reflector incorporating anisotropic losses. This applies particularly to a membrane with geometrical asymmetries, i.e., different radii of curvature in the respective transverse directions which the membrane may feature due to processing inaccuracies or stress.

To characterize the polarization behavior of MEMS-VCSELs, the emitted beam is measured by a large area photodiode (PD) after it trespasses a rotatable polarizer[3]. The power emitted along the main emission axis of a MEMS-VCSEL phrased as P_{par}, and that emitted in the direction orthogonal to the first one as P_{orth}, are plotted as a function of the bias current as depicted in Fig. 3.12a with $I_{\mathrm{MEMS}} = 23.86\,\mathrm{mA}$ and $T_{\mathrm{s}} = 22\,^{\circ}\mathrm{C}$. The MEMS-VCSEL is polarization stable with parallel-to-orthogonal polarization-suppression-ratio (PSR) of $> 20\,\mathrm{dB}$ ranging from $I_{\mathrm{b}} = 8.75\,\mathrm{mA}$–$26\,\mathrm{mA}$. The maximum PSR of $\approx 23\,\mathrm{dB}$ is obtained with $I_{\mathrm{b}} = 25\,\mathrm{mA}$, yet limited by the polarization extinction ratio of the setup.

Figure 3.12b shows the polarization-resolved CW tuning of the MEMS-VCSEL with $I_{\mathrm{b}} = 20\,\mathrm{mA}$. An excellent stability with PSR of $> 20\,\mathrm{dB}$ is maintained ranging from $I_{\mathrm{MEMS}} = 0\,\mathrm{mA}$–$26.5\,\mathrm{mA}$ (1525 nm–1556 nm) with the maximum of $> 24\,\mathrm{dB}$ with $I_{\mathrm{MEMS}} = 9.6\,\mathrm{mA}$. The PSR decreases towards the higher membrane current with the minimum value of $\approx 12\,\mathrm{dB}$ with $I_{\mathrm{MEMS}} = 37.58\,\mathrm{mA}$.

Fabrication inaccuracy-induced tilt of the suspended membrane could cause the degradation of the polarization, for instance, if the beams holding the membrane

---

[3] Thorlabs, LPNIR050-MP

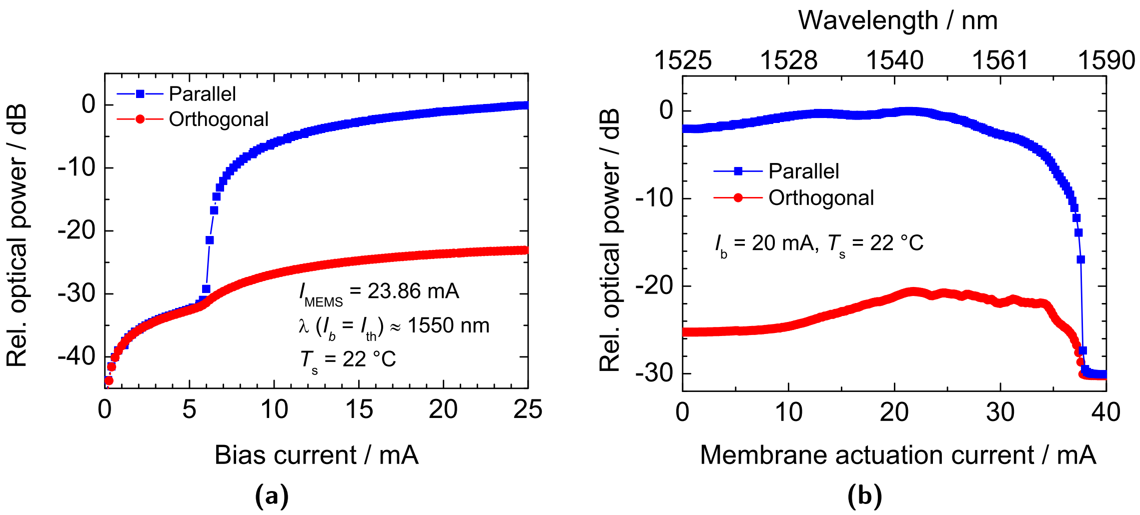

Figure 3.12: (a) Polarization-resolved L-I characteristics of a MEMS-VCSEL with $I_{\mathrm{MEMS}} = 23.86\,\mathrm{mA}$, $\lambda(I_{\mathrm{b}} = I_{\mathrm{th}}) \approx 1550\,\mathrm{nm}$, $T_{\mathrm{s}} = 22\,°\mathrm{C}$. (b) Polarization-resolved CW tuning as a function of the membrane actuation current for $T_{\mathrm{s}} = 22\,°\mathrm{C}$.

are slightly different. Based on the type of initial asymmetries, a significant mechanical movement of the membrane can cause a substantial tilt which in turn can favor the opposite polarization. Both electrothermal heating, as well as substrate temperature, affect the stress and tilt within the membrane. For the presented MEMS-VCSEL, a value of $d\lambda/dT_{\mathrm{s}} \approx -9.5\,\mathrm{nm/K}$ causes a downward mechanical movement of the membrane of $\approx 2.54\,\mu\mathrm{m}$ for a temperature rise from 22 °C–50 °C. Figure 3.13 displays the measured P_{par} and P_{orth} as a function of the membrane current with $I_{\mathrm{b}} = 20\,\mathrm{mA}$. While increasing the membrane current (0 mA–40 mA), the polarization switches with $I_{\mathrm{MEMS}} \approx 36\,\mathrm{mA}$. With the decreasing membrane current (40 mA–0 mA), the polarization switches with $I_{\mathrm{MEMS}} \approx 28.6\,\mathrm{mA}$ giving rise a hysteresis-like behavior. Since the MEMS-VCSEL is operated with a fixed bias current of $I_{\mathrm{b}} = 20\,\mathrm{mA}$, the polarization switch can only be attributed to the mechanically pronounced tilt of the membrane.

3.2.5 Mechanical Properties

The mechanical properties of the membrane determine the wavelength stability of MEMS-VCSELs. The characteristic motion of the membrane can be described as a

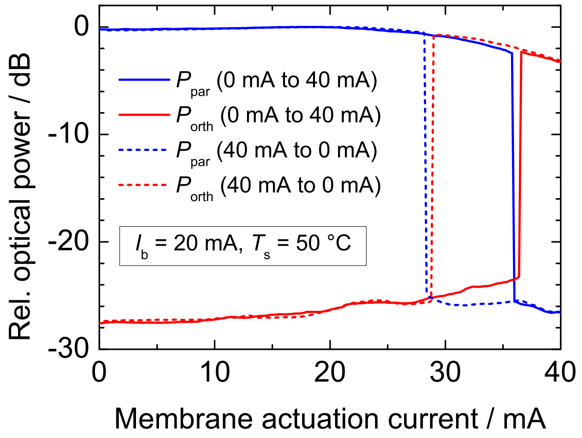

Figure 3.13: Polarization switch of a MEMS-VCSEL as a function of the increasing (0 mA–40 mA) and decreasing (40 mA–0 mA) membrane current with I_b =20 mA and T_s =50 °C.

mechanical resonator by [66, 69]

$$m_m \ddot{x} + R_m \dot{x} + k_m x = F(t), \tag{3.13}$$

where x is the displacement of the membrane from its equilibrium position, m_m, R_m, k_m are the mass, damping constant and spring constant of the membrane, and $F(t)$ is the force acting on the membrane. Since the membrane is suspended in air, we expect little damping and therefore neglect the second term in Eq. (3.13). The fundamental mechanical resonance frequency of the membrane is thus

$$\nu_{res,1} \approx \frac{1}{2\pi}\sqrt{\frac{k_m}{m_m}}. \tag{3.14}$$

The calculated mass of the membrane from its dimensions is $m_m \approx 0.55\,\mu g$. According to Refs. [70, 71], only half of each suspension beam experiences the vibration of the membrane, leading to an effective mass of $m_{m,eff} \approx 0.34\,\mu g$. The spring constant can be determined by a measurement of the mechanical resonance spectra of the membrane. Such a measurement is reported for an electrostatically tunable MEMS-VCSEL using laser Doppler vibrometer (LDV) [70]. Figure 3.14a (left) shows an electrothermally tunable MEMS-VCSEL with a broken membrane DBR and thus the circular n-contact around the exit aperture of the half-VCSEL becomes visible. For electrostatic actuation, a subsequent bias is thus applied between the n-contact and the electrodes of the membrane forming a capacitor as shown in Fig. 3.14b. The sinusoidal modulation of the voltage is given by

$$V(t) = V_{DC} + V_{pp}\sin(2\pi f_{mod} t) \tag{3.15}$$

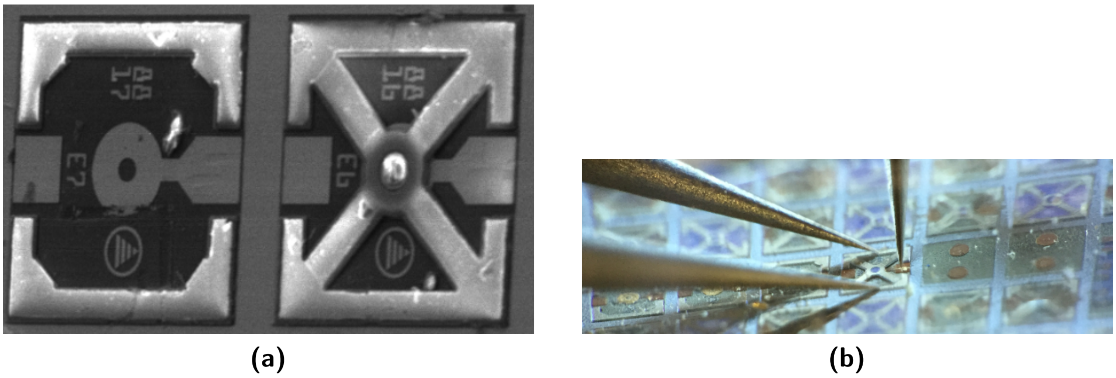

Figure 3.14: (a) SEM image of two on-wafer MEMS-VCSELs with broken membrane DBR and with membrane DBR (right), the circular n-contact can be seen. (b) The circular n-contact under the membrane facilitates electrical connections for a LDV experiment.

with V_{pp} as the peak-to-peak modulation voltage.

The exerted electrostatic force on the membrane and the corresponding motion is characterized by the LDV experiment[4] under atmospheric pressure. The VCSEL cavity is not pumped with any bias current and the wavelength of the sensing laser (Helium Neon laser with $\lambda = 633\,\mathrm{nm}$) is different from that of the MEMS-VCSEL. Thus, LDV directly measures the mechanical behavior of the membrane without any influence of optomechanical effects [72]. For an applied voltage of $V_{\mathrm{DC}} = 20\,\mathrm{V}$, $V_{\mathrm{pp}} = 1.5\,\mathrm{V}$, the motion of the membrane is examined by capturing its velocity signal. Figure 3.15a shows the normalized velocity signal of the membrane versus coarse modulation frequencies. Signals at 300 kHz and 1200 kHz are highest indicating two possible resonance frequencies of the membrane. To investigate further, time domain response of the membrane against an input signal with 300 kHz is measured. As shown in Fig. 3.15b, the membrane signal lags the input by $\approx \pi/2$, which is the fundamental characteristic under resonance condition. An additional single trace (red dotted trace) in Fig. 3.15a for $V_{\mathrm{DC}} = 20\,\mathrm{V}$, $V_{\mathrm{pp}} = 10\,\mathrm{V}$, $f_{\mathrm{mod}} = 300\,\mathrm{kHz}$ is shown to indicate the onset of higher-order harmonic (see at 600 kHz). For increasing signal modulation, thus, higher-order harmonics are excited. Obtaining the resonance frequencies more accurately, however, we measure the membrane signal against finely swept modulation frequencies. By tracking the peak of the membrane signal as illustrated in Fig. 3.16a, one can see two mechanical resonance frequencies at $\nu_{\mathrm{res},1} = 283\,\mathrm{kHz}$ and $\nu_{\mathrm{res},2} = 1215\,\mathrm{kHz}$ where $\nu_{\mathrm{res},1}$ is the 3rd harmonic of the fundamental resonance frequency, $\nu_{\mathrm{res},1}$.

---

[4] Polytec, OFV2502 Controller and OFV-534 Sensor-Head with Sensitivity of 25 mm/(s V)

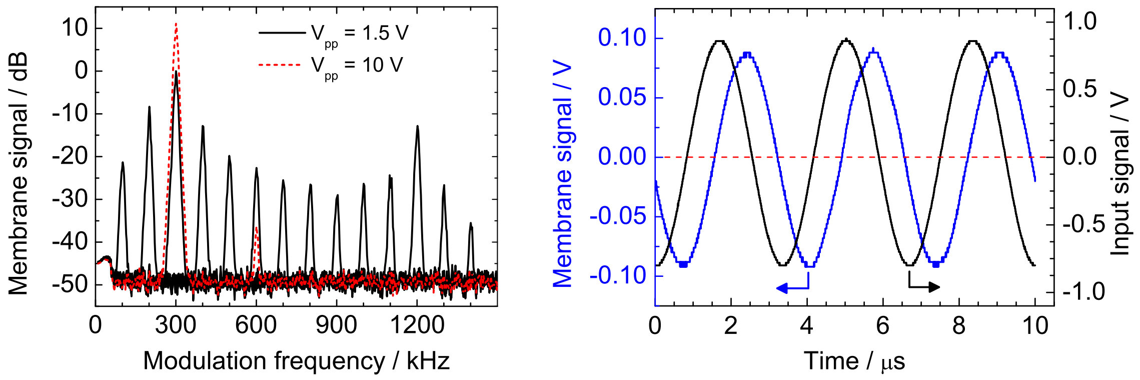

(a) (b)

Figure 3.15: (a) LDV velocity measurement shows the membrane signal as a function of coarsely swept modulation frequencies in atmospheric pressure (without injection current). (b) Time domain signals show that the membrane signal lags the input by $\approx \pi/2$ at 300 kHz.

Since mechanical or external noises can oscillate the membrane, they can cause cavity length fluctuations. This, in turn, results in wavelength and power fluctuations. The strength of the mechanical oscillations also depend on the mirror reflectivity and gain [73]. Based on this, the mechanical resonances can alternatively be measured as demonstrated in Ref. [66] by using a fixed-frequency laser feeding to a MEMS tunable Fabry-Pérot etalon. The latter is illustrated in the inset of Fig. 3.16a where the MEMS-VCSEL signal is detected by a fast PD, followed by an ESA. The fundamental resonance measured at 288 kHz matches closely to that obtained from the LDV experiment. This implies that the resonance frequencies can be determined likewise from the mechanical or electro-optical measurement. Since the MEMS-VCSEL is pumped, the latter includes the influence of optomechanical effects. Obtaining resonance peaks from the electro-optical measurement is best understood for another MEMS-VCSEL from a different wafer whose ESA spectra is displayed in Fig. 3.16b with $\nu_{\text{res},1} \approx 214\,\text{kHz}$ and $\nu_{\text{res},2} \approx 1250\,\text{kHz}$ ($I_\text{b} = 20\,\text{mA}$). This MEMS-VCSEL is employed for THz homodyne photomixng setup as will be discussed in Sec. 4.3. The observed spectra resemble the behavior as shown for the LDV measurement in Fig. 3.16a and the values of resonance peaks match closely to that reported for an electrostatically tunable MEMS-VCSEL in Ref. [13].

Since this chapter focuses the characteristics of MEMS-VCSELs belonging to the same wafer, the remaining mechanical parameters will be extracted for the MEMS-VCSEL used in the LDV experiment. The quality factor, Q of the membrane is given

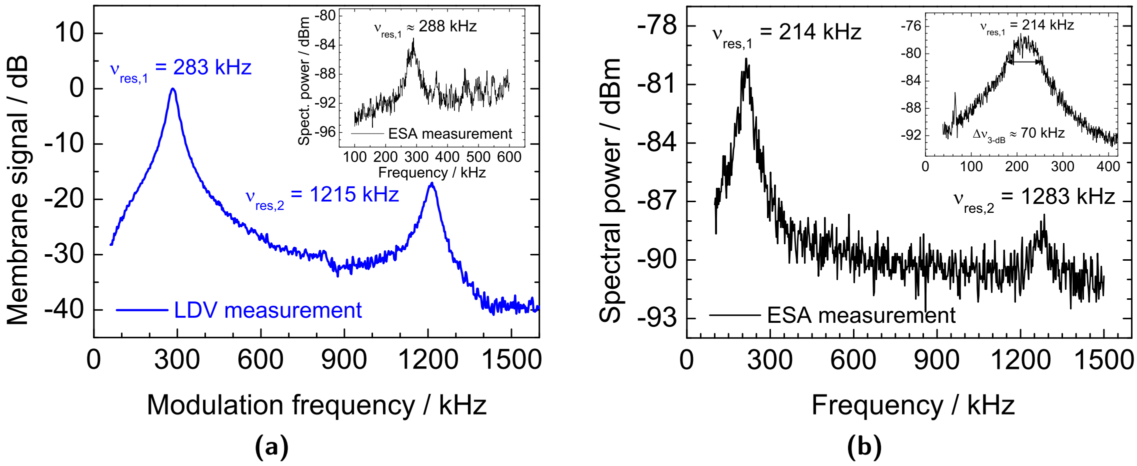

Figure 3.16: (a) LDV velocity measurement of the membrane as a function of finely swept modulation frequencies shows two resonance peaks ($I_b = 0\,\text{mA}$). The inset shows the fundamental resonance captured by an electro-optical measurement during the lasing operation (not from the LDV measurement). (b) Membrane resonances for another MEMS-VCSEL captured by an electro-optical measurement during lasing operation ($I_b = 20\,\text{mA}$). The inset shows a zoom into the fundamental resonance with a 3 dB bandwidth of 70 kHz.

by

$$Q = \frac{\nu_{\text{res},1}}{\Delta\nu_{\text{res}}} = \frac{\omega_{\text{res}}}{2\alpha_{\text{d}}}, \tag{3.16}$$

where $\omega_{\text{res}} = \sqrt{k_{\text{m}}/m}$ is the resonant (angular) oscillation frequency and $\alpha_{\text{d}} = R_{\text{m}}/2m$ is the damping factor [74]. Equation (3.16) yields a quality factor of $Q = 4.35$ with $\nu_{\text{res},1} = 283\,\text{kHz}$ and $\Delta\nu_{\text{res}} = 65\,\text{kHz}$ (see Fig. 3.16a). This supports the previous assumption of a weakly damped oscillator. Moreover with $\nu_{\text{res},1} = 283\,\text{kHz}$ and $m_{\text{m,eff}} = 0.34\,\mu\text{g}$, Eq. (3.14) yields a spring constant of $k_{\text{m}} = 1075.00\,\text{N/m}$. We will show in Sec. 3.3.1 that the spring constant has a direct consequence on the Brownian motion induced vibrations of the membrane which in turn affect the laser linewidth and stability.

3.3 Wavelength Stability Analysis

Wavelength fluctuations of MEMS-VCSELs are common due to the suspended membrane structure over half-VCSELs. The membrane is not immune to exter-

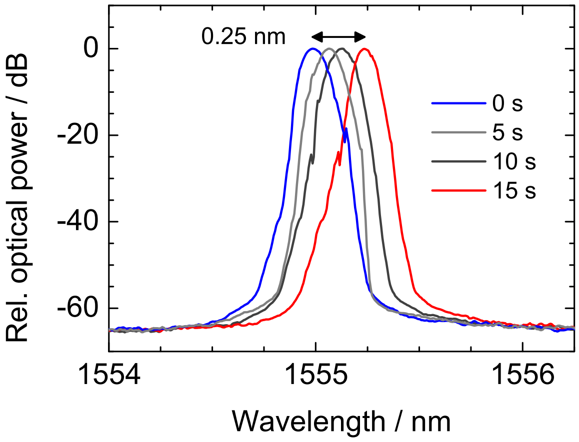

Figure 3.17: Emission spectra of a MEMS-VCSEL captured in every 5 s show an overall wavelength drifts of 0.25 nm for an observation period of 15 s.

nal disturbances such as vibrations, besides, the presence of many microforces acting on the membrane induce undesired deflections of the membrane. The overall motion is observed through wavelength drifts and fluctuations of MEMS-VCSELs. For instance, an OSA sweep of 50 ms as displayed by the blue trace in Fig. 3.17 shows the peak emission wavelength of a MEMS-VCSEL at 1554.98 nm ($I_\mathrm{b} = 20\,\mathrm{mA}$, $I_\mathrm{MEMS} = 0\,\mathrm{mA}$). Few emission spectra captured within a time span of 15 s show the wavelength drifts of 0.25 nm (31 GHz). A deep insight into the wavelength variations by various noise sources is presented in Ref. [75]. A comprehensive review article highlights the effect of noises by the types of various MEMS devices [76], whereas, these are addressed specifically for the MEMS-tunable Fabry-Pérot etalons [66] and MEMS-VCSELs [77]. In the following, different sources affecting the stability of MEMS-VCSELs are addressed.

3.3.1 Intrinsic Vibrational Noise

The membrane is prone to intrinsic Brownian motion induced vibrational noise [69]. This results in membrane fluctuations. Any system at thermal equilibrium with non-zero temperature T has an average energy of $\frac{1}{2}k_\mathrm{B}T$ in each degree of freedom where k_B is the Boltzmann constant. The associated potential energy of the membrane is $E_\mathrm{pot} = \frac{1}{2}k_\mathrm{m}\Delta x^2$. The mean-square displacement, $\langle \Delta x^2 \rangle$ of the membrane can be presented as

$$\frac{1}{2}k_\mathrm{m}\langle \Delta x^2\rangle = a\cdot\frac{1}{2}k_\mathrm{B}T, \tag{3.17}$$

where a represents the degrees of freedom of the membrane. In the following, we assume that the system is governed mainly by the fundamental oscillation with little influence of higher-order modes, hence, $a \approx 1$. If the membrane displaces by an amount of Δx with respect to its equilibrium position, Eq. (3.8) is rearranged to show the corresponding change in lasing frequency, $\Delta\nu$ as

$$\Delta\nu = \frac{2\nu\Delta x FSR_{\nu}}{c} \approx \frac{2c\Delta x FSR_{\lambda}}{\lambda^3}. \tag{3.18}$$

Inserting the expression of Δx from Eq. (3.17) in Eq. (3.18) yields for the root mean square (RMS) fluctuations as

$$\Delta\nu_{\mathrm{rms}} = \sqrt{< \Delta\nu^2 >} = \frac{2cFSR_{\lambda}}{\lambda^3}\sqrt{\frac{ak_{\mathrm{B}}T}{k_{\mathrm{m}}}}. \tag{3.19}$$

For the MEMS-VCSEL used in the LDV experiment with the set of values of $k_{\mathrm{m}} = 1075\,\mathrm{N/m}$, $T_{\mathrm{s}} = 295\,\mathrm{K}$, $FSR_{\lambda} = 82\,\mathrm{nm}$ and $\lambda = 1560\,\mathrm{nm}$, Eq. (3.19) predicts the Brownian motion induced fluctuations of $\approx 25.21\,\mathrm{MHz}$. These directly affect the linewidth of MEMS-VCSELs as we will discuss in Sec. 3.5. One way to reduce the fluctuations is to make the spring stiffer, or, a fast wavelength control circuit could compensate it. Such a control circuit for an electrostatically tunable MEMS-VCSEL shows a considerable reduction of the noise [78].

3.3.2 Acoustic Noise

Since we characterize on-wafer, unpackaged MEMS-VCSELs, unwanted membrane oscillations can take place through acoustic coupling of external vibrations [78]. Noise coupling through the optical bench is less likely due to its low cut-off frequency. In contrast, a membrane exposed to air might respond to ambient noises. The magnitude of these signals changes from day to day originating from varying electrical and mechanical environment of the laboratory. Figure 3.18 shows an OSA trace of a MEMS-VCSEL under ambient and intentional (with voice signal) acoustic noise. For the latter, vibration induced mechanical oscillations deforming the optical spectra are observed. Such a behavior bears the information that fluctuations of the membrane occur due to many microforces. Another possible reason for wavelength fluctuations is due to temperature fluctuations of the membrane itself through air drafts.

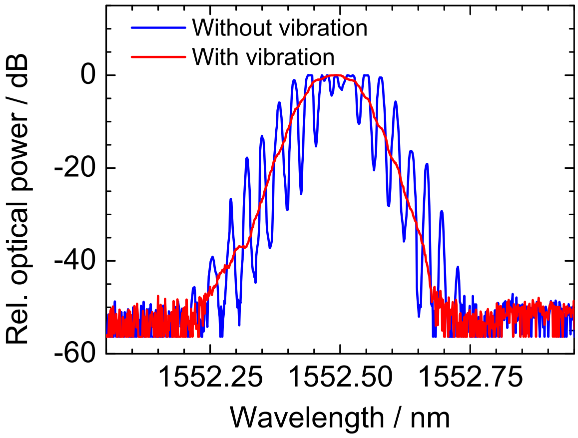

Figure 3.18: Vibrational characteristics of the membrane under acoustic coupling of a voice signal (blue), and without voice signal (red).

3.3.3 Optomechanical Effects

A significant micromechanical force is radiation pressure where light exerts a force onto the membrane causing mechanical oscillations. Such mechanical oscillation of a ultra-light-weight (130 pg) HCG mirror of a tunable VCSEL shows periodic oscillations of the wavelength and output power [73]. When the optical power inside the cavity, P_{cav} is incident onto the membrane, $P_{\mathrm{cav}} R_{\mathrm{DBR,t}}$ is the reflected light and $(1 - R_{\mathrm{DBR,t}}) \cdot P_{\mathrm{cav}}$ is the transmitted light as output, P_{opt}. The corresponding change in momentum per photon is $2\hbar k$ with $\hbar = h/2\pi$. As the photon flux is $\Phi = P_{\mathrm{cav}}/h\nu$, the total momentum change per second or equivalently, the radiation pressure F_{rp} is [66]

$$F_{\mathrm{rp}} = \frac{2P_{\mathrm{cav}}}{c} = \frac{2P_{\mathrm{opt}}}{c\,(1 - R_{\mathrm{DBR,t}})}. \tag{3.20}$$

If radiation pressure displaces the membrane by an amount Δx_{rp} about its equilibrium position, then $F_{\mathrm{rp}} = k_{\mathrm{m}} \Delta x_{\mathrm{rp}}$. Comparing this to Eq. (3.20), Δx_{rp} can be shown as

$$\Delta x_{\mathrm{rp}} = 2\frac{P_{\mathrm{cav}}}{c k_{\mathrm{m}}} = \frac{2P_{\mathrm{opt}}}{k_{\mathrm{m}} c\,(1 - R_{\mathrm{DBR,t}})}. \tag{3.21}$$

Under lasing operation, continuous pumping of the cavity increases the optical power, consequently F_{rp} also increases. For example, to reach the maximum average power of 1 mW of a MEMS-VCSEL with $R_{\mathrm{DBR,t}} = 99.5\,\%$, $k_{\mathrm{m}} = 1075\,\mathrm{N/m}$, Eq. (3.21) gives a value of $\Delta x_{\mathrm{rp}} \approx 1.24\,\mathrm{pm}$. This corresponds to a frequency deflection of about 16.2 MHz. Since the short optical resonator of the VCSEL requires very high reflective mirrors to sustain lasing, the cavity power might be significant (compared to its smaller geometry) to cause strong radiation force. In the following, we will investigate the validity of this statement for MEMS-VCSELs. Under the constant pumping, F_{rp} induced mirror displacement can be inferred by slight modification of Eq. (3.21) as

$$\Delta x_{\mathrm{rp}} = 2\frac{P_{\mathrm{cav}}}{ck_{\mathrm{m}}} = \frac{2\Delta P_{\mathrm{opt}}}{k_{\mathrm{m}}c\left(1 - R_{\mathrm{DBR,t}}\right)}, \tag{3.22}$$

where ΔP_{opt} accounts for the instantaneous power fluctuations. After the initial deflection of 16.2 MHz, as calculated from Eq. (3.21), periodic deflections of the mirror due to radiation pressure is less pronounced. This can alternatively be shown by computing the optical power level at which Δx_{rp} is equal to Δx from Eq. 3.17 as

$$\Delta P_{\mathrm{opt,eq}} = \frac{c\left(1 - R_{\mathrm{DBR,t}}\right)}{2}\sqrt{ak_{\mathrm{m}}k_{\mathrm{B}}T}, \tag{3.23}$$

where $\Delta P_{\mathrm{opt,eq}}$ is the required power fluctuations by F_{rp} to produce the equivalent mirror displacement from thermal noise. Using the identical set of parameters in Eq. (3.23), a value of $\Delta P_{\mathrm{opt,eq}} \approx 1.57\,\mathrm{mW}$ is obtained. Such a number is not realistic, and therefore Δx_{rp} is found insignificant for the presented MEMS-VCSELs under constant pump of operation.

3.3.4 Temperature Fluctuation Noise

Based on the statistical nature of heat exchange with the ambient environment, the membrane exhibits random fluctuations in temperature. The mean square temperature fluctuations are proportional to the operating temperature of MEMS-VCSELs and inversely proportional to the heat capacity of the membrane [75]. Substrate temperature fluctuations can also be coupled to the membrane inducing temperature fluctuations which are a function of the thermal time constant of the membrane, its thermal conductance, and the resolution of the temperature-control system [79]. The laser itself produces noise due to changes in its cavity under lasing operation and can be expressed as an effective noise temperature. Assuming that all the noise sources are statistically uncorrelated, the total noise temperature fluctuation $\Delta T_{\mathrm{total}}$ is given by the geometrical sum of the individual noise temperature fluctuation ΔT_{i} as [79]

$$\Delta T_{\mathrm{total}} = \sqrt{\sum \Delta {T_{\mathrm{i}}}^{2}} \qquad \text{with} \qquad i = 1, 2, 3, \ldots \tag{3.24}$$

An etalon-based commercial wavelength locker (WL) can detect wavelength fluctuations of a laser about the first wavelength of operation [78, 80]. The output of the

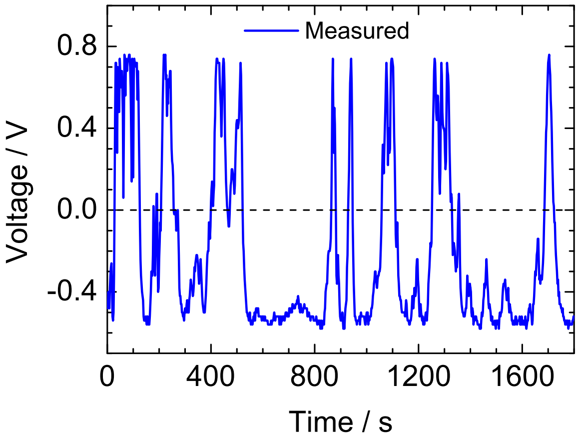

Figure 3.19: The output power of the MEMS-VCSEL feeding to an etalon shows the voltage (wavelength) variations around zero voltage corresponding to the first wavelength of operation.

WL feeding by the MEMS-VCSEL is converted into a voltage by a trans-impedance amplifier and captured by a time domain oscilloscope[5] in every two seconds as displayed in Fig. 3.19. The wavelength fluctuations are observed by the change of the voltage around the zero voltage corresponding to the first wavelength. Obviously the wavelength fluctuations are dominated by the slow drifts. Most of the unwanted noise sources discussed above cannot explain the slow drifts of MEMS-VCSELs in excess of gigahertz. For the wavelength drifts of the MEMS-VCSEL as shown in Fig. 3.17, Eq. (3.8) yields a corresponding mechanical deflection of 2.38 nm of the membrane by using $\Delta\nu = 31\,\text{GHz}$, $\lambda = 1554.98\,\text{nm}$ and $FSR_\nu = 10.13\,\text{THz}$ ($FSR_\lambda = 82\,\text{nm}$). To find the associated length extension, Δl_m of the suspended beam assisting this vertical deflection, the calculation will be arranged with a trapezoidal approximation of the membrane [81]. For a cross section of the membrane, the suspended beams are the legs, the circular membrane and the surface of half-VCSEL are the short-base and long-base, respectively. By forming a right-angled triangle with one arm equal to the air gap of 6.1 µm (height of the trapezoid) and $l_\text{m} = 150\,\mu\text{m}$ as hypotenuse, Δl_m of $\approx 96.80\,\text{pm}$ is calculated. The corresponding temperature fluctuation noise is calculated by [81]

$$\Delta T_\text{total} = \frac{\Delta l_\text{m}}{\alpha_\text{SiN} l_\text{m}}. \tag{3.25}$$

For $\alpha_\text{SiN} = 2.3 \cdot 10^{-6}/\text{K}$, Eq. (3.25) predicts of $\Delta T_\text{total} \approx 280.6\,\text{mK}$. Such a small temperature fluctuation can reasonably be produced causing tens of gigahertz of

---

[5] Tektronix, TDS 210

wavelength drifts.

3.4 Wavelength Control Mechanism

Wavelength control circuits based on commercial WL modules are reported in Refs. [78, 80]. For the present work, we have developed a WL-based wavelength control circuit where a comparator-tracked error voltage is added to the membrane current only when a MEMS-VCSEL is brought near a DWDM international telecommunication union (ITU) channel [36]. Thus, the circuit can switch and lock MEMS-VCSELs to any DWDM channel. The comparator is of Schmitt-trigger configuration. This circuit could potentially attain faster-switching speed, needs no look-up table and requires no slope selections of the error voltage. The switching (tuning) resolution of the designed circuit is based on the 100 GHz FSR of an etalon inside the WL; however, commercial WL modules with any FSR can directly be inserted into the circuit to attain the desired tuning resolution.

3.4.1 Functional Blocks of the Wavelength Control Circuit

The printed circuit board (PCB) of the developed wavelength control circuit is presented in App. A. Figure 3.20 schematically describes the simplified functional blocks of the control circuit. The main part of the control circuit is a commercially available broadband telecom WL module[6]. One percent of the total power of a MEMS-VCSEL is provided as input to the WL where the optical power is split into two branches. One of these branches is directed to an etalon, followed by a p-i-n PD. Fabry-Pérot oscillations inside the etalon cause frequency-periodic oscillations of the transmission. The peak-to-peak distance of the transmission defines the etalon's FSR which is 100 GHz (≈ 0.8 nm) for this specific WL. The corresponding PD current, I_{eta}, thus is a function of the wavelength of the input optical signal. The other branch directly goes to a reference p-i-n PD whose current I_{ref} is only a function of the power, thus used as the reference. The lock points are defined on the positive slopes of the etalon's transmission function where $dI_{\mathrm{eta}}/df > 0$. The circuit generates a normalized voltage, V_{log} after a logarithmic transimpedance amplifier as

$$V_{\mathrm{log}} = (1V) \cdot \log\left(I_{\mathrm{eta}}/I_{\mathrm{ref}}\right). \tag{3.26}$$

---

[6] JDS Uniphase, WL5102-Z1

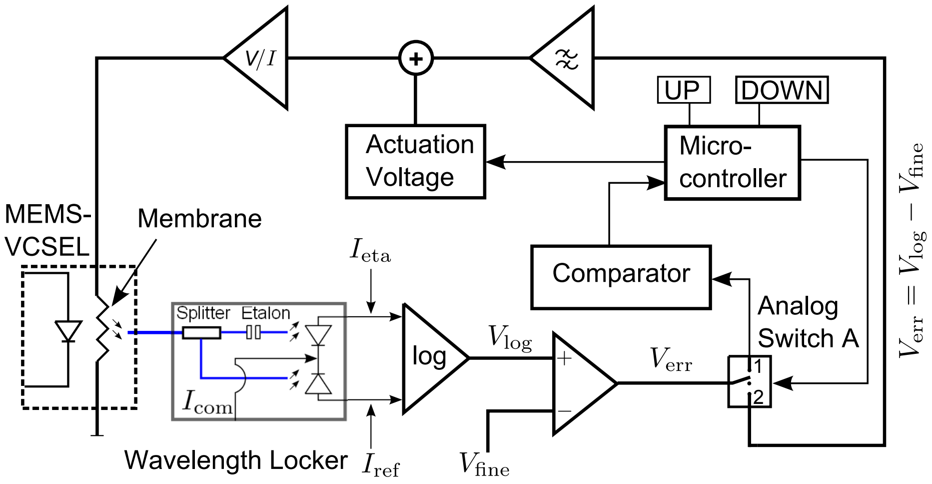

Figure 3.20: Schematic of the WL-based wavelength control circuit for locking and switching.

This output is given to an instrumentation amplifier whose output is the error voltage

$$V_{\text{err}} = V_{\text{log}} - V_{\text{fine}}, \tag{3.27}$$

where V_{fine} is the microcontroller/manually controlled offset voltage for fine-tuning. 100 GHz-spaced sweepings are accomplished by successive pressing of a UP button. At the beginning of the operation, the switch is set to position A=1 so that the comparator circuit can compare V_{err} in the event we execute a locking command. To demonstrate a single locking procedure to the nearest higher-wavelength channel, the UP command initiates the microcontroller to increase the actuation voltage (actuation current) of the MEMS-VCSEL in steps of few millivolts each. It is explicit from the definition that V_{err} is also a function of wavelength. Therefore, 100 GHz-spaced periodic peaks of V_{err} occur with increasing membrane current. These peaks are the direct indications that DWDM channels are nearby. The comparator is devised in a way that it detects the occurrence of the oncoming peaks. After each peak detection by the comparator, a signal is addressed to the microcontroller which then stops increasing the actuation voltage for the membrane, placing the switch to $A = 2$ so that V_{err} is added to the main actuation voltage. The MEMS-VCSEL is then locked to the next channel. Under normal operation, V_{fine} is set to zero. Whenever a channel lock point error (slight difference in wavelength) occurs due to self-induced temperature variation error of the WL itself, V_{fine} is tuned to compensate this. V_{fine} can also be used for tuning resolution of 1 GHz in conjunction with an additional functional block in the circuit with slope selection mechanisms of the error voltage.

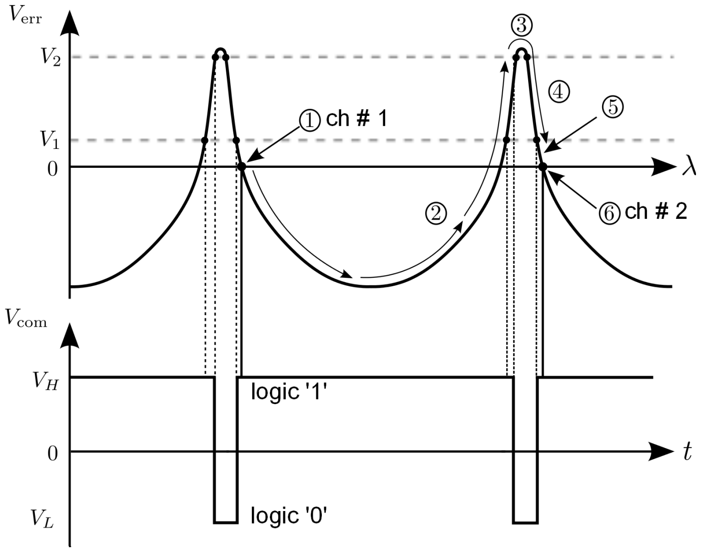

Figure 3.21: Exemplary switching procedures along 100 GHz-spaced DWDM channels.

In Fig. 3.21, channel switching is further explained. The exemplary channels represented here are in wavelength domain; therefore those are placed on the negative slopes ($dI_{\mathrm{eta}}/d\lambda < 0$) of V_{err}. Two transition voltages of V_1 and V_2 are defined for the comparator circuit so that the output can swing between its positive and negative saturation voltages of V_{H} and V_{L}, respectively. When the MEMS-VCSEL is locked at channel 1 so that V_{err} ($\approx 0\,\mathrm{V}$) $< V_1$, the comparator outputs V_{H} which is read as a logical 1 by the microcontroller. When a UP command is received, the microcontroller sets the switch to position A = 1 and immediately ramps up the actuation voltage. As a result, V_{err} starts decreasing, reaching the minimum and then rises along the positive slope. On this course, when $V_{\mathrm{err}} > V_1$, no change in logic level occurs. A change in logic level from $1 \rightarrow 0$ occurs when V_{err} crosses V_2 on the positive slope (comparator's negative saturation voltage, V_{L} is read as logical 0). The next change in logic level from $0 \rightarrow 1$ occurs when V_{err} crosses V_1 on the negative slope. The microcontroller is programmed to stop increasing the actuation voltage at this point, places the switch to A = 2 and thus, locking to the next channel is accomplished. The channel-to-channel binary logic changes are in a sequence of $1 \rightarrow 0 \rightarrow 1$. The complete switching procedure is demonstrated in Tab. 3.5. The same procedures are valid for moving along the channels towards shorter wavelengths by using a DOWN button.

Table 3.5: Locking and switching procedures along DWDM ITU channels.

Number	MEMS Actuation Voltage	Switch Position	V_{err}	Logic Level
1	fixed (locked to ch # 1)	A=2	$\approx 0 < V_1$	1
2	increase	A=1	$< V_1$	**1**
3	increase	A=1	$> V_2$	0
4	increase	A=1	$< V_2$	**0**
5	increase	A=1	$< V_1$	1
6	fixed (locked to ch # 2)	A=2	≈ 0	**1**

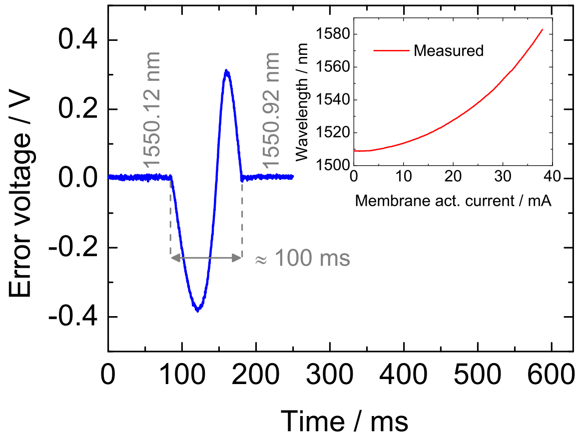

Figure 3.22: The slowest channel-to-channel switching time of 100 ms is around lower membrane current of operation. The switching time gets faster with increasing membrane current as the emission wavelength changes quardatically to it (see the inset).

3.4.2 Control Circuit Performance

The 3 dB cut-off frequency of the membrane is 258.65 ± 7.09 Hz (see Sec. 3.2.3). Therefore, the ideal channel-to-channel switching time is ≈ 4 ms. As displayed in Fig. 3.22, the slowest switching-speed measured for this circuit is 100 ms at low membrane current of operation. According to $\lambda \sim I_{\mathrm{MEMS}}^2$ relation (see the inset), a single switching requires more voltage steps (requiring more time) with low current of operation, whereas it gets faster with high current of operation (requiring less voltage steps) approaching a speed of approximately 4 ms. Using 100 GHz-

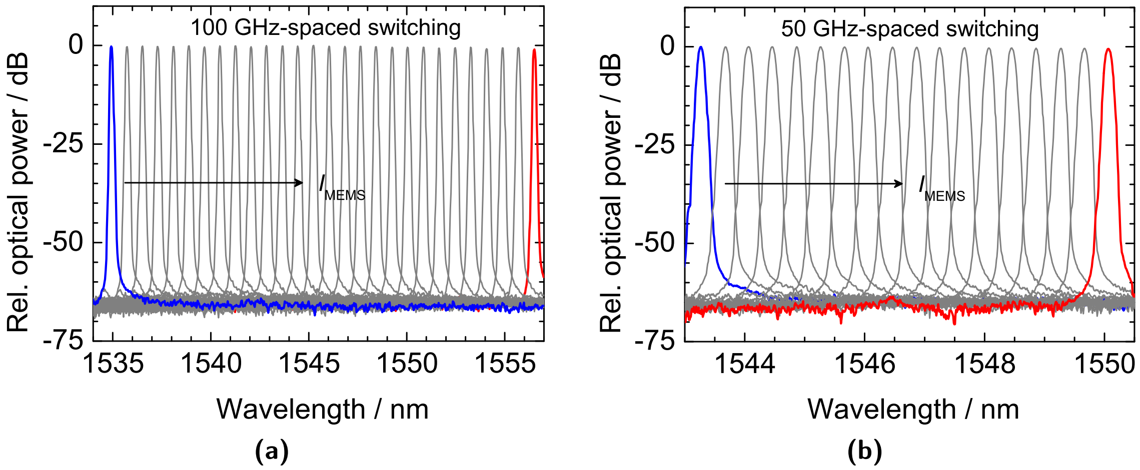

Figure 3.23: (a) 100 GHz-spaced channel-to-channel switchings for a MEMS-VCSEL while at each channel, the MEMS-VCSEL is wavelength-stabilized. (b) 50 GHz-spaced switchings for the same MEMS-VCSEL.

FSR WL, Fig. 3.23a shows 100 GHz-spaced tuning of a MEMS-VCSEL covering an exemplary tuning range of 21.60 nm. The entire tuning range can be tuned likewise. Figure 3.23b shows 50 GHz-spaced tuning of the same MEMS-VCSEL using 50 GHz FSR WL. Therefore, the highest resolution tuning conducted by this circuit depends on commercially available WL modules with the lowest FSR. In Fig. 3.24a, the wavelength drifts of an unlocked MEMS-VCSEL is compared to the case of locking at a DWDM channel of $\lambda = 1576.20\,\text{nm}$. Under locking, the drifts of more than few tens of GHz (see Fig. 3.17) are compensated to ±600 MHz for an observation period of 6 h. The control circuit compensates the slow drifts with $f \leqslant f_{\text{mod,3-dB}} = 258.65 \pm 7.09\,\text{Hz}$ due to the thermal inertia of the membrane. For electrostatically tunable MEMS-VCSELs, faster fluctuations can be canceled using a fast control circuit with a locking bandwidth significantly above the mechanical resonance frequencies of the membrane DBR.

The strength of the feedback of the control circuit is further characterized by using the temperature behavior of a MEMS-VCSEL. As shown in Fig. 3.24b, the circuit compensates the expected blueshift for a sudden increase of the substrate temperature from 23 °C to 28 °C by a rapid increase of the membrane current. Similarly, wavelength drifts due to external disturbances are well compensated by the excellent feedback implemented in the designed circuit.

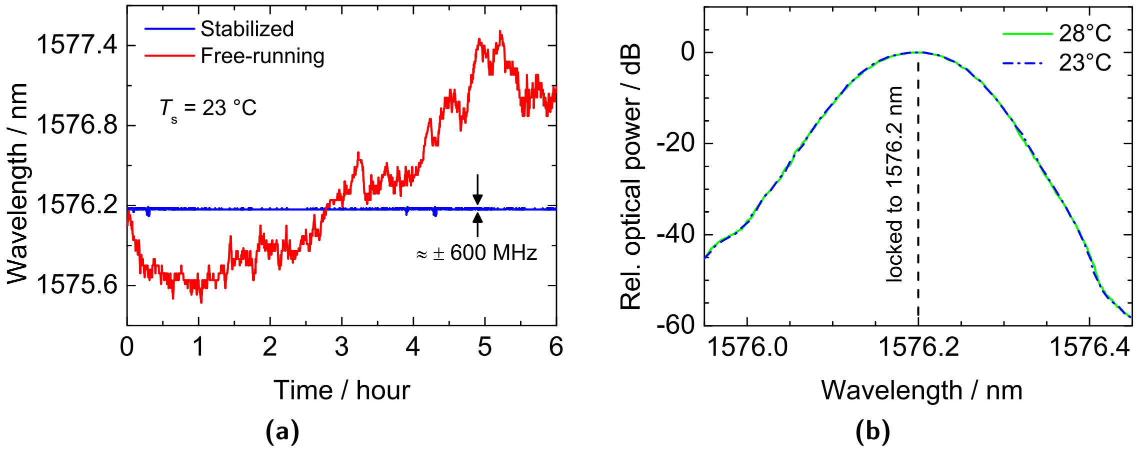

(a) **(b)**

Figure 3.24: (a) Wavelength drifts of a MEMS-VCSEL under free-running operation (red trace) and stabilized operation (blue trace). (b) The feedback strength of the wavelength control circuit is tested with blueshift compensation.

3.5 Emission Linewidth Analysis

THz signals generated by CW photomixers feature a linewidth that corresponds to the combined linewidth of two lasers. Influences by the photomixing process are typically negligible. For many applications, in particular for THz spectroscopy, narrow linewidth and frequency stability of lasers are highly important. As an example, most polar gases feature the respective linewidth in the few GHz ranges under normal conditions [82]. At lower pressures in the millibar range, the linewidths reduce to a few tens of kHz [82], requiring additional linewidth stabilization techniques. As discussed in Sec. 2.2.4, non-tunable VCSELs show a typical linewidth in the range of a few MHz which is attributed to the high-quality factor of the laser cavity. Such linewidth would be sufficient for THz spectroscopy experiments under normal pressure. The suspended membrane of the MEMS-VCSELs, however, is prone to additional noise influences that lead to a larger linewidth. In the following, we will derive the influence of the mechanical and thermal noises on the linewidth of MEMS-VCSELs and compare the findings to the experimental results.

The linewidth of MEMS-VCSELs is measured with the DSH technique as outlined in Sec. 2.2.4. The output power is coupled to a SMF via a lens with AR coating, followed by an in-line isolator to reduce back-reflections [83]. Contact needles for the membrane are intentionally disconnected during this experiment. Above the threshold, the emission wavelength is around 1560 nm with a substrate temperature

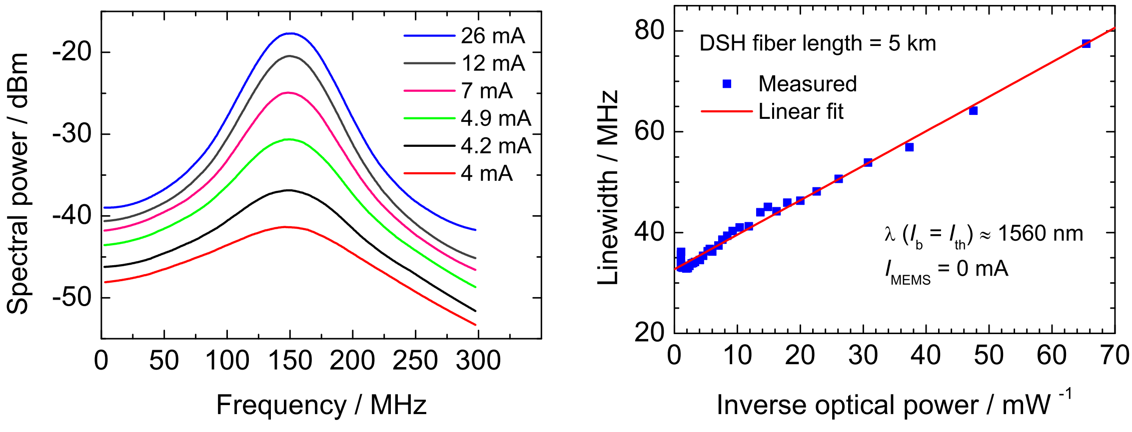

(a) **(b)**

Figure 3.25: (a) Measured DSH spectra for different bias currents. (b) MEMS-VCSEL actual linewidth, $\Delta\nu_{\mathrm{LW}}$ against inverse optical power ($I_{\mathrm{MEMS}} = 0\,\mathrm{mA}$).

of $T_{\mathrm{s}} = 22\,°\mathrm{C}$. The length of the decorrelation fiber of the DSH setup provides a time delay of $\tau_{\mathrm{d}} = 25\,\mu\mathrm{s}$. This sufficiently long fiber allows for measuring the linewidth and noise influences with a frequency above $f_{\mathrm{d}} = 1/\tau_{\mathrm{d}} = 40\,\mathrm{kHz}$ [16, 84]. In particular, this also includes the mechanical fluctuations of the membrane at 283 kHz (see Sec. 3.2.5). Noise frequency of $f < f_{\mathrm{d}}$ will partially contribute. The intrinsic linewidth of lasers is of Lorentzian shape associated with white frequency noise. For MEMS-VCSELs, perturbations of the mirror due to the Brownian motion induced vibrations, external and internal microforces, change of laboratory environment (see Sec. 3.3) are typically of statistic nature featuring a Gaussian spectrum which is of $1/f$ nature. The actual linewidth, $\Delta\nu_{\mathrm{LW}}$, therefore, has a combined profile. A Voigt profile can interpret the power spectral density (PSD) of the DSH signal with the weighted contribution of the Gaussian and Lorentzian profiles which is given by [16]

$$\Delta\nu_{\mathrm{V,DSH}}\left(f_{\mathrm{d}}\right) = 0.5346\Delta\nu_{\mathrm{L}} + \sqrt{0.2166\Delta\nu_{\mathrm{L}}^2 + \Delta\nu_{\mathrm{G}}\left(f_{\mathrm{d}}\right)^2}, \tag{3.28}$$

where $\Delta\nu_{\mathrm{V,DSH}}$ is the FWHM of the DSH signal fitted with a Voigt profile. Since the observed PSD of the DSH signal is self-convolution of $\Delta\nu_{\mathrm{LW}}$, it is estimated from the subsequent Voigt fit as $\Delta\nu_{\mathrm{LW}} = \Delta\nu_{\mathrm{V,DSH}}/\sqrt{2}$. Figure 3.25a shows several measured DSH spectra (smoothed) of a MEMS-VCSEL as a function of frequency with increasing bias current. By individual Voigt fit to all of the DSH spectra, the linewidth is extracted and plotted as a function of the reciprocal power, $1/P_{\mathrm{out}}$ of the MEMS-VCSEL. This is depicted in Fig. 3.25b. Since $\Delta\nu_{\mathrm{LW}}$ scales almost linearly with $1/P_{\mathrm{out}}$ [85], it becomes smaller with higher energies in the resonator.

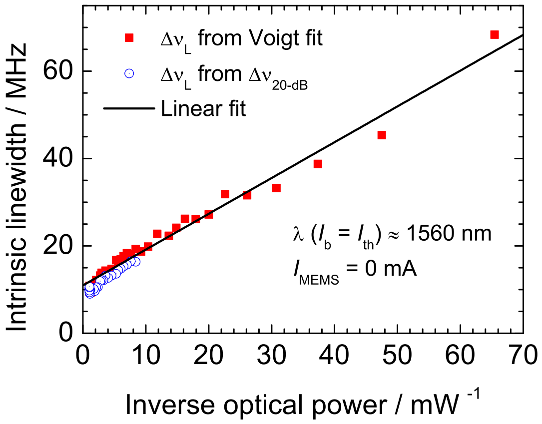

Figure 3.26: Intrinsic (Lorentzian) linewidth, $\Delta\nu_\mathrm{L}$ of the MEMS-VCSEL obtained from the Voigt fit and −20 dB bandwidth of the DSH spectra.

A slight deviation from the linearity is pronounced above 20/mW which is due to the linewidth enhancement factor. At highest powers, however, the linewidth increases again, potentially due to the increased heating of the laser cavity. Before this broadening, the lowest value of $\Delta\nu_\mathrm{LW} = 33 \pm 0.02$ MHz with $I_\mathrm{b} = 16$ mA–18 mA is reached. Figure 3.25b also shows the linear fit to the experimental data intersecting the y-axis ($P_\mathrm{out} = \infty$) with a residual linewidth of 32.71 ± 0.25 MHz. The fit line has a slope of $\Delta\nu_\mathrm{LW} \cdot P_\mathrm{opt} = 0.68 \pm 0.01$ MHz · mW representing the linewidth-power product of this MEMS-VCSEL.

Figure 3.26 shows the intrinsic linewidth profile of the MEMS-VCSEL as a function of the reciprocal power estimated from the Voigt fits of the DSH spectra. Figure 3.26 also shows the intrinsic linewidth profile estimated from the −20 dB bandwidths of the DSH spectra (see Sec. 2.2.4), however, $\Delta\nu_\mathrm{L}$ estimation for lower I_b is not possible due to the poor dynamic range (< 20 dB) of the DSH spectra. The two sets of data correlate very well. The linear fit to the data from Voigt fit intersects the y-axis with a residual value of 10.96 ± 0.41 MHz. The geometric average of this value and the derived Brownian motion induced mirror vibrations of 25.21 MHz from Sec. 3.3.1 equals to 27.48 ± 0.16 MHz which is in fair agreement with the residual linewidth of 32.71 ± 0.25 MHz as obtained from Fig. 3.25b.

It is of particular importance for tunable THz photomixing to see how the linewidth changes with electrothermal tuning. Due to the mechanical failure of the heating electrodes of the MEMS-VCSEL as shown in Fig. 3.25, we demonstrate the linewidth as a function of the membrane actuation current with an example of another MEMS-VCSEL from the same wafer. Figure 3.27 shows the linewidth and corresponding emission wavelength as functions of the membrane current. The

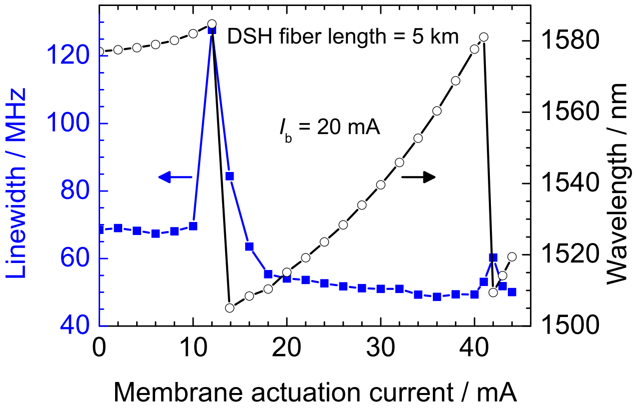

Figure 3.27: Linewidth over the tuning range as a function of the membrane actuation current with $I_\mathrm{b} = 20\,\mathrm{mA}$.

linewidth broadening towards the both edges of tuning range is due to the higher mirror losses as well as cavity detuning induced lower gain seen by the mode. At both ends of the tuning range, the sharp rise of the linewidth indicates longitudinal mode-hop. For the desired wavelength range covered by an EDFA from 1530 nm–1565 nm, the linewidth remains below 50 MHz. The lowest value of $\approx$ 48 MHz around $\approx$ 1560 nm is obtained with $I_\mathrm{MEMS} = 36\,\mathrm{mA}$. When we compare this value to the lowest linewidth of 33 ± 0.02 MHz from Fig. 3.25b, the difference constitutes to characterizing a different MEMS-VCSEL with different mass and geometry of the membrane on the one hand. On the other hand, further Gaussian noises originate from various sources, such as the use of a second LDC biasing the membrane and spurious noise pickups by the exposed contact needles of the membrane. Day to day change of the laboratory environment also influences the measured linewidth. However, the spurious noises can be considerably minimized with the packaging of MEMS-VCSELs.

3.6 Beat Signal Quality

Many applications, including THz spectroscopy, require long-term frequency stability of the lasers. It is worth to mention that the employed DSH technique records the linewidth on the time scale of 25 µs (40 kHz) generated by the 5 km fiber-optic delay. Therefore, slower drifts cannot be recorded because the two heterodyned signals remain correlated within the respective time scale. The developed wavelength control circuit [36] employing electrothermal feedback prevents long-term drifts of

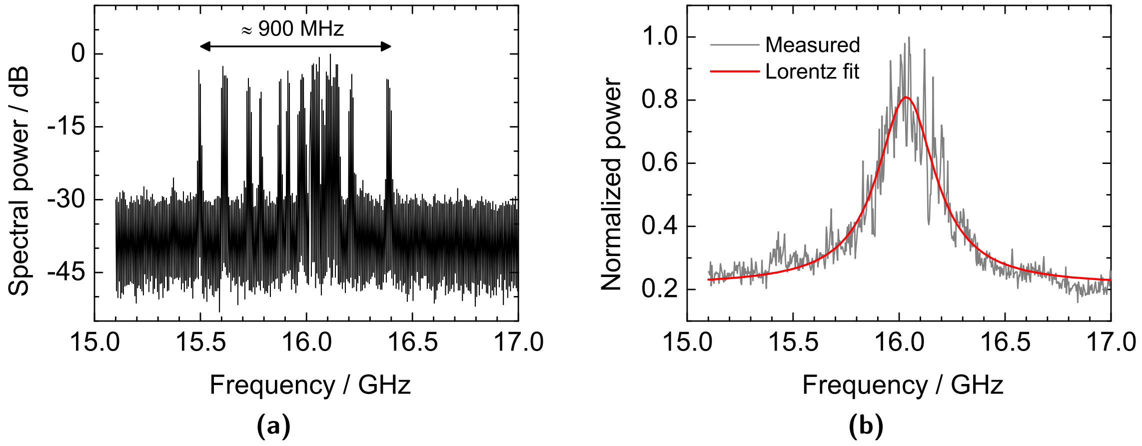

Figure 3.28: (a) Wavelength/frequency fluctuations of the heterodyned beat signal of the DFB laser and wavelength-locked MEMS-VCSEL. (b) Lorentzian fit to the time averaged beat signal shows an effective 3 dB fluctuation bandwidth of 331.91 ± 9.34 MHz.

MEMS-VCSELs. The electrothermal frequency response as shown in Fig. 3.11b permits the control circuit suppressing noise sources with frequencies below $f_{\text{mod, 3-dB}}$. However, noise sources with frequencies above $f_{\text{mod, 3-dB}}$ cannot be compensated by the developed circuit. We, therefore, expect that the MEMS-VCSELs fluctuate around the locking point. To measure the low-frequency stability, a MEMS-VCSEL is wavelength-locked and optically beat with a DFB laser which has a linewidth of ≈ 2 MHz and a long-term stability of the same order. An ESA trace with a sweep time of 50 ms is displayed in Fig. 3.28a with the instantaneous, i.e., short-time-scale beat signal bandwidth of ≈ 900 MHz. Several frequency jumps can be observed originated from the frequency drifts of the MEMS-VCSEL. These drifts occur due to several noise sources, such as spurious noise pickups by the contact needles connecting to the membrane, acoustic excitations of the membrane itself, and also due to the temperature drifts. To examine the associated long-time-scale signal, the signal as shown in Fig. 3.28a is time-integrated for 20 s. The corresponding ESA trace in Fig. 3.28b displays the long-term stability of the beat signal with a 3 dB fluctuation bandwidth of 331.91 ± 9.34 MHz. Since the DFB laser features a long-term linewidth of only ≈ 2 MHz, the fluctuation bandwidth of 331.91 ± 9.34 MHz arises solely from the drifts of the MEMS-VCSEL. Though this is about an order of magnitude larger than the VCSEL's linewidth, it is still sufficient for THz spectroscopy at ambient pressure and temperature. Faster frequency fluctuations can be filtered out by a control circuit covering the mechanical bandwidth of the fluctuations based on electrostatic feedback for electrostatically tunable MEMS-VCSELs. In that case, those MEMS-VCSELs could be conveniently stabilized towards the respective few tens of MHz linewidth.

3.7 Summary and Outlook

This chapter provides an insight into the static characterization of MEMS-VCSELs from a single wafer. Maximum output power of a MEMS-VCSEL coupled to a MMF is in the range of 1 mW with tuning range exceeding 80 nm corresponding to a bandwidth greater than 10 THz. The operating voltage remains below 2 V due to the incorporation of the BTJ. Besides the standard characterization, deep investigations are carried out to extract several relevant parameters of the MEMS-VCSELs. The mechanical resonance frequency of about 283 kHz is confirmed by both the LDV and electro-optical experiments. However, the exact value greatly depends on the mass and geometry of the membrane, which could potentially vary from device to device due to the fabrication inaccuracies or from the inhomogeneity of the wafer. There are inevitable Brownian vibrations, i.e., thermal noise of the membrane, which is inversely proportional to the membrane spring constant. Thermal noise, as well as different microforces acting on the membrane, destabilize the wavelength of the MEMS-VCSELs and directly affects the linewidth. The associated instability ranges from slow drifts to fast fluctuations. Wavelength drifts can be lessened by packaging the MEMS-VCSELs, though, practical applications will always require the wavelength control circuit for an effective wavelength stabilization. We develop a wavelength control circuit which effectively compensates the wavelength instabilities up to $f_{\text{mod, 3-dB}} = 258.65 \pm 7.09\,\text{Hz}$ limited by the thermal response of the membrane. The fluctuations greater than $f_{\text{mod, 3-dB}}$ can be compensated with a control circuit covering the bandwidth of these fluctuations. Such a control circuit can only be developed for electrostatically tunable MEMS-VCSELs.

The linewidth of less than 50 MHz is confirmed for a MEMS-VCSEL over the wavelength range of an EDFA from 1530 nm–1565 nm. For packaged MEMS-VCSELs with uniform membrane geometry, the linewidth can be as low as 33 MHz for electrostatically tunable MEMS-VCSELs. Table 3.6 summarizes the major parameters investigated for the MEMS-VCSELs from a single wafer. Among those, the CW broadband tuning with high SMSR as well as linewidth with few tens of MHz are advantageous for the application of THz photomixing. In the next chapter, we will show how the broadband tuning of MEMS-VCSELs benefits tunable THz photomixing.

Table 3.6: Key investigated parameters for MEMS-VCSELs belonging to the same wafer.

Parameter	Measured
SMF Coupled Output Power, P_{opt}	$1 \pm 0.3\,\text{mW}$
FSR	$82 \pm 1\,\text{nm}$
Maximum Tuning Range	$81 \pm 1\,\text{nm}$
SMSR over the Tuning Range	$50 \pm 5\,\text{dB}$
Linewidth over the Tuning Range, $\Delta\nu_{\text{LW}}$	$50 \pm 10\,\text{MHz}$
Tuning Speed, $f_{\text{mod, 3-dB}}$	$258.65 \pm 7.09\,\text{Hz}$
Fundamental Resonance Frequency, $\nu_{\text{res},1}$	$283 \pm 70\,\text{kHz}$
Quality Factor, Q	4.35 ± 1.3
Membrane Spring Constant, k_{m}	$1075 \pm 400\,\text{N/m}$

4 MEMS-Tunable VCSELs for THz Photomixing

This chapter first discusses the theoretical fundamentals of photomixing principle followed by THz signal generation and radiation by a CW photomixer. The remaining part of this chapter addresses MEMS-VCSELs-driven tunable THz photomixing system. The first photomixing setup with its first variant reports tunable THz signal generation with a photomixer driven by a MEMS-VCSEL optically heterodyned with a non-tunable VCSEL in direct power detection mode with a zero-bias Schottky diode. In the second variant of this setup, the same photomixer is driven by the optical beat of the MEMS-VCSEL and a DFB laser replacing the non-tunable VCSEL for the same type of detection. The second photomixing setup demonstrates tunable THz signal generation with the photomixer driven by a MEMS-VCSEL and a DFB laser in homodyne field detection mode with a photoconductor. In this configuration, the polarization stability of the MEMS-VCSEL is utilized.

4.1 The Principle of Photomixing

For photomixing, two interfering laser beams with the same polarization and frequencies of $\omega_1 = \omega + \frac{1}{2}\omega_{\mathrm{THz}}$ and $\omega_2 = \omega - \frac{1}{2}\omega_{\mathrm{THz}}$, respectively, are optically heterodyned. The superposition of these two laser beams yields the heterodyned electric field, $E_{\mathrm{het}}\,(t)$ as

$$E_{\mathrm{het}}\,(t) = E_1 \exp\left(i\omega_1 t\right) + E_2 \exp\left(i\omega_2 t\right), \tag{4.1}$$

where E_1 and E_2 are the respective electric fields of the laser beams. For $E_1 = E_2 = E_0$ yields the total heterodyned power, P_{het} as

$$\begin{aligned} P_{\mathrm{het}}\,(t) \sim E_{\mathrm{het}}\,(t) \cdot E^{*}_{\mathrm{het}}\,(t) = E_0^2 + E_0^2 + 2E_0^2 \cos[(\omega_1 - \omega_2)\,t] \\ \Rightarrow P_{\mathrm{het}}\,(t) = 2P_0[1 + \cos\left(\omega_{\mathrm{THz}} t\right)] \end{aligned}, \tag{4.2}$$

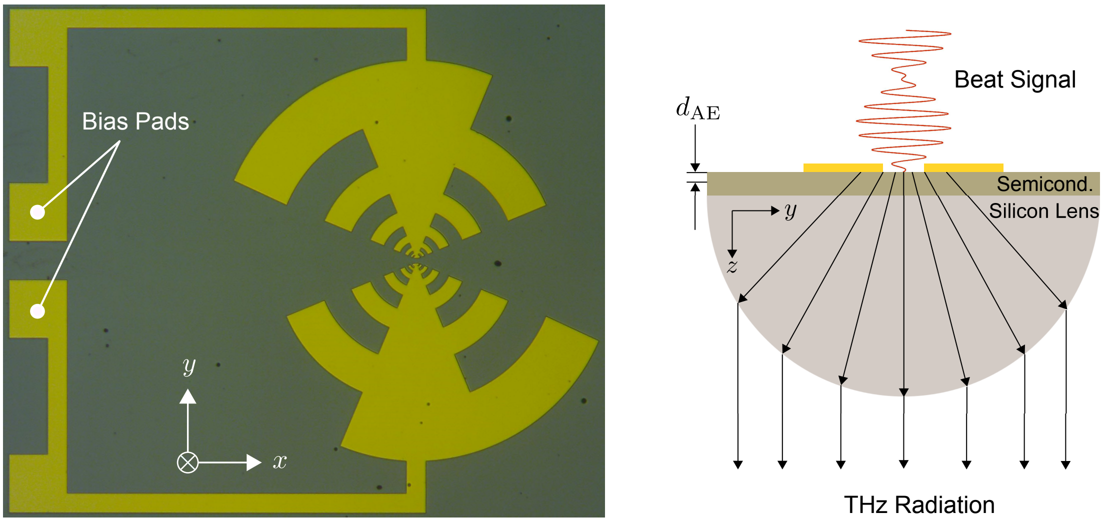

Figure 4.1: The test structure of an exemplary photomixer. The photocurrent generated by the incident beat signal is fed to an antenna converting the AC component of the photocurrent into free-space THz emission through a silicon lens.

with E^*_{het} is the complex conjugate of E_{het} and $P_0 \sim E_0^2$ is the optical power of each laser. The term $2P_0$ in Eq. (4.2), therefore, corresponds to the direct power, i.e., intensity detection of the two lasers. The remaining sinusoidal term modulates the intensity with $\omega_1 - \omega_2 = \omega_{\mathrm{THz}}$.

If the power and/or the polarization of the two laser beams are not equal, the modulation amplitude is reduced [86]. This is expressed in accordance with Eq. (4.2) as

$$P_{\mathrm{het}}\left(t\right) = P_1 + P_2 + 2\sqrt{mP_1P_2}\cos\left(\omega_{\mathrm{THz}}t\right), \tag{4.3}$$

where $m = \vec{E}_1 \circ \vec{E}_2 / |E_1| \cdot |E_2|$ is the mixing efficiency [25]. Semiconductor devices with bandgap energy $E_{\mathrm{G}} = \hbar\omega_{\mathrm{THz}}$ absorb the heterodyned signal and generate electron-hole pairs. The generated photocarriers are effectively separated through a bias or a built-in accelerating field and the resulting photocurrent contains an AC component with the angular frequency of ω_{THz}. An appropriately designed antenna attached to the device converts the AC into free-space THz emission as shown in Fig. 4.1. Such a device is termed as a photomixer or antenna-based emitter (AE).

4.1.1 THz Signal Generation

The AEs radiating the THz signal can be classified into photoconductors and p-i-n-based emitters [86]. In the case of photoconductors, the generated photocarriers have recombination lifetime of τ_{rec} in the sub-ps range. An external bias is applied to the metal contacts of a photoconductor resulting the respective drifts of the electrons and holes towards the contacts. The resulting photocurrent is parallel to the surface, and such devices will be denoted as lateral photoconductors. In contrast to lateral photoconductors, the photogenerated carriers in the intrinsic layer of the p-i-n-based emitters propagate towards the respective n- and p-doped layers due to a built-in field perpendicular to the surface.

We will, first, start with deriving few important equations with an exemplary photoconductor which is shown in Fig. 4.1. The beat signal is focused between the area of the electrodes with width, w_{AE} and length, l_{AE} in the x- and y-directions, respectively and photocarriers are generated within a thickness of d_{AE}. For simplicity, we assume on the one hand that electrons and holes have constant mobilities of μ_{e} and μ_{h}, resrectively where $\mu_{\mathrm{e}} \gg \mu_{\mathrm{h}}$ [87]. On the other hand, electrons drift with a saturation velocity towards the contacts in the presence of a DC bias voltage, V_{bias} applied between the metallic bias pads. Under these assumptions, the total photocurrent density, J_{ph} is

$$J_{\mathrm{ph}}\left(t\right) = \sigma\left(t\right) E_{\mathrm{bias}}, \tag{4.4}$$

where E_{bias} is the electric field of the applied bias and the conductivity, σ is

$$\sigma\left(t\right) \approx e N_{\mathrm{c}}\left(t\right) \mu_{\mathrm{e}}, \tag{4.5}$$

with e and $N_{\mathrm{c}}\left(t\right)$ as the elementary electric charge and instantaneous number of pairs of photocarrier in an uniform cross section of $A_{\mathrm{AE}} = w_{\mathrm{AE}} d_{\mathrm{AE}}$, respectively. Thus, the photocurrent, I_{ph} is obtained as

$$I_{\mathrm{ph}}\left(t\right) \approx e N_{\mathrm{c}}\left(t\right) v_{\mathrm{dr}} A_{\mathrm{AE}}, \tag{4.6}$$

where $v_{\mathrm{dr}} = \mu_{\mathrm{e}} E_{\mathrm{bias}}$ is the drift velocity of electrons. The excited electrons N_{c} follow the rate equation given by

$$\frac{dN_{\mathrm{c}}\left(t\right)}{dt} = \frac{\eta_{\mathrm{e}}}{h\nu} \frac{P_{\mathrm{het}}\left(t\right)}{V_{\mathrm{AE}}} - \frac{N_{\mathrm{c}}\left(t\right)}{\tau_{\mathrm{rec}}}, \tag{4.7}$$

where η_{e} and V_{AE} are the external quantum efficiency and volume of the photomixer, and τ_{rec} is the mean recombination lifetime of the electrons. Inserting Eq. (4.7) in

Eq. (4.2) yields,

$$\frac{dN_{\mathrm{c}}\left(t\right)}{dt} = \frac{\eta_{\mathrm{e}}}{h\nu V_{\mathrm{AE}}}\left[2P_0\left[1+\cos\left(\omega_{\mathrm{THz}}t\right)\right]\right] - \frac{N_{\mathrm{c}}\left(t\right)}{\tau_{\mathrm{rec}}}. \tag{4.8}$$

The solution to this differential equation is given by

$$N_{\mathrm{c}}\left(t\right) = \frac{2\eta_{\mathrm{e}}\tau_{\mathrm{rec}}P_0}{h\nu V_{\mathrm{AE}}}\left[1+\frac{1}{\sqrt{1+\left(\omega_{\mathrm{THz}}\tau_{\mathrm{rec}}\right)^2}}\sin\left(\omega_{\mathrm{THz}}t+\varphi\right)\right], \tag{4.9}$$

with $\varphi = \arctan\left(1/\omega_{\mathrm{THz}}\tau_{\mathrm{rec}}\right)$. Inserting Eq. (4.9) in Eq. (4.6), the photocurrent is obtained as,

$$\begin{aligned} I_{\mathrm{ph}}\left(t\right) &\approx \frac{2eP_0\eta_{\mathrm{e}}}{h\nu}\frac{\tau_{\mathrm{rec}}v_{\mathrm{dr}}A_{\mathrm{AE}}}{V_{\mathrm{AE}}}\left[1+\frac{1}{\sqrt{1+\left(\omega_{\mathrm{THz}}\tau_{\mathrm{rec}}\right)^2}}\sin\left(\omega_{\mathrm{THz}}t+\varphi\right)\right] \\ &\approx \frac{2eP_0\eta_{\mathrm{e}}}{h\nu}\frac{\tau_{\mathrm{rec}}}{\tau_{\mathrm{tr}}}\left[1+\frac{1}{\sqrt{1+\left(\omega_{\mathrm{THz}}\tau_{\mathrm{rec}}\right)^2}}\sin\left(\omega_{\mathrm{THz}}t+\varphi\right)\right], \end{aligned} \tag{4.10}$$

with transit time of the electrons of $\tau_{\mathrm{tr}} = l_{\mathrm{AE}}/v_{\mathrm{dr}}$. By defining the ideal DC and AC amplitude of,

$$I_0^{\mathrm{id}} = \frac{2eP_0}{h\nu}, \tag{4.11}$$

Eq. (4.10) reduces to

$$I_{\mathrm{ph}}\left(t\right) \approx I_0^{\mathrm{id}}\eta_{\mathrm{e}}\left(\frac{\tau_{\mathrm{rec}}}{\tau_{\mathrm{tr}}}\right)\left[1+\frac{1}{\sqrt{1+\left(\omega_{\mathrm{THz}}\tau_{\mathrm{rec}}\right)^2}}\sin\left(\omega_{\mathrm{THz}}t+\varphi\right)\right]. \tag{4.12}$$

As understood from Eq. (4.12), both the DC and AC amplitudes of the photocurrent are reduced by the value of η_{e}. By using an AR coating and sufficiently thick absorbing layer, η_{e} can approach one. The reduction factor of the form $\left(\tau_{\mathrm{rec}}/\tau_{\mathrm{tr}}\right)\cdot[1+\left(\omega_{\mathrm{THz}}\tau_{\mathrm{rec}}\right)^2]^{-1}$ arises from carrier transport-related mechanisms. The DC amplitude of the photocurrent is strongly reduced by the first term of this factor known as photoconductive gain $g_{\mathrm{AE}} = \left(\tau_{\mathrm{rec}}/\tau_{\mathrm{tr}}\right) \ll 1$ [88]. In accordance with g_{AE}, the second factor introduces a roll-off for the AC component with increasing frequency. The associated 3 dB frequency, ω_{rec} is given by

$$\omega_{\mathrm{rec}} = \frac{1}{\tau_{\mathrm{rec}}}. \tag{4.13}$$

4.1.2 Emitted THz Power

The AC component of the photocurrent, as from Eq. (4.12),

$$I_{\mathrm{ph}}^{\mathrm{AC}}(t) \approx I_0^{\mathrm{id}} \eta_{\mathrm{e}} \left(\frac{\tau_{\mathrm{rec}}}{\tau_{\mathrm{tr}}}\right) \left[\frac{1}{\sqrt{1+\left(\omega_{\mathrm{THz}} \tau_{\mathrm{rec}}\right)^2}} \sin\left(\omega_{\mathrm{THz}} t + \varphi\right)\right], \tag{4.14}$$

is fed to an antenna which converts the AC component into THz radiation as,

$$P_{\mathrm{THz}} = \frac{1}{2} \mid I_{\mathrm{ph}}^{\mathrm{AC}} \mid^2 \Re\left(Z_{\mathrm{load}}\right), \tag{4.15}$$

where Z_{load} is the impedance of the external circuit. Z_{load} comprises of the radiation resistance, R_{A} of the antenna, device photoconductance, G_{ph} and device capacitance, C. Under the illumination, Z_{load} is

$$Z_{\mathrm{load}} = \left(\frac{1}{R_{\mathrm{A}}} + G_{\mathrm{ph}} + i\omega C\right)^{-1}. \tag{4.16}$$

For a real photomixer, the relation of $R_{\mathrm{A}} \ll 1/G_{\mathrm{ph}}$ gives the expression of,

$$\Re\left(Z_{\mathrm{load}}\right) = \frac{R_{\mathrm{A}}}{1+\left(\omega_{\mathrm{THz}} C R_{\mathrm{A}}\right)^2}. \tag{4.17}$$

Inserting Eq. (4.17) in Eq. (4.15), the emitted power is given by

$$P_{\mathrm{THz}} = \frac{1}{2}\left(I_0^{\mathrm{id}}\right)^2 \eta_{\mathrm{e}}^2 \left(\frac{\tau_{\mathrm{rec}}}{\tau_{\mathrm{tr}}}\right)^2 \cdot \frac{1}{1+\left(\omega_{\mathrm{THz}} \tau_{\mathrm{rec}}\right)^2} \cdot \frac{R_{\mathrm{A}}}{1+\left(\omega_{\mathrm{THz}} C R_{\mathrm{A}}\right)^2}. \tag{4.18}$$

For the photoconductors, the power reduction of

$$P_{\mathrm{THz}} \sim \left(\frac{\tau_{\mathrm{rec}}}{\tau_{\mathrm{tr}}}\right)^2 = g_{\mathrm{AE}}^2, \tag{4.19}$$

is obtained for the low-frequency limit. For the high-frequency of operation, the emitted power of

$$P_{\mathrm{THz}} \sim \frac{1}{1+\left(\omega_{\mathrm{THz}} \tau_{\mathrm{rec}}\right)^2} \cdot \frac{1}{1+\left(\omega_{\mathrm{THz}} C R_{\mathrm{A}}\right)^2} \sim \omega_{\mathrm{THz}}^{-4} \tag{4.20}$$

is independent of the recombination lifetime, but is influenced additionally by the RC roll-off factor with the associated 3 dB frequency of,

$$\omega_{\mathrm{RC}} = \frac{1}{\tau_{\mathrm{RC}}}, \qquad \text{with} \qquad \tau_{\mathrm{RC}} = R_{\mathrm{A}}C. \tag{4.21}$$

In the high-frequency limit, the emitted THz power is, therefore, reduced within a range from 20 dB–40 dB.

For p-i-n-diode emitters, recombination plays insignificant role and practically all the photogenerated carriers reach at the contacts, thus, $g_{\mathrm{AE}} = 1$ [86]. However, the finite transit time through the intrinsic layer still introduces a roll-off [86] and Eq. (4.18) is modified according to

$$P_{\mathrm{THz}} = \frac{1}{2}\left(I_0^{\mathrm{id}}\right)^2 \eta_{\mathrm{e}}^2 \cdot \frac{1}{1 + (\nu_{\mathrm{THz}}/\nu_{\mathrm{tr}})^2} \cdot \frac{R_{\mathrm{A}}}{1 + (\nu_{\mathrm{THz}}/\nu_{\mathrm{RC}})^2}. \tag{4.22}$$

4.2 Tunable THz Photomixing with Direct Power Detection

The MEMS-VCSEL employed for this experiment [36] is biased through electrical contact needles for both the cavity and membrane. The bias current for the cavity and substrate temperature are 26 mA and 22 °C, respectively. For THz signal generation, a longitudinal mode-hop-free tuning in the range between 1530 nm–1565 nm is desired to be able to implement an EDFA to boost the laser signal. The MEMS-VCSEL has a FSR of 80 nm over which a mode-hop-free, CW tuning of 70 nm(8.8 THz) is accomplished. SMSR of > 55 dB is maintained over the entire tuning range.

Figure 4.2 shows this MEMS-VCSEL-driven experimental photomixing setup with direct power detection. The first variant of this setup uses a non-tunable, packaged VCSEL as the second laser for optical heterodyning. Emitted light of the on-wafer MEMS-VCSEL is guided to a SMF via an AR coated lens supporting the fundamental Gaussian mode of the laser. Mechanical robustness of the coupling lens avoids externally influenced power variation of the received power. The maximum power coupled to the SMF at this bias current is 0.66 mW. Moreover, the broadband AR coating greatly suppresses back-reflections. First, 1 % power of the on-wafer MEMS-VCSEL is tapped out for the wavelength control circuit. The setup incorporates separate amplifiers for each VCSEL to reach sufficient power for THz photomixing.

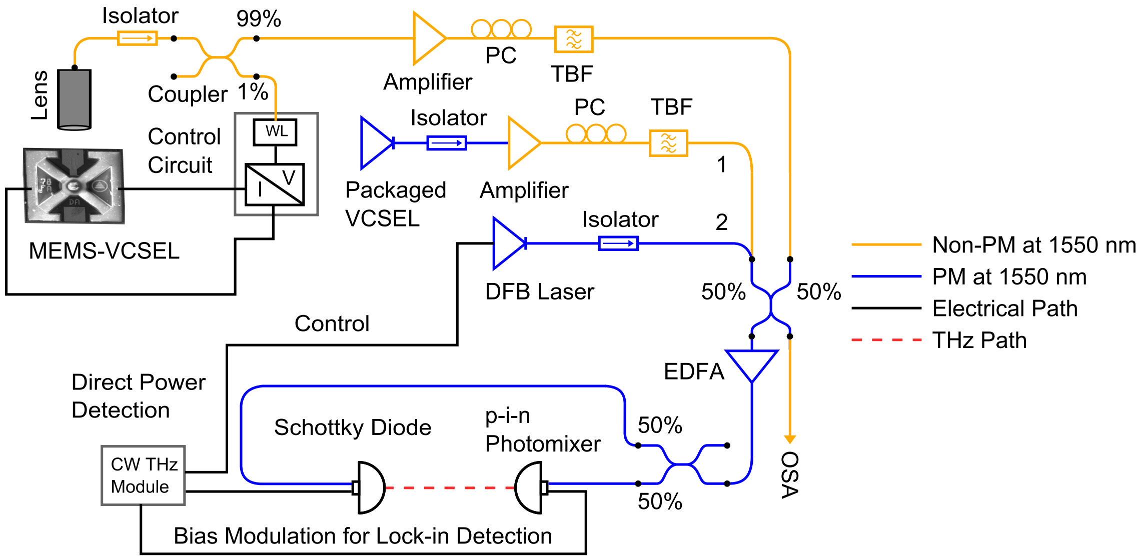

Figure 4.2: Schematic for the THz photomixing setup with direct power detection of a Schottky diode. The first variant of the setup is all VCSELs-based photomixing system. In the second variant of this setup, a DFB laser replaces the non-tunable VCSEL.

A non-PM EDFA[1] and a semiconductor optical amplifier (SOA)[2] are used after the MEMS-VCSEL and non-tunable VCSEL, respectively. Tunable band-pass filter (TBF) is used after each amplifier to remove the amplified spontaneous emission (ASE) noise to get a clean THz signal after photomixing. The TBF used after the non-tunable VCSEL is positioned at its emission wavelength. An appropriate low-cost fixed-wavelength filter can be used alternatively. The 3 dB bandwidths of both of the filters are set to 200 pm (25 GHz) during the experiment. As the first-stage amplifiers and TBFs are not PM, two polarization controllers (PCs) are implemented prior to the PM photomixing setup. After filtering, the outputs of the VCSELs are combined by a 50/50 optical coupler and further amplified by a PM EDFA[3] to reach an output power of 22 mW each. Finally, the output signal pumps a p-i-n photomixer[4] for THz signal generation. The p-i-n photomixer source is bias-modulated by a commercial THz module[5] for the later lock-in detection. On the detection side, a zero-bias Schottky diode (direct power detector) is used. The THz module performs a lock-in

---

[1] ATx Telecom Systems, 1.5-AMP

[2] THORLABS, SOA 1117

[3] PriTel, PMFA-35-S-IO

[4] WIN-PD from Fraunhofer-Institut für Nachrichtentechnik/TOPTICA Photonics

[5] TOPTICA Photonics

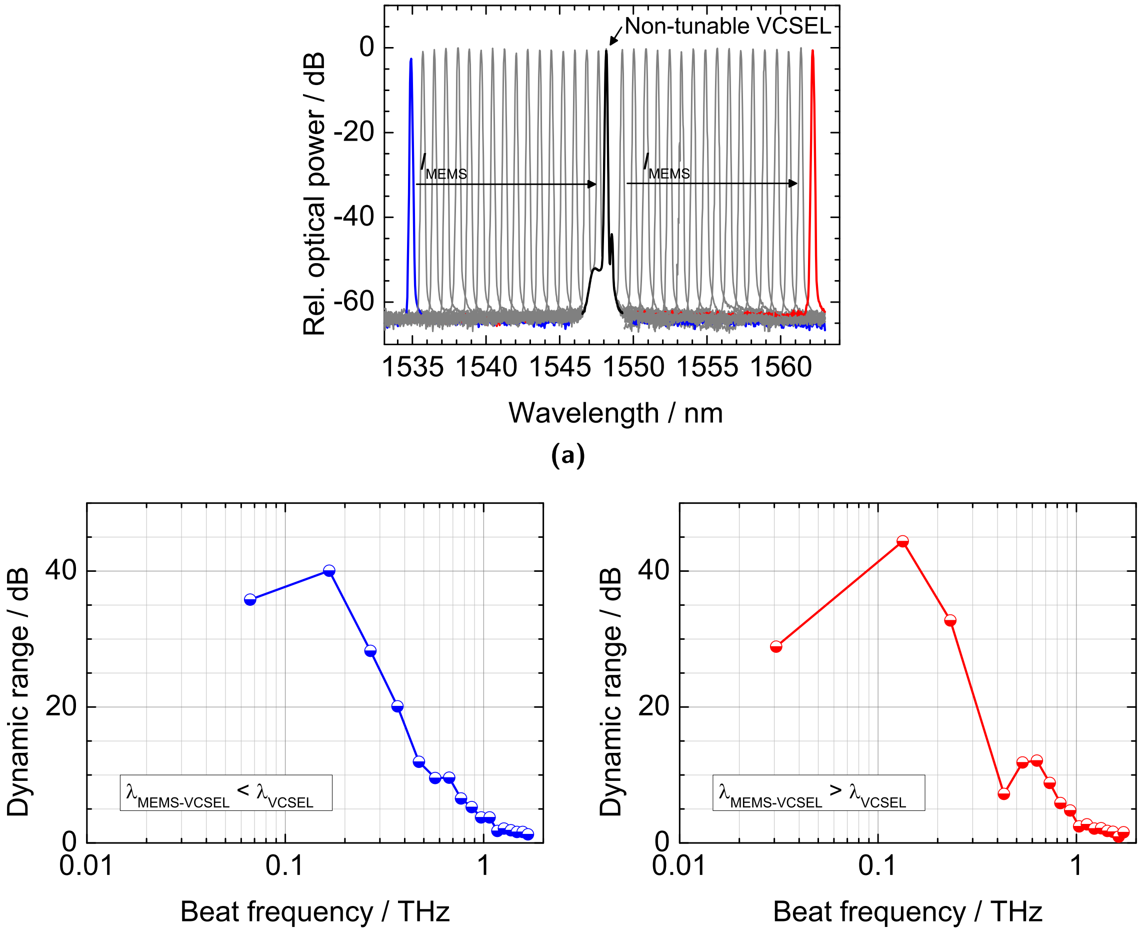

(a)

(b) **(c)**

Figure 4.3: (a) 100 GHz-spaced tuning of the MEMS-VCSEL by the wavelength control circuit from 1534.92 nm–1562.17 nm with respect to the non-tunable VCSEL. Corresponding power detection with the Schottky diode: (b) THz signal from 1.67 THz–0.066 THz for $\lambda_{\text{MEMS-VCSEL}} < \lambda_{\text{VCSEL}}$ and (c) from 0.03 THz–1.73 THz for $\lambda_{\text{MEMS-VCSEL}} > \lambda_{\text{VCSEL}}$.

detection with an integration time, $\tau_{\text{LIA}} = 600$ ms of the received THz photocurrent. The module can follow a frequency tuning up to 1.75 THz which is limited by the dynamic range of the photomixer and Schottky-diode used in the setup.

To demonstrate the large tuning range of this MEMS-VCSEL for the direct detection setup, 28 nm tuning from 1534.92 nm–1562.17 nm is illustrated in Fig. 4.3a [36] covering the whole amplification range of the employed EDFAs. The wavelength of the non-tunable VCSEL is fixed at $\lambda_{\text{VCSEL}} = 1548.18$ nm. At first, the MEMS-VCSEL is tuned and locked to 1534.92 nm. The corresponding optical beating with the non-tunable VCSEL generates a bandwidth of 1.67 THz. The following tuning with subsequent stabilization performed by the wavelength control circuit scans the bandwidth with a resolution of 100 GHz. The dynamic range (DR) for the direct power detection is calculated according to

$$\mathrm{DR}_{\mathrm{DPD}} = 10 \log \left(P_{\mathrm{THz}} / P_{\mathrm{noise}} \right), \tag{4.23}$$

where the noise floor (NF) signal, P_{noise} is of 0.08 nA and is measured by blocking the THz path.

For $\lambda_{\text{MEMS-VCSEL}} < \lambda_{\text{VCSEL}}$, the detected THz signal from 1.67 THz–0.066 THz is thus plotted in Fig. 4.3b [36]. The roll-off of the detected THz signal is due to the roll-off of the p-i-n emitter $\left(\sim \nu^{-2} - \nu^{-4}\right)$ [86] and roll-off of the Schottky diode $\left(\sim \nu^{-2}\right)$ [89] that are used for the detection. The highest DR of $\approx$ 44.4 dB is achieved at 1.33 THz while that remains in excess of 2.4 dB above 1 THz. Similarly for $\lambda_{\text{MEMS-VCSEL}} > \lambda_{\text{VCSEL}}$, Fig. 4.3c shows the detected THz signal from 0.03 THz–1.73 THz [36]. Thus, the measurement demonstrates a total bandwidth of 3.4 THz (1.67 THz + 1.73 THz). In terms of further tuning of the MEMS-VCSEL, there is no fundamental limit. Thus the further tuning capability of this setup is solely limited by the dynamic range of the THz emitter/receiver system.

For the second variant of this experiment, a DFB laser [6] with $\lambda_{\mathrm{DFB}} = 1548.53$ nm replaces the non-tunable VCSEL, subsequent amplifier, and TBF as it has sufficient output power. The wavelength tuning of the MEMS-VCSEL as shown in Fig. 4.3a, as well as the total power pumping the p-i-n emitter, are kept the same for this experiment. Figure 4.4 shows the detected THz signal from 1.72 THz–0.12 THz for $\lambda_{\text{MEMS-VCSEL}} < \lambda_{\mathrm{DFB}}$ and from 0.09 THz–1.68 THz for $\lambda_{\text{MEMS-VCSEL}} > \lambda_{\mathrm{DFB}}$.

4.3 Tunable THz Photomixing with Homodyne Detection

MEMS-VCSELs-based tunable THz photomixing, so far, has been shown for the direct power detection where the tuning resolution is 100 GHz controlled by the wavelength control circuit. Tuning resolution of 25 GHz/50 GHz can be achieved by using a commercially available 25 GHz/50 GHz-FSR WL. As outlined in Sec. 3.4, an additional functional block of the wavelength control circuit can tune and lock

---

[6] Sacher Lasertechnik, DFB-1550-040

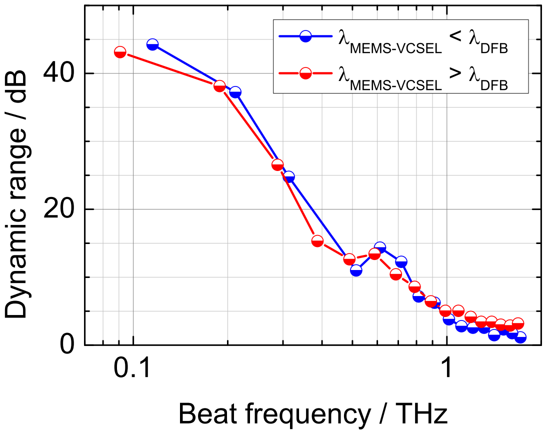

Figure 4.4: THz photomixing setup driven by the MEMS-VCSEL and a DFB laser with direct power detection of the Schottky diode: THz signal from 1.72 THz–0.12 THz for $\lambda_{\text{MEMS-VCSEL}} < \lambda_{\text{DFB}}$ and from 0.09 THz–1.68 THz for $\lambda_{\text{MEMS-VCSEL}} > \lambda_{\text{DFB}}$.

MEMS-VCSELs with a frequency resolution of 1 GHz. Scanning of several THz with this resolution should be directed in an entirely automated fashion which needs complex programming. We aim to accomplish this with packaged MEMS-VCSELs rather than those being on-wafer. Since the purpose of this work is to show the compatibility of MEMS-VCSELs towards THz photomixing, an alternative way for the broadband THz signal generation with fine-tuning will be presented. This is fulfilled by driving the photomixer with a pair of a MEMS-VCSEL and a DFB laser in the homodyne field detection mode with a photoconductive mixer (photoconductor).

The MEMS-VCSEL used for this experiment is biased with RF ground-signal (GS) probes which greatly eliminates RF noise pickups. Threshold current and threshold voltage are 5.4 mA, and 1.03 V. Efficiencies and other static characteristics of this particular MEMS-VCSEL are prsented in Apps. B.1 and B.2. Figure 4.5 shows the electrothermal actuation of this MEMS-VCSEL with a mode-hop-free tuning from 1525 nm ($I_{\text{MEMS}} = 0$ mA) to 1589 nm ($I_{\text{MEMS}} = 37.6$ mA) with $I_b = 20$ mA and $T_s = 22\,°\text{C}$. This yields a tuning range of 64 nm (7.92 THz), covering the whole range of an EDFA. It is worth mentioning that the CW tuning of 64 nm is less than the FSR of 92 nm which is seen in the inset of Fig. 4.5. The reason that this MEMS-VCSEL does not lase over its entire FSR is explained in App. B.3. Figure 4.5 also shows the CW power and voltage profile of this MEMS-VCSEL. The inset also shows the high spectral purity with the highest SMSR of 58 dB around 1552 nm while SMSR > 50 dB is maintained over the entire tuning range. The electro-optical

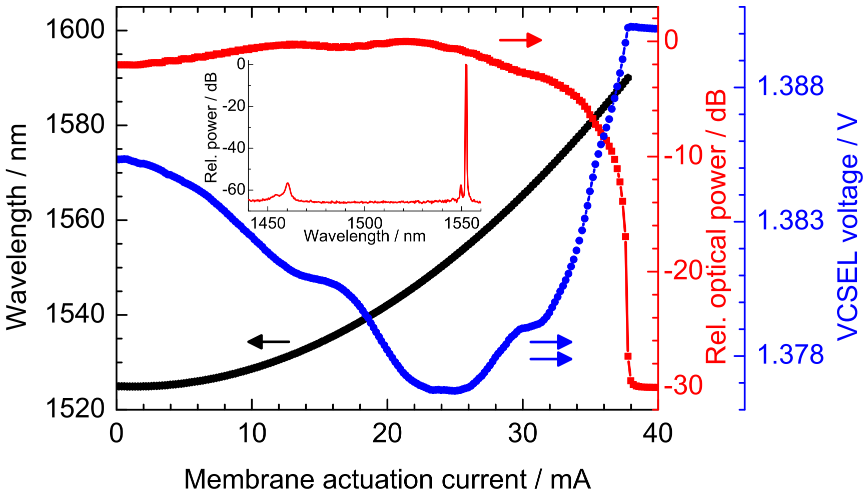

Figure 4.5: Mode-hop-free CW power, operating voltage and peak emission wavelength as functions of I_{MEMS} of the MEMS-VCSEL employed for homodyne photomixing setup. Inset is the emission characteristics

measurement in Fig. 3.16b shows the resonance frequencies of this MEMS-VCSEL. Using $\nu_{\text{res},1} = 214\,\text{kHz}$, $\Delta\nu_{3\text{-dB}} = 70\,\text{kHz}$, Eqs. (3.14) and (3.16) yield the spring constant and quality factor of $k_{\text{m}} = 614.71\,\text{N/m}$ and $Q = 3.06$, respectively.

Figure 4.6 schematically shows the photomixing setup for the homodyne measurement technique. This setup utilizes the polarization stability of the employed MEMS-VCSEL with a PSR of $> 20\,\text{dB}$ over its entire tuning range. This leads to implement all PM devices and components around 1550 nm. The optical power is coupled to a PM fiber (PMF) through an aspheric lens, aligned to the slow axis of the PMF. The coupled power in the PMF is 1.5 mW. 1 % of the output power is tapped out for the wavelength control circuit. The remaining power is guided to the 95 %-port of a 95/5 PM-coupler where the 5 %-port is fed by the DFB laser with a power of about 40 mW. The unequal coupling from the two lasers at the input balances the power levels at the output of the PM coupler. A gain-flattened PM EDFA[7] amplifies the combined power to $\approx 44\,\text{mW}$. The polarization-matched, equal-amplitude power from the two lasers feature a (tunable) difference frequency in the THz range which drives the p-i-n photomixer. An antenna radiates the THz emission into the free space. The THz detection is accomplished by employing the photoconductor for the homodyne detection with τ_{LIA} between 30 ms and 300 ms. The frequency bandwidth of this setup is $\approx 2.75\,\text{THz}$ limited by the dynamic range of detector-source pair at the given combined power. As compared to the previously

---

[7] PriTel, PMFA-20-IO

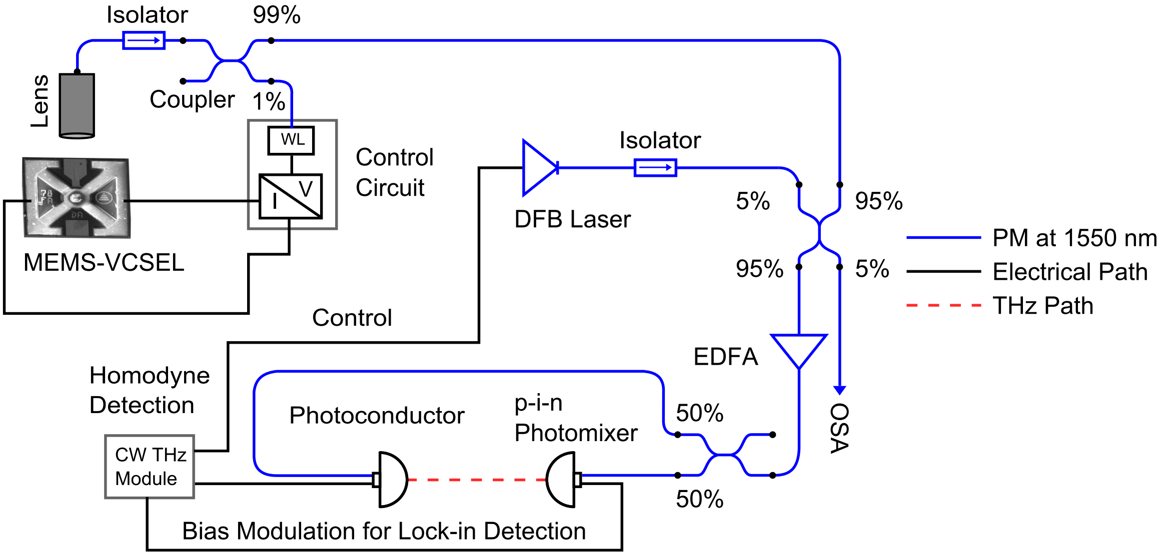

Figure 4.6: Schematic of the PM photomixing setup. The CW photomixer is driven by the on-wafer, polarization stable MEMS-VCSEL, and a DFB laser in the homodyne field detection mode with a photoconductor.

reported non-PM setup with the separate amplifier for each laser source [36], this setup is drastically simplified using only PM components and only one PM EDFA.

To demonstrate the continuous tunability and frequency coverage for the homodyne THz setup, the MEMS-VCSEL is tuned and locked by the wavelength control circuit to a particular wavelength between 1533.41 nm and 1570.41 nm covering the whole amplification range of the PM EDFA. At first, the MEMS-VCSEL is locked to 1533.41 nm. The corresponding optical beating with the longest DFB laser wavelength of 1558.57 nm generates a bandwidth of 3148.51 GHz. Within this bandwidth, the DFB laser is thermally tuned over its complete tuning range from 1558.57 nm–1554.16 nm ($\approx$ 540 GHz) in 100 MHz steps. This method allows for a frequency resolution defined by the step size of the DFB laser which can be as small as 1 MHz–2 MHz if required. After tuning the DFB laser by $\approx$ 540 GHz, the MEMS-VCSEL is coarsely tuned to the fourth or fifth next locking point, i.e., by 400 GHz or 500 GHz as listed in Tab. 4.1. As the wavelength step-size of the VCSEL is smaller than the bandwidth of the DFB laser, this technique ensures the overlap of the individual DFB sweeps to get a continuous spectrum without interruptions. In this procedure, the full THz bandwidth of the photomixing setup can be covered. To demonstrate the large tunability of this system, we continue the stepping up to 1570.41 nm with the difference frequency of 1988.14 GHz with respect to the shortest DFB laser wavelength of 1554.16 nm.

Table 4.1: Procedure of broadband THz photomixing for homodyne detection.

Number	$\lambda_{\text{MEMS-VCSEL}}$ / nm	Scanned Bandwidth / GHz
1	1533.41	3148.51–2604.80
2	1536.50	2755.83–2213.83
3	1539.69	2353.62–1810.62
4	1542.86	1952.99–1414.66
5	1546.05	1553.76–1012.30
6	1550.04	1054.62–512.83
7	1554.09	552.40–9.36
8	1558.15	51.00–0 and 0–491.01
9	1562.20	446.60–988.36
10	1566.31	948.06–1490.12
11	1570.41	1448.04–1988.14

The detected THz photocurrent is given by [90]

$$I_{\text{ph}} \propto E_{\text{THz}} \cos\left(\Delta\varphi\right) = E_{\text{THz}} \cos\left(2\pi \Delta L \nu_{\text{THz}}/c\right), \tag{4.24}$$

with the THz electric field amplitude, E_{THz}, phase difference, $\Delta\varphi$ between the THz wave and the beat signal of the lasers, THz frequency, ν_{THz} and optical path difference of the photomixing setup, ΔL which is given by

$$\Delta L = \left(L_{\text{T}} + L_{\text{THz}}\right) - L_{\text{R}}, \tag{4.25}$$

where L_{T}, L_{R} represent optical path up to the transmitter and receiver in the fibers with refractive index, n, respectively, and L_{THz} is the THz path between the transmitter and receiver. For any given frequency ν_{THz}, the information about the phase and amplitude of the detected THz signal can be obtained by varying $\Delta\varphi$, i.e., by scanning the ν_{THz} where I_{ph} oscillates with the period set by a predetermined ΔL. For our case, this is set by the unequal length of the optical fibers connecting the transmitter and receiver (from output ports of the final-stage coupler) so that $L_{\text{T}} \neq L_{\text{R}}$. CW scanning for a frequency range of 520 GHz–600 GHz is shown in Fig. 4.7a. The period of oscillations of the interference pattern is calculated to be $\approx$ 5 GHz (peak-to-peak frequency between two maxima), which corresponds to

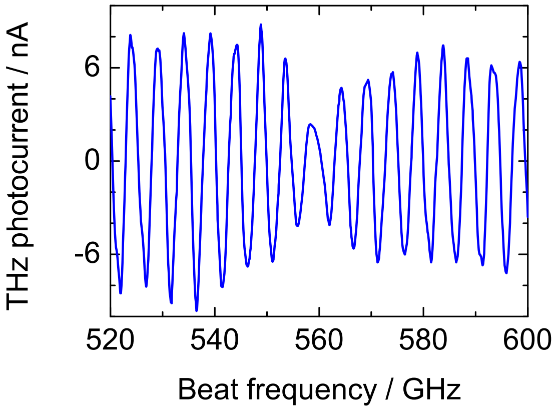

(a)

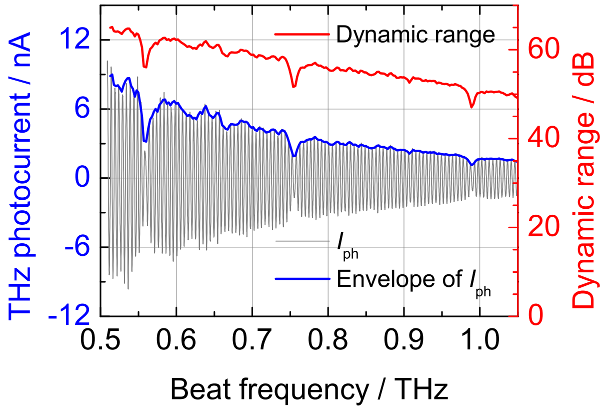

(b)

Figure 4.7: (a) Detected photocurrent for a portion of the frequency-window six as in Tab. 4.1. Both the amplitude and phase information can be retrieved. The period of oscillations of the interference pattern is about 5 GHz corresponding to $\Delta L \approx 0.06\,\mathrm{m}$. (b) The envelope of the detected photocurrent shows three water absorption lines at 557, 752 and 988 GHz which can be best understood by plotting the $\mathrm{DR}_{\mathrm{HMD}}$ with $I_{\mathrm{noise}} = 5\,\mathrm{pA}$ ($\tau_{\mathrm{LIA}} = 300\,\mathrm{ms}$).

$\Delta L \approx 0.06\,\mathrm{m}$. By increasing the ΔL, the scanning resolution can be increased. Figure 4.7b shows the frequency scanning of one of the frequency windows (row six in Tab. 4.1) where I_{ph} is given by the envelope of the detected phase showing three water absorption lines at 557, 752 and 988 GHz. These can be best understood when the DR for the homodyne detection

$$\mathrm{DR}_{\mathrm{HMD}} = 20 \log \left(I_{\mathrm{ph}} / I_{\mathrm{noise}} \right) , \tag{4.26}$$

is plotted as a function of the beat frequency where I_{noise} is the noise current measured by blocking the THz path and I_{ph} is the oscillation amplitude measured without any sample placed along the THz path.

By using Eq.(4.26) with $I_{\text{noise}} = 5\,\text{pA}$ ($\tau_{\text{LIA}} = 300\,\text{ms}$), Fig. 4.8a displays a scan for $\lambda_{\text{MEMS-VCSEL}} < \lambda_{\text{DFB}}$ where the individual DFB sweeps are highlighted by alternate color sequences. The roll-off of the detected THz signal is due to the roll-off of the p-i-n emitter $\left(\sim \nu^{-2} - \nu^{-4}\right)$ and roll-off of the photoconductor $\left(\sim \nu^{-2} - \nu^{-4}\right)$ [86]. The swept THz bandwidth from 3.14 THz to DC is solely limited by the noise floor of the photomixing system to 2.75 THz. To assure fast data acquisition, most data are recorded with $\tau_{\text{LIA}} = 30\,\text{ms}$. Only for the three traces (green, black and green traces) above 1.95 THz as shown in Fig. 4.8a, $\tau_{\text{LIA}} = 300\,\text{ms}$ is used to reduce the noise floor and extend the THz bandwidth. Since the setup is operated under the ambient air, several water lines are clearly visible at 557, 621, 752, 988, 1097, 1113, 1163, 1208, 1229, 1278, 1322, 1411, 1602, 1661, 1669, 1717, 1762 and 1795/1797 GHz [90, 91]. A dynamic range of $\approx$ 87.5 dB is obtained at 0.1 THz while that drops to $\approx$ 50.5 dB at 1 THz. These values are 10 dB smaller with respect to the noise floor for $\tau_{\text{LIA}} = 30\,\text{ms}$ as also shown in Fig. 4.8a. Similarly, Fig. 4.8b shows a scanning from DC to 1.99 THz for $\lambda_{\text{MEMS-VCSEL}} > \lambda_{\text{DFB}}$. In this case, THz bandwidth is limited by the bandwidth of the PM EDFA to a maximum difference frequency of 1.99 THz.

The measurement demonstrates a total bandwidth of 4.74 THz (2.75 THz + 1.99 THz). This is 1.49 THz larger than demonstrated with the non-PM photomixing setup as reported by our group in Ref. [36]. Improved photomixers with an extended bandwidth would allow for the sweep up to a THz bandwidth of 4.74 THz using the presented optical system. In that case, a DFB laser has to be chosen featuring its longest wavelength at the edge of the EDFA gain region.

4.4 Summary and Outlook

The performance of on-wafer tunable MEMS-VCSELs is investigated in details for application in an tunable THz photomixing system with unprecedented bandwidth. A purely VCSELs-based system for driving a CW photomixer is demonstrated in which the tunable MEMS-VCSEL is stepped through 100 GHz spaced lock points with respect to a non-tunable VCSEL covering a frequency span of 3.4 THz in direct detection mode. We setup a second variant of this system where the non-tunable VCSEL is replaced by a DFB laser, and the corresponding photomixing generates a THz signal with a bandwidth of 3.4 THz with the same scanning resolution.

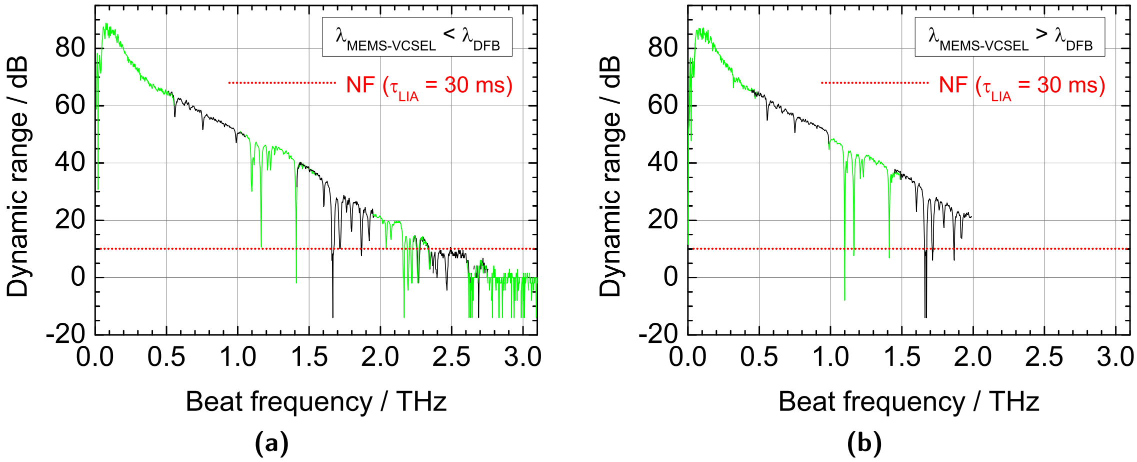

(a) **(b)**

Figure 4.8: (a) Homodyne detection up to 2.75 THz for $\lambda_{\text{MEMS-VCSEL}} < \lambda_{\text{DFB}}$. The individual DFB sweeps are indicated in black and green, respectively. The dynamic range is indicated with respect to the NF for $\tau_{\text{LIA}} = 300\,\text{ms}$ whereas this is 10 dB smaller with respect to the NF for $\tau_{\text{LIA}} = 30\,\text{ms}$. Several water lines are visible. (b) Homodyne detection up to 1.99 THz for $\lambda_{\text{MEMS-VCSEL}} > \lambda_{\text{DFB}}$.

For achieving higher scanning resolution, we set up a second system where the photomixer is driven by another MEMS-VCSEL and a DFB laser in homodyne field detection mode with a photoconductor. This setup utilizes the polarization stability of the employed MEMS-VCSEL with a PSR of $> 20\,\text{dB}$ over the entire tuning range. This leads to implement all PM devices and components at 1550 nm. For a broadband THz signal generation, the DFB laser is scanned in 100 MHz steps over its tuning range in each frequency window which is selected by an appropriate choice of the lock point of the MEMS-VCSEL. This setup covers a frequency span of 4.74 THz and solely limited by the dynamic range of the setup and the bandwidth of the used EDFA, not by the MEMS-VCSEL which offers an electrothermal tuning of 64 nm corresponding to a maximum bandwidth of 7.92 THz. The polarization stable MEMS-VCSEL provides the maximum fiber coupled power of 1.5 mW, and features a linewidth below 50 MHz over the entire tuning range. The MEMS-VCSEL is therefore well suited for THz photomixing systems. Regarding the wavelength stability, temperature, acoustic, electronic and mechanical noises cause long-term frequency fluctuations of the on-wafer MEMS-VCSEL of $331.91 \pm 9.34\,\text{MHz}$. Packaging and isolation from the temperature, acoustic and electronic noises could improve the stability. Further fluctuations can be canceled using a fast wavelength control circuit using electrostatic stabilization with a locking bandwidth significantly above the mechanical resonance frequencies of the membrane. Electrostatically tunable

Table 4.2: Measured characteristics of the MEMS-VCSEL with $I_b = 20\,\mathrm{mA}$, $T_s = 22\,^\circ\mathrm{C}$ towards tunable PM photomixing.

Type	Parameters	Measured
Mechanical	Membrane Spring Constant, k_m	$614.71\,\mathrm{N/m}$
	Fundamental Resonance Frequency, $\nu_{\mathrm{res},1}$	$214\,\mathrm{kHz}$
	Quality Factor, Q	3.06
Electro-Optical	Maximum Coupled Power, P_{opt}	$1.5\,\mathrm{mW}$
	Tuning Range	$64\,\mathrm{nm}$ ($7.92\,\mathrm{THz}$)
	SMSR over the Tuning Range	$> 20\,\mathrm{dB}$
	PSR over the Tuning Range	$> 20\,\mathrm{dB}$
	Emission Linewidth, $\Delta\nu_{\mathrm{LW}}$	$< 50\,\mathrm{MHz}$
	Effective Linewidth over the Tuning Range	$< 350\,\mathrm{MHz}$
Tunable THz Photomixing	Homodyne Detection Bandwidth	$4.74\,\mathrm{THz}$

MEMS-VCSELs, however, will be part of the future work. The examined parameters of this MEMS-VCSEL with the experimental PM photomixing result are tabulated in Tab. 4.2. With further improvement of the THz emitter and detector components, the tuning range can be further extended.

5 Silver Nanowires-Based Lateral Photoconductors

The physical and chemical properties of metallic nanowires have attracted much attentions in the quest for future nanodevices and are expected to play a vital role in nanoelectronics, optoelectronics, sensorics, and numerous other fields [92, 93]. In context with the CW tunable photoconductors, the THz power roll-off due to the device capacitance is found detrimental for the emission bandwidth. For instance, a conventional low-temperature-grown (LTG) GaAs photoconductor with 6-finger interdigitated electrodes has a device capacitance of $\sim 3\,\mathrm{fF}$ [37], yielding a 3 dB RC frequency of 0.76 THz for a broadband $70\,\Omega$ antenna whereas, a photoconductor with silver (Ag) nanowire (NW) as nanoelectrode shows a device capacitance of $< 0.1\,\mathrm{fF}$ [37]. To realize such lateral photoconductors, a controlled alignment technique of the 1-D, single-crystalline Ag-NWs is demonstrated in this chapter. The primary reason for choosing Ag-NWs are their high electrical and thermal conductivities of $6.3 \cdot 10^7\,\mathrm{S/m}$ and $429\,\mathrm{W/(m\,K)}$, respectively [94]. As discussed in the preceding chapter, MEMS-tunable VCSELs prove their potential for CW THz photomixing. A compact and fully integrated photomixing setup is potentially realized when the inherently low-output power of a MEMS-VCSEL could effectively drive a CW photoconductor. In this context, Ag-NW-based lateral photoconductors (NW-photoconductors) seem to be promising. The research starts with fabricating NW-photoconductors both on 850 nm LTG-GaAs and 1550 nm LTG-InGaAs materials. During the course, the performance of the Ag-NWs at elevated temperature is found detrimental, and a detailed analysis of the failure mechanisms are addressed in this chapter.

5.1 Device Fabrication

The fabrication of the NW-photoconductors is composed of two functional procedures. Firstly, a broadband log-periodic antenna [95] is fabricated onto the photoconductive material of LTG-GaAs or LTG-InGaAs by using few processing steps. For

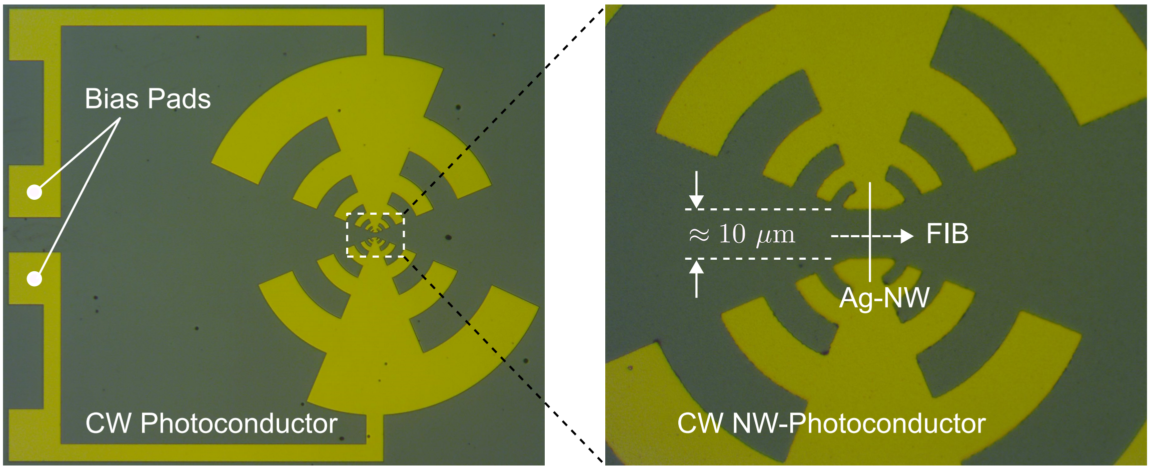

Figure 5.1: LTG-GaAs photoconductor. The zoom in view schematically shows the desired alignment of a metallic NW, the following FIB cutting accomplishes a nanoelectrode-based photoconductor, i.e., NW-photoconductor.

this work, various LTG-GaAs samples are employed concerning carrier recombination lifetime ranging from 190 fs–350 fs. With the aid of standard photolithography, the antenna structure is patterned onto the wafer with a thin photoresist [1]. On the patterned wafer, Ni/Au layers with a thickness of 20 nm 100 nm, respectively, are thermally evaporated. The following lift-off in the acetone accomplishes the first part of the fabrication of the device. Such a fabricated LTG-GaAs device is presented in Fig. 5.1 where the antenna structure connected to an individual DC bias pad will be denoted as antenna electrode.

The second functional procedure of the device fabrication is to align/assembly Ag-NW/NWs across the spacing (≈ 10 μm) of the antenna electrodes as shown by the highlighted section of Fig. 5.1. Such an alignment would short the antenna electrodes. To incorporate the nano-cathode and nano-anode, focused ion beam (FIB) or wet etching procedures can be used to cut the NW/NWs in the direction of the arrow into two segments. The gap between the segments is of practical importance based on the photocarrier transport mechanisms. The optimum value of this gap lies in the range of 1 μm–2 μm. In the present work, the gap will be termed as tip-to-tip distance. In Ref. [37], Ag-NWs alignment is realized by manually controlled random spin and air-flow methods. It is apparent that a controlled alignment technique should replace these tedious and low-yield alignment procedures. To realize the second functional procedure of the device fabrication, we use the dielectrophoresis

---

[1] MicroChemicals, AZ 1518

(DEP) technique. This technique requires no capital-intensive equipment and can be performed at ambient temperature and pressure for the alignment of all kinds of nanowire materials [96]. In this work, commercially available Ag-NWs[2] immersed in ethanol are used with average diameter and length of $d_{\mathrm{NW}} = 120\,\mathrm{nm}$ and $l_{\mathrm{NW}} = 20\,\mu\mathrm{m}$, respectively. To avoid any ambiguity, the fully fabricated devices will be phrased as NW-photoconductors.

5.2 Dielectrophoresis Technique

5.2.1 Theory of Dielectrophoresis

The term DEP is first introduced by Pohl [97] referring to an effect where a polarizable particle is carried as a result of its dielectric properties [98]. With the presence of inhomogeneous/non-uniform electric fields, the force acting on each side of the polarizable particle will be different to cause a net movement in its host medium. In this work, Ag-NWs immersed in ethanol are used to bridge the gap between the antenna electrodes of the CW photoconductors by using DEP technique. An applied potential causes non-uniform electric fields to generate the DEP force, F_{DEP} which captures and orients few of the NWs to bridge the gap. F_{DEP} on a single NW is given by [99]

$$F_{\mathrm{DEP}}\left(t\right) = \left[s\left(t\right) \cdot \nabla E(t)\right], \tag{5.1}$$

where $s\left(t\right)$ is the induced dipole moment of the NW and ∇ is the gradient operator. $s\left(t\right)$ is further denoted as [99]

$$s\left(t\right) = \varepsilon_{\mathrm{m}} V_{\mathrm{NW}} K E\left(t\right), \tag{5.2}$$

where ε_{m} is the absolute permittivity ($\varepsilon_{\mathrm{r}}\varepsilon_0$) of the solvent medium (ethanol), V_{NW} is the volume of the NW and K is the complex polarization factor. In the case of a spherical particle, K is referred to as the Clausius–Mossotti factor [100], whereas for nanorods or NWs, this is given by[99, 101]

$$K = \left[\frac{\varepsilon^*_{\mathrm{NW}} - \varepsilon^*_{\mathrm{m}}}{\varepsilon^*_{\mathrm{m}} + \left(\varepsilon^*_{\mathrm{NW}} - \varepsilon^*_{\mathrm{m}}\right) A_\alpha}\right], \tag{5.3}$$

where $\varepsilon^*_{\mathrm{NW}}$ and $\varepsilon^*_{\mathrm{m}}$ are the complex permittivities of the NW and solvent medium, respectively. The factor A_α is termed as the shape-dependent depolarization factor [96]

---

[2] ACS Material

describing the shape anisotropy of the particle. The NWs are of cylindrical-shaped and highly anisotropic. For an elongated cylindrical NW, the polarizability along its length is much higher than its radial orientation. For such a case [99, 100, 102],

$$K = \frac{\varepsilon^*_{\mathrm{NW}} - \varepsilon^*_{\mathrm{m}}}{\varepsilon^*_{\mathrm{m}}}. \tag{5.4}$$

Since the imaginary part of ε^* contains the conductivity σ and angular frequency of the applied potential as

$$\varepsilon^* = \varepsilon - i\frac{\sigma}{\omega}, \tag{5.5}$$

K is also a function of the conductivity and angular frequency of the applied field as well. As the electric field and NW polarization are in phase, therefore, the time averaged DEP force is given by [99, 103]

$$\langle F_{\mathrm{DEP}}\left(t\right)\rangle = \frac{1}{2}\Re\left\{s \cdot \nabla E^*\right\}, \tag{5.6}$$

which is further expanded as

$$\langle F_{\mathrm{DEP}}\left(t\right)\rangle = \frac{1}{2}\varepsilon_{\mathrm{m}}\pi r^2_{\mathrm{NW}} l_{\mathrm{NW}}\Re\left\{K\right\} \nabla \mid E_{\mathrm{rms}} \mid^2, \tag{5.7}$$

with $V_{\mathrm{NW}} = \pi r^2_{\mathrm{NW}} l_{\mathrm{NW}}$ where r_{NW} is the radius of Ag-NWs and E_{rms} is the RMS value of the applied electric field. For $\Re\left\{K\right\} > 0$, the positive DEP force will attract NWs into the zone with increasing field strength.

To summarize, F_{DEP} depends on the square of the magnitude of the field and its frequency and also on the difference of the dielectric permittivities of NWs and the medium. It is apparent that F_{DEP} is zero if the field is uniform ($\nabla E = 0$). NWs will be attracted by the applied force towards the region with highest field gradient. For the presented photoconductors, the highest field gradient exists between the spacing of the antenna electrodes across which the NWs should be bridged (see Fig. 5.1). Thicker and longer NWs will experience higher force than the shorter and thinner ones. F_{DEP} also depends on the ratio of the spacing of the antenna electrodes to the length of the NWs where for the same spacing, longer NWs will experience higher force [104]. With all these dependencies, the first alignment of a NW reduces the local electric field preventing further assemblies of NWs in its proximity [99]. That is particularly advantageous for the present work. Otherwise, too many assemblies would give rise increased device capacitance. However, further assemblies of NWs can still be possible with an increasing applied voltage.

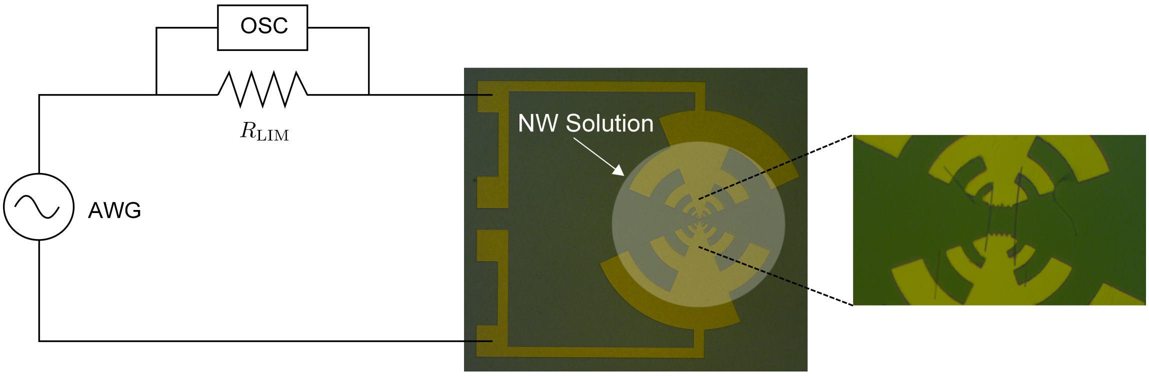

Figure 5.2: Schematic representation of the DEP setup. The zoom in view shows two of the aligned Ag-NWs bridging and shorting the antenna electrodes of a test device.

5.2.2 Dielectrophoretic Alignment of Silver Nanowires

Figure 5.2 schematically shows the DEP setup where an arbitrary waveform generator (AWG)[3] biases a test photoconductor through the bias pads. A current limiting resistor, $R_{\mathrm{LIM}} = 10\,\mathrm{k\Omega}$ is inserted in the circuit to protect any short-circuit current. The DEP-alignment of Ag-NWs is monitored by observing the potential drop across the R_{LIM} with a time-domain oscilloscope (OSC). Ag-NWs are densely immersed in ethanol, therefore, a dilution of the solution is necessary to avoid aggregation. With an applied potential, a little droplet of the diluted solution placed around the antenna electrodes is dispersed as highlighted by the transparent circle. The dispersed NWs move towards the region of the highest field intensity which is found across the spacing of the antenna electrodes. Successful alignment of the NWs shortening the antenna electrodes is read by the potential drop across the R_{LIM}. The applied potential is turned off only after the complete evaporation of the solution to avoid any disruption of the adhered (aligned) NWs. The evaporation depends on the size of the dispersed volume of solution; however, this lies in the range of few tens of seconds in our case. Assemblies of two Ag-NWs with $V_{\mathrm{pp}} = 2\,\mathrm{V}$ and $f = 50\,\mathrm{kHz}$ are displayed in the zoom in view of Fig. 5.2. Unsuccessful assemblies leave the NWs scattered around, and these contribute to device parasitic capacitance. To avoid the process complexities associated with FIB or wet etching, through an alternative approach, the wafer is first passivated with a 500 nm thick $\mathrm{Si_xN_y}$ layer. Figure 5.3a shows an unpassivated device while Fig. 5.3b illustrates a photolithographic pattern over the passivated layer of the same device. The passiva-

---

[3] Agilent, 33220A

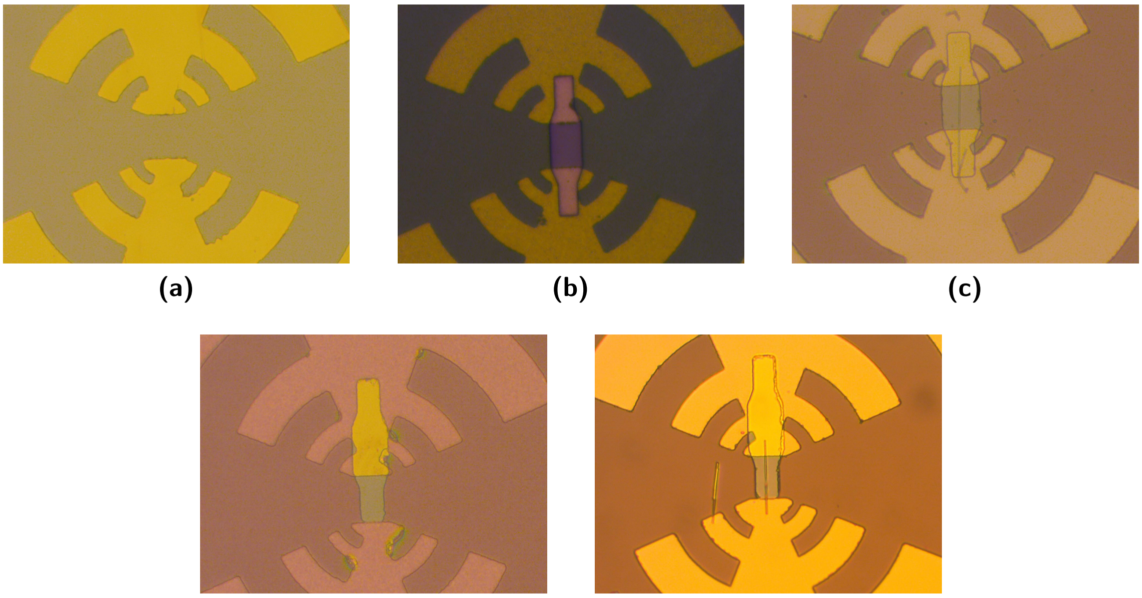

Figure 5.3: 850 nm LTG-GaAs photoconductors: (a) Unpassivated device. (b) Photolithographic pattern to etch the Si_xN_y passivation layer for equal opening of the antenna electrodes and (c) the subsequent DEP-alignment of the Ag-NW shortening the antenna electrodes. (d) With a displaced photolithographic pattern followed by the etching of the Si_xN_y layer opens only one antenna electrode and (e) the subsequent DEP-alignment shows the Ag-NW bridging the antenna electrodes without any short.

tion layer of the patterned area, as well as that on the bias pads, are etched away by the following SF_6 etching. As can be seen in Fig. 5.3c, the successive DEP-alignment of a Ag-NW ($V_{\mathrm{pp}} = 4\,\mathrm{V}$ and $f = 30\,\mathrm{kHz}$) shortens the antenna electrodes. Would there be more NWs scattering around, they will not contribute to any parasitic capacitance due to the passivation layer. Since this type of etching does not help to avoid the FIB process, a displaced etching as shown in Fig. 5.3d is performed. Since the intentional etching exposes only one antenna electrode, the successive DEP-alignment of the Ag-NW ($V_{\mathrm{pp}} = 6\,\mathrm{V}$, $f = 50\,\mathrm{kHz}$) as shown in Fig. 5.3e avoids the unwanted short-circuiting. Due to the high bendability of metallic NWs [105], the aligned ones as shown in Figs. 5.3c and 5.3e is overlaid onto the substrate. Note that, a higher voltage is required due to the passivation layer when compared to the case with the unpassivated devices. For the event of the non-displaced/displaced etching, a step gradient of 500 nm exists between the etched and unetched area. At

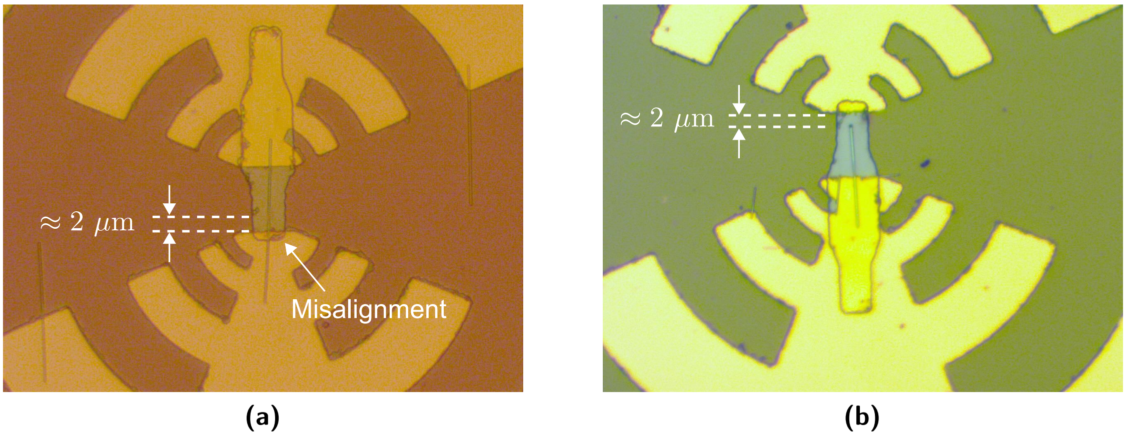

(a) (b)

Figure 5.4: (a) DEP-alignment of Ag-NW across the electrode-contacts with pseudo-tip-to-electrode distance of around 2 µm. (b) DEP-alignment enabling tip-to-electrode distance of around 2 µm.

one hand, the NW approaching to bridge the spacing needs to be pulled down; this consequently necessitates the need for higher potential. On the contrary, DEP force depends on the fluid (ethanol) flow and nanowire–surface interactions [99]. The passivation layer reduces the viscosity of the ethanol as well as interacts more with NWs. Consequently, a higher potential is required.

If there exists any misalignment from the photolithography process, the following etching exposes a portion of the other antenna electrode. Such a case is shown in Fig. 5.4a with the subsequent NW alignment ($V_{\mathrm{pp}} = 6\,\mathrm{V}, f = 50\,\mathrm{kHz}$). In this case, the misalignment is not significant, as well as the step gradient of the passivation layer on this side avoids any chance of short-circuiting. With the aligned NWs on the passivated devices as shown in Figs. 5.3e and 5.4a, a requirement needs to be met which is discussed in light with the NW alignment in Fig. 5.4b. Apart from a long overlap with the unpassivated antenna electrode, the NW overlays on the substrate due to bending, and the respective tip has an offset of $\approx 2\,\mu\mathrm{m}$ with the opposite antenna electrode. This distance, in contrast with the already mentioned tip-to-tip distance, will be regarded as tip-to-electrode distance. Though not clearly visualized in the optical image of Fig. 5.3e, the point from where the overlaid NW ascending (due to the height gradient) towards the passivated antenna electrode is marked as the pseudo-tip. The relevant pseudo-tip-to-electrode distance of $\approx 4\,\mu\mathrm{m}$ is not favorable for higher photocurrent generation. For the device as shown in Fig. 5.4a has a pseudo-tip-to-electrode distance of $\leq 2\,\mu\mathrm{m}$. Such alignment is desirable for a higher photocurrent (THz signal) generation.

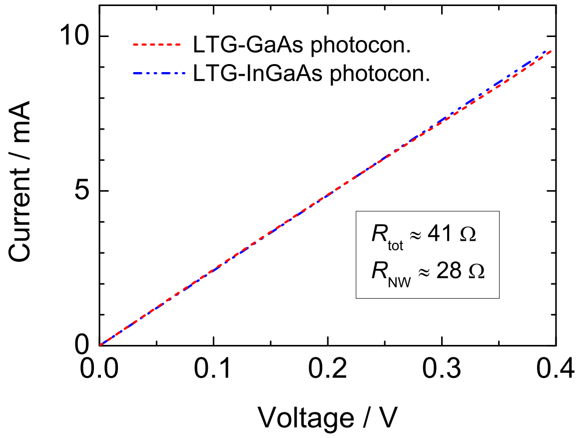

Figure 5.5: DEP-alignments of Ag-NWs on the unpassivated GaAs and InGaAs photoconductors show a maximum short-circuit current of ≈ 9.7 mA. The reciprocal of the slope for each of the voltage-current curve shows a total resistance of $\approx 41\ \Omega$.

Unfortunately, the chance of getting an optimum pseudo-tip-to-electrode/tip-to-electrode distance on a passivated (displaced) structure is random. This is due to the higher thickness of the passivation layer which affects the bendability of NWs. In the present case, the overall yield is of $< 50\,\%$. To retain the precise alignments with high yield, the thickness of the passivation layer must be reduced.

5.3 Static Characterization

Short-circuit current is a potential measure of assessing photocurrent carrying capability of NWs. To measure that, DEP-alignment of Ag-NWs on the unpassivated photoconductors are carried out to bridge the antenna electrodes ($V_{\mathrm{pp}} = 2$ V and $f = 50$ kHz). Though the short-circuit current is not material dependent, this is yet measured for both the GaAs and InGaAs NW-photoconductors. In each case, reliable short-circuit current up to ≈ 9.7 mA (0.4 V) is measured (2-wire experiment). The experimental results are demonstrated in Fig. 5.5 [106]. Using the Ag resistivity of $15.87\,\mathrm{n\Omega \cdot m}$ at 20 °C, the NW resistance of $R_{\mathrm{NW}} = 28\ \Omega$ is classically obtained for the mentioned diameter and length. From each of the voltage-current curves, as illustrated in Fig. 5.5, the total resistance R_{tot} is read from the reciprocal of the respective slope. For both cases, one calculates of $R_{\mathrm{tot}} \approx 41\ \Omega$. By subtracting the value of R_{NW} from that of R_{tot}, one reads the contact resistance of $R_{\mathrm{con}} \approx 13\ \Omega$.

The photocurrent measurement of the LTG-GaAs NW-photoconductor is presented

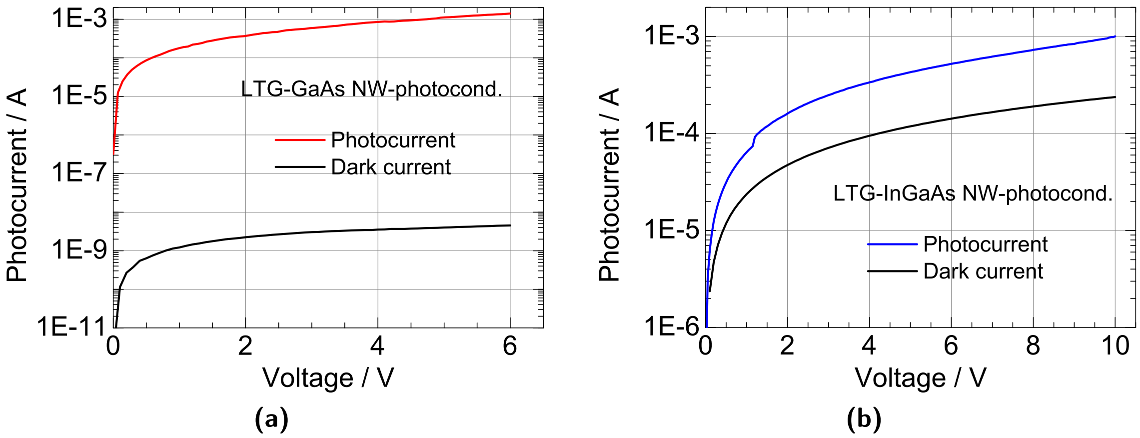

Figure 5.6: Static characterizations of CW NW-photoconductors as a function of the bias voltage: (a) 850 nm GaAs device shows reliable photocurrent of 1.4 mA (6 V) with associated dark current of 4.5 nA. (b) 1550 nm InGaAs device shows reliable photocurrent of 1 mA (10 V) with associated dark current of 238 µA.

in Fig. 5.6a [106]. For a DC potential of 6 V, the measured dark current is 4.5 nA. For the photocurrent measurement, the CW power of a 850 nm DFB laser is focused onto the device emplyoing a PMF. The photocurrent is measured as high as 1.4 mA with the DC voltage of 6 V and $P_{\text{opt}} \approx 20$ mW. The calculated on-off ratio (OOR) is $\approx$ 55 dB. For the LTG-InGaAs NW-photoconductor, as illustrated in Fig. 5.6b, the dark current of 238 µA is measured for a DC voltage of 10 V [106]. To measure the photocurrent, the CW power of a 1550 nm DFB laser is focused onto the device through a lens system with a spot diameter of 4.65 µm. The measured photocurrent is as high as 1 mA with the DC voltage of 10 V and $P_{\text{opt}} \approx 20$ mW. The OOR for the InGaAs NW-photoconductor is $\approx$ 6.2 dB. The low OOR of this device results from the high dark current which arises from the impurities of InGaAs material itself. As a matter of fact, the InGaAs NW-photomixers are not suitable for the CW operation at the moment, instead, these might be used for the pulsed operation.

In the THz experiment, the GaAs NW-photoconductor is illuminated with the beat signal from two DFB lasers operating around 850 nm. However, the device does not respond to the beat signal to produce the expected photocurrent. The photocurrent of few hundreds of nanoampere with OOR of $< 2\,\%$ indicates the failure of the Ag-NW nanoelectrode. The same phenomenon is also recognized for the InGaAs NW-photoconductor. Repeated photocurrent measurements for another GaAs NW-photoconductor are carried out to investigate the reproducibility. After several trials, the sudden drop of the photocurrent indicates the onset of some

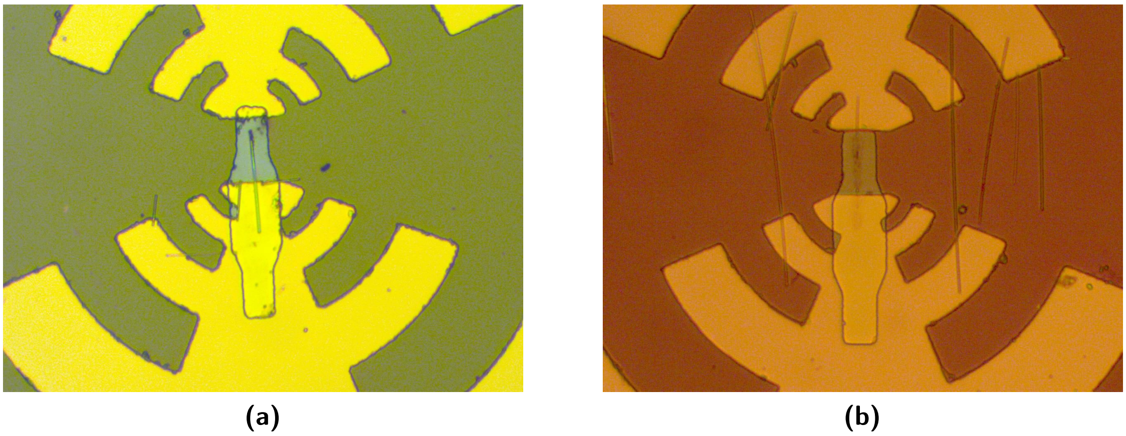

Figure 5.7: Optical images showing failure of Ag-NWs on passivated (displaced) GaAs NW-photoconductors: (a) the dark shadow on the tip of the NW shows the onset of the failure. (b) NW failure both on the unpassivated antenna electrode and substrate.

failure mechanisms of the nanoelectrodes. The failure of the Ag-NWs for many other devices are likewise found common. The following section investigates the basis of the failure mechanisms of the Ag-NWs as nanoelectrodes.

5.4 Nanowire Failure Mechanisms

The Ag-NW of the device as already shown in Fig. 5.4b undergoes a failure after static characterization. The corresponding optical image in Fig. 5.7a shows a blackish spot on its tip. This is clearly in contrast with the remaining part. Figure 5.7b shows another GaAs NW-photoconductor with its nanoelectrode being completely damaged. The other Ag-NWs aligned along the gradient fields between the antenna electrodes seem to be intact. In the following sections, a detailed analysis of these observed failures of Ag-NWs is discussed.

5.4.1 Electromigration

The failure of the Ag-NWs can be due to the onset of electromigration [107]. For the metallic conductors, the momentum transfer between the conducting electrons and metallic ions constitute a mass transport mechanism known as electromigration.

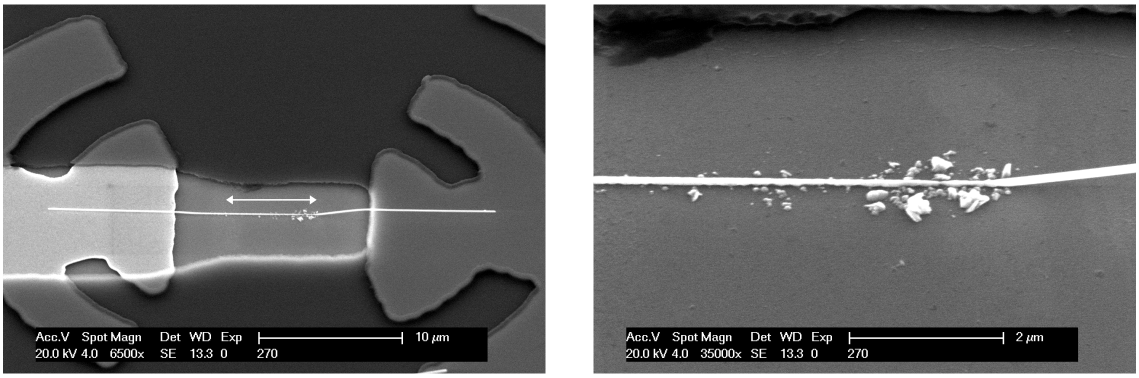

(a) **(b)**

Figure 5.8: (a) SEM image showing severe morphological transformations around the point where the laser beam is focused. (b) The transformations continue only along the length where the NW is in contact with the substrate.

The term wind force F_{wind} indicates the scattering of the conduction electrons by the metal atoms leading to a mass transport in the direction of the electron flow (from the cathode to anode) [107]. In contrast, the term direct force F_{direct} indicates the electrostatic interaction of the metallic ions with the external fields leading to a mass flow in the opposite direction (from the anode to cathode) [107]. For the single-crystalline Ag-NWs as used in this work, the relation of $F_{\text{wind}} < F_{\text{direct}}$ shows a reversed electromigration where the mass transport occurs in the direction of the electron flow [107]. This is attributed by forming voids at the anode and hillocks at the cathode [108] which is in contrast observed for other metallic NWs, such as gold NWs [109]. With reversed current direction, however, voids and hillocks alternate with the respective anode and cathode [108, 110]. Figure 5.8a shows the scanning electron microscopy (SEM) image of a GaAs NW-photoconductor. As indicated by the arrow, the Ag-NW overlaid along the substrate undergoes some damages. The rest of the NW remains single-crystalline which can be distinguished from the remaining part. The pseudo-tip-to-electrode distance for this device is $\approx 3\,\mu\text{m}$ within which the incident laser beam is focused. With a zoom in view as shown in Fig. 5.8b, the pseudo-tip through which the photogenerated carriers are collected undergoes severe damage. With close inspection, no concrete evidence of having voids or hillocks is observed. Short-circuit current measurement (no substrate involved) for a single-crystalline Ag-NW is reported in Ref. [110] where the voids and hillocks are formed with much higher current ($> 15\,\text{mA}$) for longer-time operation. For the case in this work, it is worth to mention that the short-circuit current measurement (see Fig. 5.5) involving the effect of substrate shows no electromigration behavior with a current of $> 9\,\mathrm{mA}$. Therefore, the device with photocurrent of $> 1\,\mathrm{mA}$ for few tens of seconds (see Fig. 5.6a) undergoes electromigration failure is less likely. One criterion being common for all the devices is that the transformations of the Ag-NWs take place only under the photocurrent measurements. The changes are found to be severe only along the overlaid part of the NWs onto the substrate. With this view, inspections are carried out concerning what is known as Rayleigh instability.

5.4.2 Rayleigh Instability

The morphological instabilities above a certain temperature may fragment NWs into a chain of nanospheres. Plateau pioneered the theoretical work that a liquid cylinder undergoes radius perturbations of wavelength λ_{rod} exceeding the circumference of the cylinder [111]. Based on this, Lord Rayleigh continued with the extensive analysis on the instability of nonviscous liquid jets. Afterward, Nichols and Mullins applied Rayleigh's work to explain the instability for solid rods. The morphological instability for an infinitely long cylindrical rod with isotropic surface energy is expressed through the sinusoidal perturbation of its radius of the form [112, 113]

$$\Delta r_{\mathrm{rod}} = r_{\mathrm{rod}} + A_{\mathrm{per}} \sin \frac{2\pi}{\lambda_{\mathrm{per}}} z, \tag{5.8}$$

where r_{rod} is the initial unperturbed radius of the rod, A_{per} and λ_{per} are the amplitude and wavelength of the perturbation, respectively and z is the coordinate along the symmetry axis of the rod. The morphology of the rod is unstable against the perturbations with a minimum wavelength of $\lambda_{\mathrm{per,min}} = 2\pi r_{\mathrm{rod}}$. For a maximum wavelength $\lambda_{\mathrm{per,max}}$, the perturbation grows with a maximum rate. The morphological changes of various metallic NWs as a function of the annealing temperature have been studied where the thermally induced transformations are due to the Rayleigh instability [93, 112, 113, 114]. In all these works, the onset of the morphological changes of the metallic NWs at temperatures far below the melting point of the respective bulk materials is reported. Due to the Rayleigh instability for a range of annealing temperatures, the NWs are seen to fragment into sections with varying lengths. With increasing temperature, NWs transform into nanospheres [93]. Thinner NWs are prone to fragment at lower annealing temperature than the thicker ones [112]. As shown in Fig. 5.9, the aligned NW on a GaAs NW-photoconductor undergoes morphological damage. The fragmentation of the NW into a linear chain with different cylindrical segments can be seen on the unpassivated antenna electrode, whereas on the substrate, the NW is fragmented

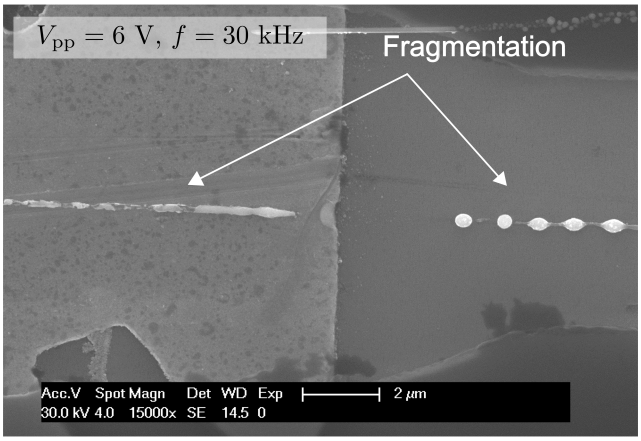

Figure 5.9: Morphological transformations due to Rayleigh instability imaged by SEM: the NW fragments into varying lengths of cylindrical segments on the left side, decays into spheres and peanut-shaped segments on the right side.

into peanut-shaped and spherical segments. The cylindrical or peanut-shaped segments will eventually decay into single spheres with longer time of operation [112]. The diameter of the spheres is given by $3.78 \cdot r_{\mathrm{rod}}$ where the spheres are ranged with $\lambda_{\mathrm{per,max}} = 8.89 \cdot r_{\mathrm{rod}}$ [115]. Since the radius of Ag-NWs is 60 nm ($d_{\mathrm{NW}} = 120$ nm), the diameter and $\lambda_{\mathrm{per,max}}$ of the spheres are calculated to be of ≈ 0.23 µm and ≈ 0.54 µm, respectively. Though the diameter of the spheres as shown in Fig. 5.9 matches to the calculated dimensions, however, the $\lambda_{\mathrm{per,max}}$ is smaller than what is observed. The equations for the diameter and $\lambda_{\mathrm{per,max}}$ are valid for polycrystalline NWs, where their values for single-crystalline NWs are found higher [116]. For the Ag-NW shown in Fig. 5.8, the ultimate decay to spheres does not take place, but the presence of the satellite particles indicate the onset of morphological transformations [113]. Characterization with prolonged time would result in decaying to spheres as demonstrated in Fig. 5.9.

5.4.3 Corrosion

It is reported in Ref. [116] that a single-crystalline gold nanowire with a diameter of 132 nm takes four hours to decay into spheres at an annealing temperature of 700 °C. Though the respective parameters for Ag-NWs might be different, the presence of hundred degrees Celsius would cause severe damage to the underlying semiconductor decomposing at temperatures above 700 °C. This is clearly not the case. Since the observed fragmentation of Ag-NW matches closely to the morphological changes predicted by Rayleigh instability, there might be some other factors accelerating the onset of this phenomenon at much lower temperature. In the case of current conduction through NWs, as reported in Ref. [117], the subsequent Joule heating elevates the temperature of NWs than that of the average surface temperature. This might be severe when NWs form resistive junctions. For both of the Ag-NWs, as shown in Figs. 5.8 and 5.9, the corresponding transformations are critical along the way they are in contact with the substrate. Due to having a large surface-area-to-volume ratio of NWs, the resistive junction created with the substrate might give rise to immense temperature with the current flow. Moreover, the immense light spotted onto the substrate between tip-to-tip, or tip-to-electrode distance enhances the temperature substantially. Since we do not use any passivation layer for the NWs, they oxidize extremely quickly when exposed to air, i.e., NWs corrode with oxygen. At the Joule heating induced elevated temperature of operation, we believe that corroded NWs are accelerating the morphological changes which are predicted by Rayleigh instability.

For further investigation, NW-photoconductors are fabricated with unpassivated LTG-GaAs in order to observe the effect of the passivation layer. To prevent the short-circuiting, the spacing of the antenna electrodes ($\approx 30\,\mu\text{m}$)) are kept larger than the length of Ag-NWs. The left SEM image of Fig. 5.10a shows two of the Ag-NWs aligned on the unpassivated device where one has a tip-to-electrode distance of $\approx 1\,\mu\text{m}$. The other NW along the spacing as well as those oriented along the gradient fields between the electrodes do not undergo any failure. The zoom in view of this device as imaged by the SEM shows morphological changes of the optimally aligned NW. The intact NW which is not in the focus of laser beam carries negligible photocurrent. The intactness bears the testimony of the arguments as mentioned earlier with Rayleigh instability and corrosion. SEM image of a second device as in Fig. 5.10b shows the fragmentation of the optimally aligned NW (tip-to-electrode distance of $< 2\,\mu\text{m}$) while the other one remains intact for the same reasoning. The corresponding zoom in view confirms the onset of the morphological changes around its tip. Note that, repeated photocurrent measurements would further decay the NW.

The investigations so far covered in this work show concrete signs of morphological transformations of Ag-NWs. Being aware of that, LTG-GaAs NW-photoconductors are prepared with larger diameter NWs which are more robust than the thinner ones against the Rayleigh instability [112]. Moreover, smaller surface-area-to-volume of larger diameter NWs would show better performance at elevated temperature [117]. Figure 5.11a shows the optical image of a NW-photoconductor aligned with a larger diameter Ag-NW ($d_{\text{NW}} = 300\,\text{nm}$, $l_{\text{NW}} = 20\,\mu\text{m}$). Though repeated measurements show no photocurrent for this device, the latter inspection by SEM (Fig. 5.11b)

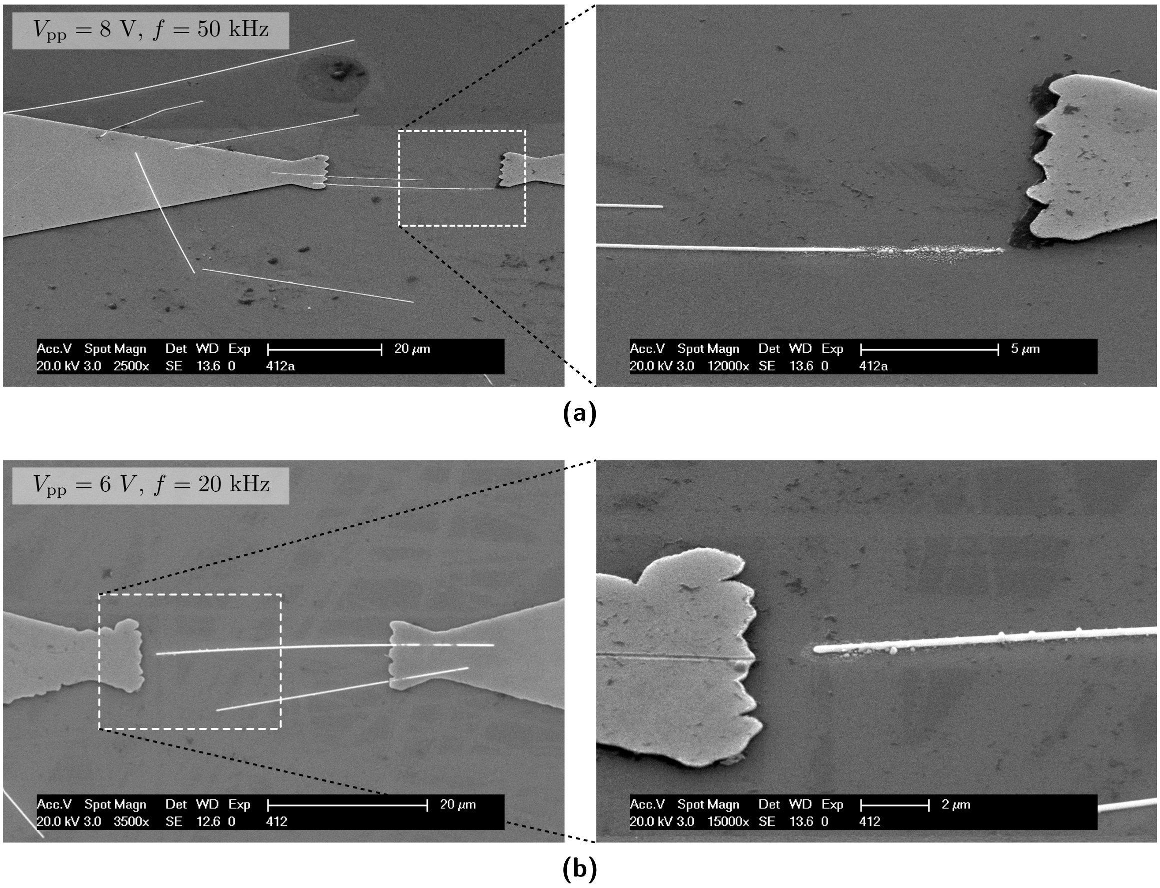

Figure 5.10: (a) DEP-alignment of Ag-NWs on an unpassivated LTG-GaAs photoconductor with larger spacing of the antenna electrodes. The zoom in view shows the transformations of the optimally aligned NW. (b) A second device where the aligned NW fails on the electrode side (left) and along the tip (zoom in view).

confirms a crystal defect preventing its contact onto the substrate. Even without this defect, however, it might not bend onto the substrate due to the increased stiffness. The associated solution is to use photoconductors with larger antenna gaps as those shown in Fig. 5.10.

5.5 Summary and Outlook

In this chapter, Ag-NWs as 1-D nanoelectrodes for CW photoconductors (NW-photoconductors) are presented. Commercially available single-crystalline Ag-NWs

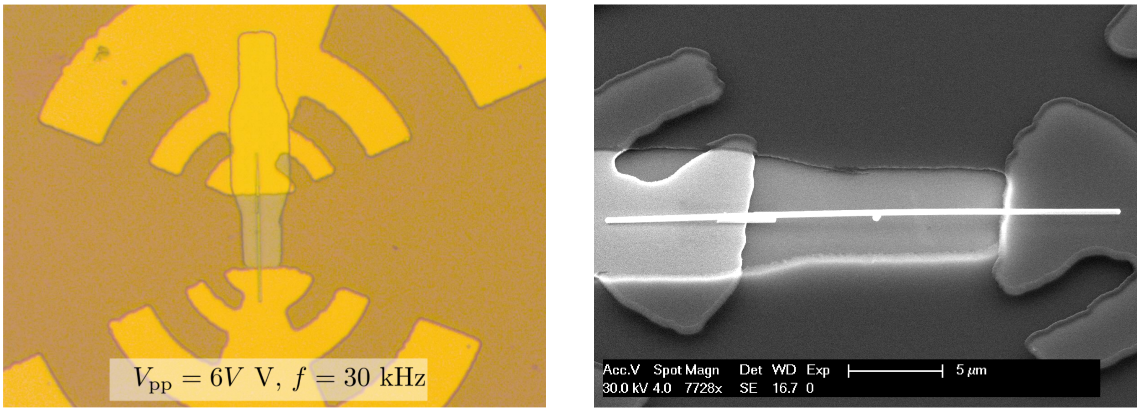

(a) **(b)**

Figure 5.11: (a) Optical image of a NW-photoconductor with $d_{NW} = 300\,\text{nm}$, $l_{NW} = 20\,\mu\text{m}$. (b) Corresponding SEM image shows a crystal defect preventing the NW bending onto the substrate.

($l_{NW} = 20\,\mu\text{m}$, $d_{NW} = 120\,\text{nm}$) are dielectrophoretically aligned across the antenna electrodes of LTG-GaAs (850 nm) and LTG-InGaAs (1550 nm) material systems. Successful alignments for unpassivated devices are accomplished using square wave potential with voltage and frequency ranging from $V_{pp} = 1\,\text{V}$–$2\,\text{V}$ and $f = 20\,\text{kHz}$–$50\,\text{kHz}$, respectively. FIB cutting is required to segment an aligned NW into nano-anode and nano-cathode with a tip-to-tip distance of 1 μm–2 μm. To avoid the process complexities associated with FIB cutting, an alternative approach aligns Ag-NWs on passivated structures where only one antenna electrode is exposed to avoid short-circuiting ($V_{pp} = 4\,\text{V}$–$10\,\text{V}$, $f = 20\,\text{kHz}$–$100\,\text{kHz}$). The relevant static characterizations of such NW-phtoconductors are summarized in Tab. 5.1. However, these devices suffer from a low-yield in terms of obtaining the non-optimum tip-to-electrode distance of $> 2\,\mu\text{m}$. Therefore, DEP alignment of the nanoelectrodes should be performed on unpassivated devices followed by the FIB cutting obtaining fully functional devices with a yield of almost 100 %.

At the moment, successful implementation of NW-photoconductors is hindered by the unexpected failures of the nanoelectrodes. The failure mechanisms are thoroughly inspected concerning electromigration, Rayleigh instability and corrosion. Numerous devices are characterized and inspected by SEM where morphological changes of the NWs are evident. Under laser illumination, the substrate area along which a NW is overlaid is intensely heated as long as the photocurrent starts flowing. The subsequent Joule heating is suspected to increase the local temperature which causes the morphological transformations of the NWs. The pattern of the

Table 5.1: Static measurements of the CW NW-photoconductors.

Materials	Static Characterizations	Measured
LTG-GaAs	Photocurrent	1.4 mA
	Dark Current	4.5 nA
	On-Off Ratio (OOR)	≈ 55 dB
LTG-InGaAs	Photocurrent	1 mA
	Dark Current	238 µA
	On-Off Ratio (OOR)	≈ 6.2 dB

transformations correlates very well to the predictions by Rayleigh instability. The unprotected NWs also corrode with oxygen in air. At the mentioned elevated temperature of operation, corrosion accelerates the onset of morphological changes. In any case, the behavior of the devices at elevated temperatures can potentially be improved by passivating with SiC or SiN layers, for example. Besides, alignments can be performed with thicker NWs since those are more robust against the Rayleigh instability at elevated temperature. Although a performance degradation is expected, this will still be better than that of the conventional photoconductors with interdigitated electrodes.

The initial idea is to drive a CW NW-photoconductor by the temperature-tuned optical beating of two commercially available 850 nm VCSELs. By using external lens objectives, the incident laser beam can be focused between the tip-to-tip/tip-to-electrode gap of 1 µm–2 µm. For the subsequent THz photomixing, the low-output power of VCSELs, at least, would be less pronounced considering the extremely low capacitances of the NW-photoconductors. For operation in the telecom wavelength range, CW tunable MEMS-VCSELs are confirmed as potential broadband optical sources for tunable THz photomixing. To realize miniaturized, low-cost photomixing systems, MEMS-VCSELs need to drive CW LTG-InGaAs NW-photoconductors. Though the presented LTG-InGaAs material shows high dark current, therefore, the NW-photoconductors for 1550 nm should be fabricated with a better quality material [118].

6 Summary and Conclusions

This thesis investigates tunable THz signal generation with a telecom wavelength compatible photomixer driven by the optical beat of a tunable MEMS-VCSEL and a fixed cavity length laser. Around telecom wavelengths, one THz corresponds to a detuning of the two heterodyned lasers by only about 8 nm. With an optimum fabrication, a surface micromachined electrothermally tunable MEMS-VCSEL features a tuning range of $> 100\,\mathrm{nm}$ ($> 12.5\,\mathrm{THz}$). Thus, a MEMS-VCSEL-based tunable THz system enables to cover the whole THz range with a single optical system, given that efficient photomixers with such large bandwidths are available.

After a brief introduction in chapter one, chapter two focuses on the theoretical fundamentals of VCSELs. Key output characteristics of non-tunable VCSELs are discussed concisely to show how those are maintained over the entire tuning range of tunable MEMS-VCSELs.

Chapter three reviews the detailed structure of MEMS-VCSELs and performs a systematic characterization with a particular focus on the parameters relevant for THz photomixing. These include mode-hop-free CW tuning characteristics with high spectral purity, wavelength stability, linewidth analysis, and polarization stability. Wavelength variations of MEMS-VCSELs are common due to the suspended membrane structure. The membrane is not only prone to external disturbances such as vibrations but also responses to many microforces acting on it. The overall outcome is identified through membrane deflections, i.e., wavelength variations of MEMS-VCSELs. The fluctuations fall into two categories, on the one hand, MEMS-VCSELs drift to few tens of GHz with a time scale slower than the thermal response of the membrane featuring a 3 dB thermal tuning cut-off frequency of $f_{\mathrm{mod,\,3\text{-}dB}} = 258.65 \pm 7.09\,\mathrm{Hz}$. With a detailed analysis, this chapter shows that the most detrimental slow drifts are due to temperature fluctuations and acoustic noises. To prevent long-term drifts of MEMS-VCSELs, on the one hand, a wavelength control circuit has been developed employing electrothermal feedback. The developed circuit can compensate these drifts with noise frequencies of $f < f_{\mathrm{mod,\,3\text{-}dB}}$. On the other hand, natural Brownian motion or external disturbances induce membrane fluctuations with a time scale faster than its thermal response and adversely affect the intrinsic linewidth of MEMS-VCSELs to few tens of MHz. These fluctuations can be canceled using a fast wavelength control circuit with a locking bandwidth significantly above the mechanical resonance frequencies of the membrane for electrostatically tunable MEMS-VCSELs. Nevertheless, the fluctuations are functions of the mechanical properties of the membrane which are obtained by well-known laser Doppler vibrometer experiment, and we report for the first time an alternative electro-optical measurement obtaining those likewise.

We employ the delayed self-heterodyne technique to measure the linewidth which remains below 55 MHz over the entire tuning range. It is worth mentioning that the DSH technique records the influence of noises above a time scale of 25 μs (40 kHz) generated by the 5 km fiber-optic delay. Since the noise sources with frequencies $f_{\text{mod, 3-dB}} < f < 40\,\text{kHz}$ are not observed during the linewidth experiment, MEMS-VCSELs fluctuate around the locking point with a 3 dB fluctuations bandwidth of $331.91 \pm 9.34\,\text{MHz}$ on the time scale present during photomxing experiment. Since the photomixing process requires two lasers of the same polarization, this chapter investigates the membrane to be a polarization selective reflector supporting anisotropic gain/loss in the active gain region avoiding polarization switching between the low-indexed crystal directions of the active medium. We experimentally show that MEMS-VCSEls are highly polarization stable with PSR of $> 20\,\text{dB}$ over the entire tuning range, yet limited by the employed setup.

Chapter four discusses the theoretical fundamentals of photomixing, and THz signal generation and radiation. With the state-of-the-art parameters of MEMS-VCSELs, this chapter demonstrates tunable THz photomixing with the unprecedented bandwidth of MEMS-VCSELs. The first photomixing setup utilizes a commercial photomixer driven either by a pair of a MEMS-VCSEL and a non-tunable VCSEL or the MEMS-VCSEL and a DFB laser. The employed MEMS-VCSEL has an output power of 0.77 mW with a mode-hop-free, CW tuning of 70 nm (8.8 THz) and a SMSR of $> 55\,\text{dB}$ over the entire tuning range. The VCSELs-based system drives the photomixer where the MEMS-VCSEL is stepped through 100 GHz-spaced lock points from 1.67 THz below the frequency of the non-tunable VCSEL to 1.73 THz above the frequency of the same laser, thus yielding a total scanned frequency span of 3.40 THz with direct power detection of a Schottky diode. With similar direct power detection, a frequency span of 3.40 THz is also covered by the MEMS-VCSEL and DFB laser driven photomixing system. The output of each VCSEL in these systems is amplified to reach the power required for the photomixing experiment. Separate TBFs are used after each amplification stage of VCSELs to get rid of the ASE noise to obtain a clear THz signal.

For achieving higher scanning resolution, we demonstrate a second system where the photomixer is driven by a MEMS-VCSEL and a DFB laser in homodyne field detection mode with a photoconductor. The employed MEMS-VCSEL has an output power of 1.5 mW with a mode-hop-free, CW tuning of 64 nm (7.92 THz) and a SMSR of $>$ 50 dB over the entire tuning range. This setup utilizes the polarization stability of the employed MEMS-VCSEL and thus leads to implement PM components solely at 1550 nm. The higher resolution is achieved by scanning the DFB laser in 100 MHz steps over its tuning range of about 540 GHz. Subsequently, the VCSEL is locked to a subsequent locking point with a frequency step of 400 GHz or 500 GHz, followed by a consecutive DFB laser scan. Repeating this procedure allows covering the whole tuning range of the photomixers employed in the setup of about 2.75 THz. No additional amplifier or TBF for the MEMS-VCSEL is necessary, simplifying the setup considerably. The employed photomixers yet limit the achieved bandwidth. Once improved photomixers are available, the electrothermally actuated MEMS-VCSELs will allow for a tuning range covering almost the complete THz domain with a single system.

A particular aspect of increasing the frequency coverage of photomixers is addressed in chapter five. We use dielectrophoresis technique to align Ag-NWs as nanoelectrodes to fabricate such CW NW-photoconductors at 850 nm and 1550 nm using corresponding LTG substrate materials. However, with initial characterization using DFB lasers with respective wavelengths, these devices fail due to the failure of NWs. It is observed under DC photocurrent operation that the temperature of NWs is increased due to Joule heating. Consequently, NWs are likely to undergo morphological changes at the Joule heating-induced elevated temperature. In light of known failure mechanisms, such as electromigration, corrosion or Rayleigh instability, we find that Rayleigh instability fragments the NWs. Corrosion with oxygen is also considered detrimental for the unprotected NWs. At the elevated temperature of NWs, corrosion further accelerates the onset of these morphological changes. To prevent this, future devices must be passivated with SiC or SiN protective layers.

For the realization of future miniaturized photomixing setup, two additional photomasks by the existing ones are designed which will support the future monolithic fabrication of tunable MEMS-VCSELs and non-tunable fixed cavity length VCSELs in the same run. The width and length of the footprint of a pair of a MEMS-VCSEL and a fixed cavity VCSEL are 0.42 mm and 0.92 mm. Such a pair of VCSELs will drive conventional or nanoelectrodes-based photomixers where a wavelength control circuit will lock and tune the MEMS-VCSEL with a resolution of, i.e., 1 GHz. Recently, MEMS-VCSELs are being mounted into transmitter optical subassembly (TOSA) modules. Similar packaging and isolation of a pair of VCSELs will considerably reduce the temperature fluctuations, acoustic and electronic noises of the MEMS-VCSEL to improve the wavelength stability.

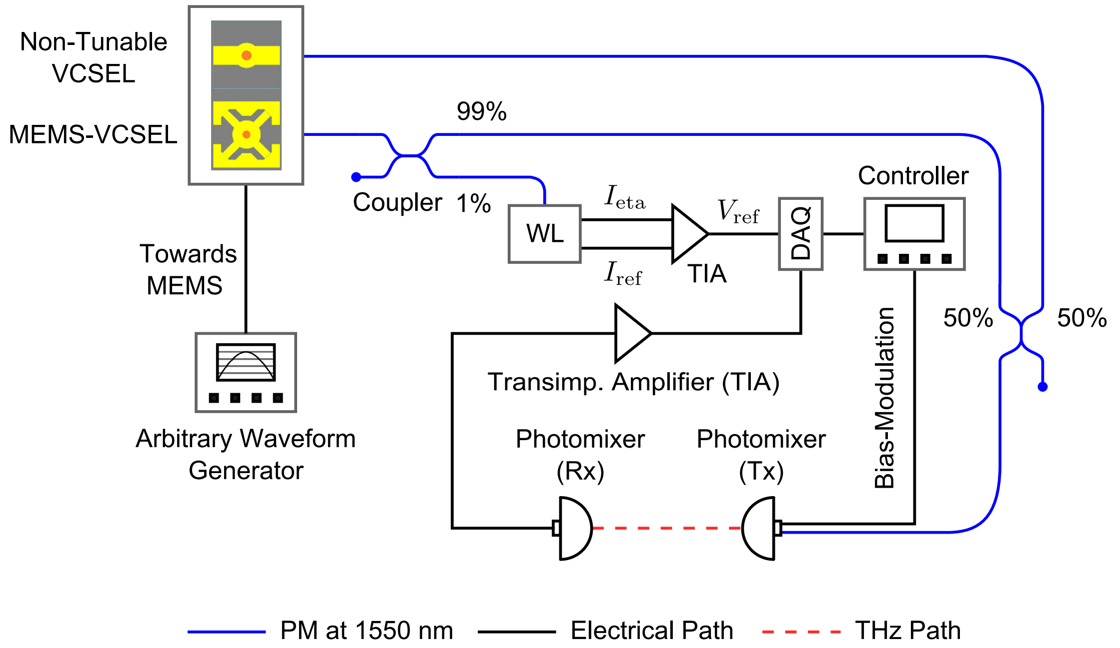

Figure 6.1: Future miniaturized THz photomixing setup driven by a pair of a MEMS-VCSEL and a non-tunable fixed cavity VCSEL.

For further miniaturization, Fig. 6.1 schematically shows a photomixing setup where a pair of VCSELs (photomask layout) will drive conventional or nanoelectrodes-based photomixers. This photomixing system will fully utilize the faster tuning speed of MEMS-VCSELs where the wavelength locking mechanism will not be required. However, a wavelength/frequency reference is needed which will be generated by a combination of a wavelength locker and a logarithmic transimpedance amplifier. As displayed in Fig. 6.1, an arbitrary waveform generator will modulate the membrane current of the MEMS-VCSEL in back and forth manner over its entire tuning range. For the detection, a fast data acquisition system (DAQ) with a controller will perform synchronized reading and time-averaging of the received data of the THz photomixer unless an adequate signal-to-noise ratio (SNR) is achieved. We thus aim to implement MEMS-VCSELs-based miniaturized CW tunable photomixing system which will benefit from the unprecedented tuning range of MEMS-VCSELs.

A Printed Circuit Board of the Wavelength Control Circuit

The wavelength control circuit is designed using Altium Designer. Figure A.1 shows the PCB of the designed circuit whose schematic is displayed in Fig. 3.20.

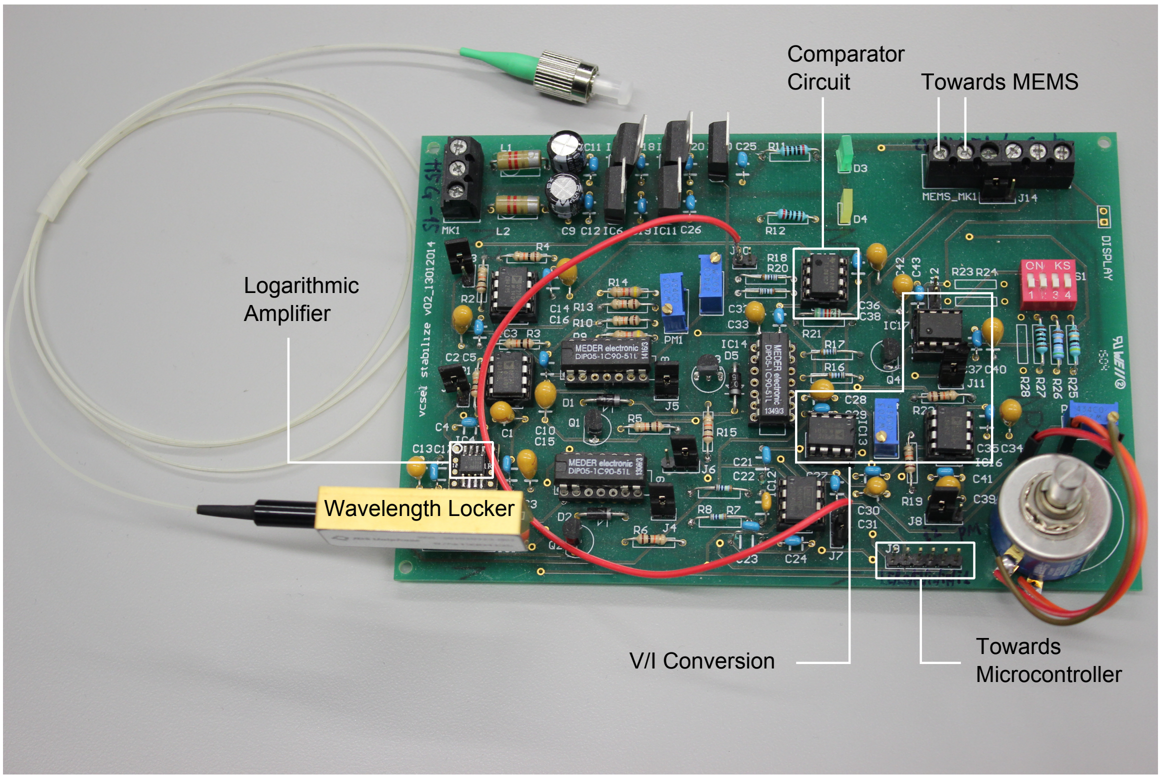

Figure A.1: PCB of the wavelength control circuit.

B Additional Characterization of MEMS-Tunable VCSELs

In this section, we will describe few more characteristics of the MEMS-VCSEL employed in the homodyne photomixing setup including efficiencies and diode ideality factor. It is worth to mention that all MEMS-VCSELs from this wafer do not lase over their entire FSRs. We investigate and figure out the reason behind this behavior with the help of the temperature tuning characteristics (see Sec. 3.2.2) of another MEMS-VCSEL from this wafer.

B.1 Efficiencies and Ideality Factor

Figure B.1a shows the CW *L*-*I*-*V* characteristics. The emission wavelength above the threshold is around 1560 nm for $T_s = 20\,^{\circ}\mathrm{C}$. The output power is as high as 2 mW limited by the large-area PD. Threshold current and threshold voltage are 5.4 mA and 1.03 V, respectively. The outer y-axis shows the CE calculated according to Eq. (2.39). Maximum CE of $\eta_c = 5.36\,\%$ is obtained for the operating conditions of $I_b = 17.7\,\mathrm{mA}$, $V_{LD} = 1.32\,\mathrm{V}$ and $P_{opt} = 1.26\,\mathrm{mW}$. The calculated DQE of this device is $\eta_d \approx 14.1\,\%$. Above the threshold, as shown in Fig. B.1b, the differential series resistance R_s is calculated to be $< 33\,\Omega$ and becomes as low as $\approx 20\,\Omega$ with the increasing I_b. From the differential resistance curve, the term $I_b dV_{LD}/dI_b$ is obtained. Below the threshold, this is a linear function of I_b with a slope equal to R_s and a y-axis intercept of $n_d k_B T/e$, where n_d is the ideality factor of the diode [43]. A substantial kink is observed at the threshold, and $I_b dV_{LD}/dI_b$ decreases from $n_d k_B T/e + I_b R_s$ to $I_b R_s$. Below the threshold, the y-axis intercept of the linear fit, as shown in Fig. B.1b, is 0.063. The corresponding calculated value for the ideality factor is $n_d \approx 2.5$.

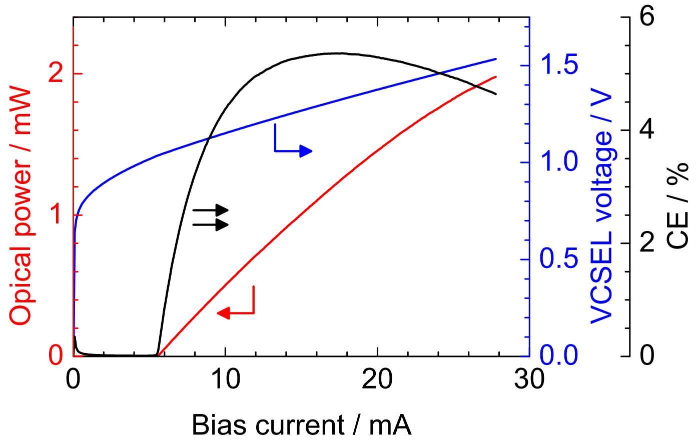

(a)

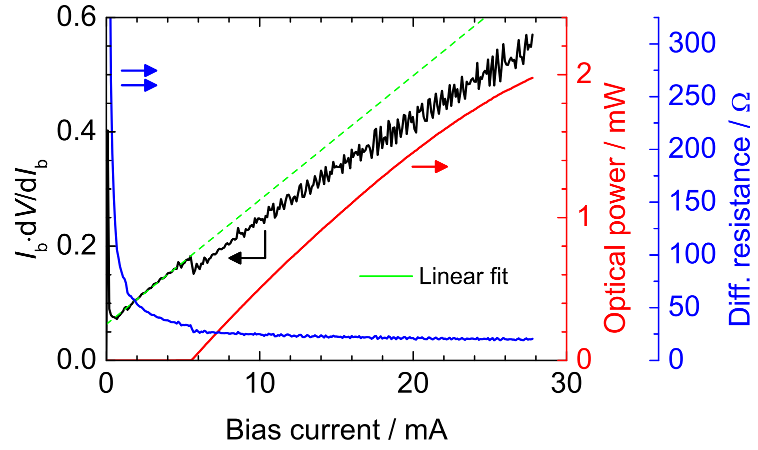

(b)

Figure B.1: (a) *L-I-V* characteristics with the outer y-axis indicating the calculated CE. (b) Differential series resistance and $I_b dV_{LD}/dI_b$ as a function of I_b.

B.2 Differential Quantum Efficiency over the Tuning Range

In Fig. B.2, DQE, and I_{th} of the MEMS-VCSEL employed in homodyne photomixing setup are plotted as a function of I_{MEMS}. The voltage profile of the laser from Fig. 4.5 correlates with the threshold current as shown in Fig. B.2. To discuss the DQE over the tuning range, the *L-I* characteristics with a large-area PD for different membrane currents are measured. The maximum of $\eta_d = 18\,\%$ is calculated with $I_{MEMS} =$

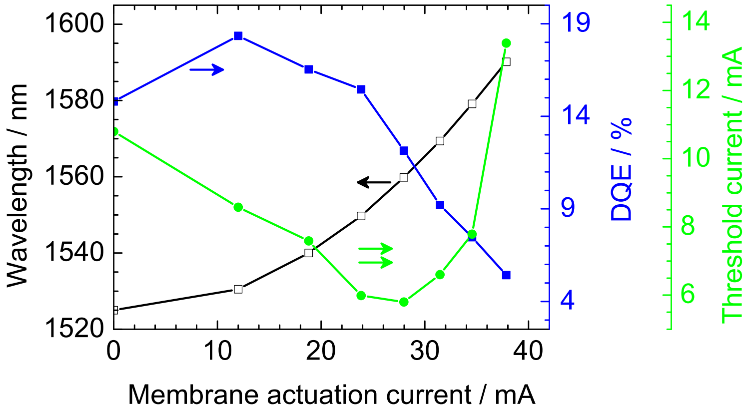

Figure B.2: Threshold current, DQE and emission wavelength as a function of the I_{MEMS}.

12 mA, $\lambda = 1530.5$ nm. As from Eq. (2.35), the electrical-to-optical conversion inside the cavity (higher SE) at this point is highest. The outcoupled power, however, is not highest there. At longer wavelengths, the membrane becomes less reflective decreasing the Q-factor of the cavity on the one hand. On the contrary, this results to increase the outcoupled power since the intensity transmission coefficient of the membrane is $T_{\mathrm{DBR,t}} = (1 - R_{\mathrm{DBR,t}})$.

B.3 Tuning Range versus Free Spectral Range Characteristics

We see in Fig. 4.5 that the MEMS-VCSEL does not laser over its entire tuning range (64 nm CW tuning versus FSR of 92 nm). In this section, we justify the associated reason with temperature tuning characteristics and corresponding voltage profiles of a MEMS-VCSEL as displayed in Figs. B.3a and B.3b, respectively. The variation of the voltage profile versus I_{MEMS} (e.g., for $T_s = 20\,^{\circ}\mathrm{C}$) as shown in Fig. B.3b can be described by considering a multitude of wavelength-dependent effects, such as combined reflectivity of the two DBR mirrors, the overlap of the standing wave pattern with the gain medium (confinement factor) or with lossy parts of the laser structure. The phenomenon is revealed in the measured voltage profile which therefore traces out the behavior of the overall gain seen by the cavity resonance. The voltage trace features a minimum with $I_{\mathrm{MEMS}} = 11.2$ mA where the overall gain is highest, and the threshold current should be the lowest. With increasing actuation current from this point, a sharp increase of voltage implies high loss encountered

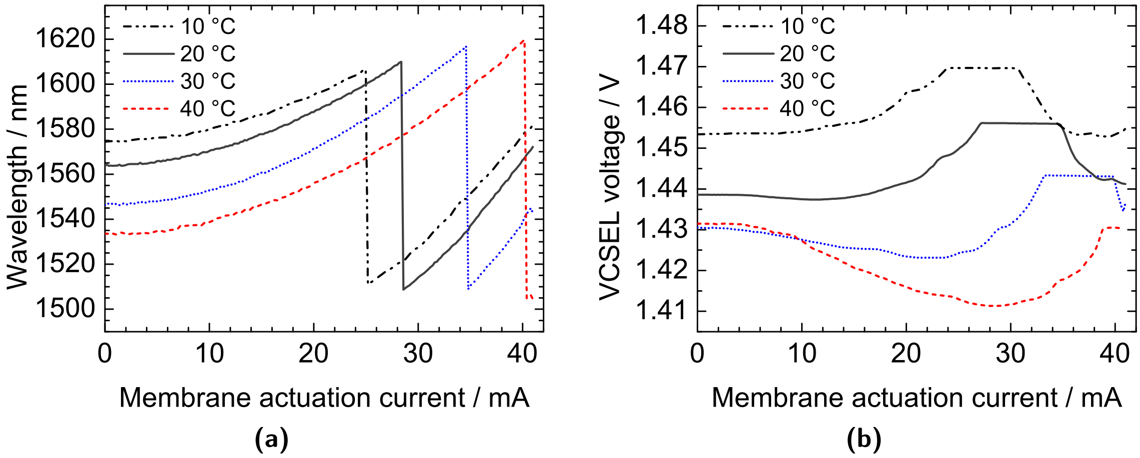

(a) **(b)**

Figure B.3: (a) Emission wavelengths across the tuning range at different substrate temperatures. (b) Corresponding voltage profiles of the MEMS-VCSEL.

by the cavity resonance. The complete cease of lasing can be understood from the plateau formed between actuation current of 27.2 mA and 34.6 mA. This possibly corresponds to the separation of quasi-Fermi level indicating higher threshold gain requirement of the MEMS-VCSEL to lase as well as mode competition. A longitudinal mode-hop occurs within this plateau with $I_{\mathrm{MEMS}} = 28.4\,\mathrm{mA}$ as shown in Fig. B.3a. However, it lases from $I_{\mathrm{MEMS}} = 34.6\,\mathrm{mA}$ as shown in Fig. B.3b where the voltage starts decreasing. The no-lasing zone of this longitudinal mode is probably restricted by degradation of confinement factor, combined reflectivity bandwidth of the mirrors and also by cavity gain detuning. For other substrate temperatures, the same phenomenon is observed in the voltage profiles as shown in Fig. B.3b. It is interesting to observe that the voltage profiles redshift with increasing substrate temperature. It is well-known that bandgap of the active medium shrinks with increasing T_{s} yielding an overall redshift of the gain spectrum [38]. The redshift is read by noting the individual membrane current corresponding to the onset of the plateau in Fig. B.3b, the associated emission wavelength for this membrane current is read from Fig. B.3a. For example, in Fig. B.3b, the membrane currents for the onset of the plateaus are 23.98 mA (10 °C) and 27.17 mA (20 °C). Therefore, the redshift is $(1606.2\,\mathrm{nm} - 1603.9\,\mathrm{nm}) = 2.3\,\mathrm{nm}$ for $\Delta T_{\mathrm{s}} = 10\,°\mathrm{C}$ where the wavelengths are read from Fig. B.3a. Thus an average value of 0.23 nm/K is read. The mean value of 0.25 nm/K is read from the overall redshift for a temperature range of 10 °C–40 °C.

Symbols and Acronyms

α	Spatial Average of the Intensity Attenuation Coefficient
α_{d}	Damping Factor
α_{fc}	Free Carrier Absorption
α_{H}	Linewidth Enhancement Factor
α_{ia}	Spatial Average of the Intrinsic Loss Coefficient in the Active Medium
α_{ip}	Spatial Average of the Intrinsic Loss Coefficient in the Passive Medium
α_{i}	Spatial Average of the Intrinsic Loss Coefficient
α_{m}	Mirror Losses
α_{th}	Thermal Expansion Coefficient
β	Complex Propagation Constant
$\delta P_{\mathrm{opt}}(t)$	Instantaneous Variations of Output Power
$\varDelta T_{\mathrm{total}}$	Total Noise Temperature fluctuation
$\varDelta x$	Membrane Displacement from the Equilibrium Position
$\varDelta\lambda_{\mathrm{ET}}$	Electro-Thermal Tuning of the MEMS-VCSELs
$\varDelta\lambda_{\mathrm{g}}$	Wavelength-Shift of the Peak Material Gain Wavelength
$\varDelta\lambda_{\mathrm{T}}$	Temperature-Induced Wavelength-Shift of the Cavity Mode
$\delta\nu(t)$	Frequency Jitter

$\Delta\nu_{\mathrm{DSH}}$	FHWM of the DSH Signal
$\Delta\nu_{\mathrm{L}}$	Intrinsic Linewidth
$\Delta\nu_{\mathrm{res}}$	3 dB Bandwidth of the Fundamental Resonance
η_{c}	Wall-Plug or, Conversion Efficiency
η_{d}	Differential Quantum Efficiency
η_{e}	External Quantum Efficiency
η_{i}	Internal Quantum Efficiency
Γ	Confinement Factor
γ_{c}	Phase Coupling Factor
Γ_{r}	Relative Confinement Factor
Γ_{xy}	Lateral Confinement Factor
Γ_{z}	Longitudinal Confinement Factor
λ	Emission Wavelength in Free Space
λ_0	Central Wavelength or Bragg Wavelength
λ_{DFB}	Emission Wavelength of the DFB Laser
λ_{g}	Bandgap Wavelength
λ_{q}	Emission Wavelength of Longitudinal Mode-Order of q
λ_{VCSEL}	Emission Wavelength of Fixed Cavity VCSELs
μ_{e}	Mobility of the Electrons
μ_{h}	Mobility of the Holes
ν	Lasing Frequency
ν_{AOM}	AOM Frequency

ν_{res}	Mechanical Resonance Frequency
ω	Angular Frequency
ω_0	Angular Bragg Frequency
Φ	Photon Flux
$\rho_{1,2}$	Radius of Curvature of Laser Mirrors 1,2
ρ_{m}	Material Density of the Membrane
τ_{coh}	Coherence Length
τ_{DBR}	Delayed Response Time of a DBR
τ_{d}	Time Delay of the DSH Decorrelation Fiber
τ_{LIA}	Integration Time of Lock-In Amplifier
τ_{ph}	Photon Lifetime
τ_{th}	Thermal Time Constant of a Membrane
φ_{air}	Round trip Phase in the Air Gap
φ_{eff}	Reflected Phase from a Membrane DBR
A_{m}	Area of the Membrane
d_{a}	Geometrical Thickness of the MQWs
d_{BTJ}	Diameter of the BTJ
d_{m}	Diameter of the Membrane
E_{g}	Bandgap Energy
E_{THz}	THz Electric Field Amplitude
F_{DEP}	DEP Force
f_{mod}	Modulation Frequency

F_{rp}	Radiation Pressure
g	Spatial Average of the Laser Gain
h_{m}	Thickness of the Membrane
I_{b}	Electrically-Injected Bias Current
I_{eta}	Etalon Current of the WL
I_{MEMS}	Membrane Actuation Current
I_{mod}	Peak-to-Peak Modulation Current
I_{noise}	Noise Current of the Homodyne Photomixing Setup
I_{ref}	Reference Current of the WL
I_{th}	Threshold Current of Lasers
K	Complex Polarization Factor/Clausius–Mossotti Factor
k	Wavenumber
k_{m}	Spring Constant of the Membrane
L	Geometrical Resonator/Cavity Length
L_{air}	Membrane Deflection in Air
$L_{\mathrm{DBR,b}}$	Penetration Depth into the Bottom DBR
$L_{\mathrm{DBR,t}}$	Penetration Depth into the Top DBR
L_{eff}	Geometrical Effective Cavity Length
l_{m}	Length of the Suspension Beam of the Membrane
L_{opt}	Optical Cavity Length
L_{SC}	Optical Length of the Half-VCSEL
m_{e}	Mass of the Electrons

m_{h}	Mass of the Holes
$m_{\mathrm{m,\,eff}}$	Effective Mass of the Membrane
m_{m}	Mass of the Membrane
N	Electron/Carrier Density
n_{H}	Refractive Index of the Optically Denser Quarter-Wave Layer of a DBR Mirror
n_{L}	Refractive Index of the Optically Thinner Quarter-Wave Layer of a DBR Mirror
n_{S}	Refractive Index of Substrates
N_{th}	Threshold Density of Carriers
P_{cav}	Optical Power in the Cavity
P_{dis}	Dissipated Electrical Power
P_{heat}	Joules Heating of the Membrane
P_{in}	Input Electrical Power
P_{noise}	Noise Floor Signal of the Direct Power Detection Photomixing Setup
P_{opt}	Optical Output Power
P_{THz}	THz Signal Power
Q	Quality Factor of the Membrane
$R\,(z)$	Radius of Curvature of the Wavefronts of the Gaussian Beam
$R_{1,2}$	Intensity Reflection Coefficient/Reflectivity of Mirror 1,2
$r_{1,2}$	Amplitude Reflection Coefficient of Mirror 1,2
$R_{\mathrm{DBR,b}}$	Reflectivity of the Plane DBR of a MEMS-VCSEL
$R_{\mathrm{DBR,t}}$	Reflectivity of the Membrane DBR of a MEMS-VCSEL

R_{LIM}	Current Limiting Resistor
R_{MEMS}	Electrical Resistance of the Electrodes of MEMS
R_{th}	Thermal Resistance
s	Dipole Moment of Ag-NWs
T_0	Characteristic Temperature
V	Normalized Frequency Parameter
$V_{1,2}$	Transition Voltage of the Comparator Circuit of Level 1/2
V_{a}	Volume of the Active Region
V_{bias}	DC Bias Voltage
V_{d}	Ideal Diode Voltage/Quasi-Fermi Separation Voltage
V_{err}	Error Voltage of the Wavelength Control Circuit
V_{H}	Positive Saturation Voltage of the Comparator Circuit
V_{LD}	Operating Voltage of a MEMS-VCSEL
V_{L}	Negative Saturation Voltage of the Comparator Circuit
V_{NW}	Volume of the Ag-NW
V_{pp}	Peak-to-Peak Voltage
V_{p}	Volume of the Cavity Mode
w_0	Beam Waist Radius of the Gaussian Beam
w_{m}	Width of the Suspension Beam
x	Membrane Displacement
z_0	Rayleigh Range
1-D	One-Dimensional

2-D	Two-Dimensional
AC	Alternating Current
AOM	Acousto-Optic Modulator
AR	Anti-Reflection
ASE	Amplified Spontaneous Emission
AWG	Arbitrary Waveform Generator
BCB	Benzocyclobutene
BTJ	Buried Tunnel Junction
CW	Continuous-Wave
DAQ	Data Acquisition System
DBR	Distributed Bragg Reflector
DC	Direct Current
DEP	Dielectrophoresis
DFB	Distributed Feedback
DPD	Direct Power Detection
DQE	Differential Quantum Efficiency
DR	Dynamic Range
DSH	Delayed Self-Heterodyne
EC	External-Cavity
EDFA	Erbium-Doped Fiber Amplifier
EEL	Edge-Emitting Laser
ESA	Electrical Spectrum Analyzer

FIB	Focused Ion Beam
FSR	Free Spectral Range
FWHM	Full-Width at Half-Maximum
HCG	High-Contrast Grating
HMD	Homodyne Detection
LDC	Laser Diode Controller
LDV	Laser Doppler Vibrometer
LPD	Linear Power Dissipation
LTG	Low-Temperature-Grown
MEMS	Microelectromechanical System
MMF	Multi-Mode Fiber
MQW	Multi-Quantum Well
NF	Noise Floor
OOR	On-Off Ratio
OSA	Optical Spectrum Analyzer
OSC	Oscilloscope
PC	Polarization Controller
PD	Photodiode
PECVD	Plasma-Enhanced Chemical Vapor Deposition
PM	Polarization-Maintaining
PMF	Polarization-Maintaining Fiber
PSD	Power Spectral Density

QW	Quantum Well
RF	Radio-Frequency
RIN	Relative Intensity Noise
RMS	Root Mean Square
RoC	Radius of Curvature
SC	Semiconductor Cavity
SE	Slope Efficiency
SG-DBR	Sampled Grating Distributed Bragg Reflector
SMF	Single-Mode Fiber
SMSR	Side-Mode-Suppression-Ratio
SOA	Semiconductor Optical Amplifier
TBF	Tunable Band-Pass Filter
TEM	Transverse Electro-Magnetic
VCSEL	Vertical-Cavity Surface-Emitting Laser
WDM	Wavelength-Division Multiplexing
WL	Wavelength Locker

Bibliography

[1] K. Iga. “Vertical-Cavity Surface-Emitting Laser (VCSEL)”. In: *Proceedings of the IEEE* 101.10 (Oct. 2013), pages 2229–2233. DOI: `10.1109/jproc.2013.2275016`.

[2] H. Soda, K. Iga, C. Kitahara, and Y. Suematsu. “GaInAsP/InP Surface Emitting Injection Lasers”. In: *Japanese Journal of Applied Physics* 18.12 (Dec. 1979), pages 2329–2330. DOI: `10.1143/jjap.18.2329`.

[3] F. Koyama, S. Kinoshita, and K. Iga. “Room-temperature continuous wave lasing characteristics of a GaAs vertical cavity surface-emitting laser”. In: *Applied Physics Letters* 55.3 (July 1989), pages 221–222. DOI: `10.1063/1.101913`.

[4] R. P. Schneider, K. D. Choquette, J. A. Lott, K. L. Lear, J. J. Figiel, and K. J. Malloy. “Efficient room-temperature continuous-wave AlGaInP/AlGaAs visible (670 nm) vertical-cavity surface-emitting laser diodes”. In: *IEEE Photonics Technology Letters* 6.3 (Mar. 1994), pages 313–316. DOI: `10.1109/68.275475`.

[5] Y. H. Lee, J. L. Jewell, A. Scherer, S. L. McCall, J. P. Harbison, and L. T. Florez. “Room-temperature continuous-wave vertical-cavity single-quantum-well microlaser diodes”. In: *Electronics Letters* 25.20 (Sept. 1989), pages 1377–1378. DOI: `10.1049/el:19890921`.

[6] M. Müller, W. Hofmann, T. Gründl, M. Horn, P. Wolf, R. D. Nagel, E. Rönneberg, G. Böhm, D. Bimberg, and M.-C. Amann. “1550-nm High-Speed Short-Cavity VCSELs”. In: *IEEE Journal of Selected Topics in Quantum Electronics* 17.5 (Sept. 2011), pages 1158–1166. DOI: `10.1109/jstqe.2011.2109700`.

[7] A. Bachmann, K. Kashani-Shirazi, S. Arafin, and M.-C. Amann. “GaSb-Based VCSEL With Buried Tunnel Junction for Emission Around 2.3 µm”. In: *IEEE Journal of Selected Topics in Quantum Electronics* 15.3 (May 2009), pages 933–940. DOI: `10.1109/jstqe.2009.2013361`.

[8] K. Iga. “Surface-emitting laser-its birth and generation of new optoelectronics field”. In: *IEEE Journal of Selected Topics in Quantum Electronics* 6.6 (Nov. 2000), pages 1201–1215. DOI: `10.1109/2944.902168`.

[9] M.-C. Amann and W. Hofmann. "InP-Based Long-Wavelength VCSELs and VCSEL Arrays". In: *IEEE Journal of Selected Topics in Quantum Electronics* 15.3 (2009), pages 861–868. DOI: `10.1109/jstqe.2009.2013182`.

[10] M. Grabherr. "New applications boost VCSEL quantities: recent developments at Philips". In: *Vertical-Cavity Surface-Emitting Lasers XIX*. Edited by C. Lei and K. D. Choquette. Volume 9381. Proc. SPIE, Mar. 2015, pages 938102–938102–13. DOI: `10.1117/12.2081790`.

[11] J. S. Harris. "Tunable long-wavelength vertical-cavity lasers: the engine of next generation optical networks?" In: *IEEE Journal of Selected Topics in Quantum Electronics* 6.6 (Nov. 2000), pages 1145–1160. DOI: `10.1109/2944.902163`.

[12] C. Gierl, T. Gründl, P. Debernardi, K. Zogal, C. Grasse, H. A. Davani, G. Böhm, S. Jatta, F. Küppers, P. Meißner, and M.-C. Amann. "Surface micromachined tunable 1.55 µm-VCSEL with 102 nm continuous single-mode tuning". In: *Optics Express* 19.18 (Aug. 2011), pages 17336–17343. DOI: `10.1364/oe.19.017336`.

[13] C. Gierl, T. Gründl, P. Debernardi, K. Zogal, H. A. Davani, C. Grasse, G. Böhm, P. Meissner, F. Küppers, and M.-C. Amann. "Surface micromachined MEMS tunable VCSEL at 1550 nm with $>$ 70 nm single mode tuning". In: *Vertical-Cavity Surface-Emitting Lasers XVI*. Edited by C. Lei and K. D. Choquette. Volume 8276. Proceedings of SPIE, Feb. 2012, 82760P–82760P–9. DOI: `10.1117/12.907800`.

[14] M. C. Y. Huang, K. B. Cheng, Y. Zhou, A. P. Pisano, and C. J. Chang-Hasnain. "Monolithic integrated piezoelectric MEMS-tunable VCSEL". In: *IEEE Journal of Selected Topics in Quantum Electronics* 13.2 (Mar. 2007), pages 374–380. DOI: `10.1109/JSTQE.2007.894056`.

[15] G. D. Cole, E. S. Bjorlin, C. S. Wang, N. C. MacDonald, and J. E. Bowers. "Widely tunable bottom-emitting vertical-cavity SOAs". In: *IEEE Photonics Technology Letters* 17.12 (Dec. 2005), pages 2526–2528. DOI: `10.1109/LPT.2005.859157`.

[16] Y. Rao, W. Yang, C. Chase, M. C. Y. Huang, D. P. Worland, S. Khaleghi, M. R. Chitgarha, M. Ziyadi, A. E. Willner, and C. J. Chang-Hasnain. "Long-Wavelength VCSEL Using High-Contrast Grating". In: *IEEE Journal of Selected Topics in Quantum Electronics* 19.4 (July 2013), pages 1701311–1701311. DOI: `10.1109/jstqe.2013.2246780`.

[17] S. Paul, M. T. Haidar, J. Cesar, M. Malekizandi, B. Kögel, C. Neumeyr, M. Ortsiefer, and F. Küppers. "Far-field, linewidth and thermal characteristics of a high-speed 1550-nm MEMS tunable VCSEL". In: *Optics Express* 24.12 (June 2016), pages 13142–13156. DOI: `10.1364/oe.24.013142`.

[18] B. Kögel, H. Halbritter, M. Lackner, M. Schwarzott, M. Maute, M.-C. Amann, F. Winter, and P. Meissner. "Micromechanically Widely Tunable VCSEL for Absorption Spectroscopy at around 1.55 µm". In: *IEEE/LEOS International Conference on Optical MEMS and Their Applications Conference, 2006.* Institute of Electrical and Electronics Engineers (IEEE), 2006, pages 7–8. DOI: `10.1109/omems.2006.1708238`.

[19] B. Kögel, H. Halbritter, S. Jatta, M. Maute, G. Böhm, M.-C. Amann, M. Lackner, M. Schwarzott, F. Winter, and P. Meissner. "Simultaneous Spectroscopy of NH_3 and CO Using a $>$ 50 nm Continuously Tunable MEMS-VCSEL". In: *IEEE Sensors Journal* 7.11 (Nov. 2007), pages 1483–1489. DOI: `10.1109/jsen.2007.907055`.

[20] T. C. Bond, G. D. Cole, L. L. Goddard, and E. M. Behymer. "Photonic MEMS for NIR in-situ Gas Detection and Identification". In: *2007 IEEE Sensors*. Institute of Electrical and Electronics Engineers (IEEE), 2007, pages 1368–1371. DOI: `10.1109/icsens.2007.4388666`.

[21] J. Rausch, P. Heinickel, B. Koegel, K. Zogal, and P. Meissner. "Experimental comparison of piezoresistive MEMS and fiber bragg grating strain sensors". In: *2009 IEEE Sensors*. Institute of Electrical and Electronics Engineers (IEEE), Oct. 2009, pages 1329–1333. DOI: `10.1109/icsens.2009.5398407`.

[22] M. Tonouchi. "Cutting-edge terahertz technology". In: *Nature Photonics* 1.2 (Feb. 2007), pages 97–105. DOI: `10.1038/nphoton.2007.3`.

[23] S. Koenig, D. Lopez-Diaz, J. Antes, F. Boes, R. Henneberger, A. Leuther, A. Tessmann, R. Schmogrow, D. Hillerkuss, R. Palmer, T. Zwick, C. Koos, W. Freude, O. Ambacher, J. Leuthold, and I. Kallfass. "Wireless sub-THz communication system with high data rate". In: *Nature Photonics* 7.12 (Oct. 2013), pages 977–981. DOI: `10.1038/nphoton.2013.275`.

[24] K. A. McIntosh, E. R. Brown, K. B. Nichols, O. B. McMahon, W. F. DiNatale, and T. M. Lyszczarz. "Terahertz photomixing with diode lasers in low-temperature-grown GaAs". In: *Applied Physics Letters* 67.26 (Dec. 1995), pages 3844–3846. DOI: `10.1063/1.115292`.

[25] E. R. Brown, F. W. Smith, and K. A. McIntosh. “Coherent millimeter-wave generation by heterodyne conversion in low-temperature-grown GaAs photoconductors”. In: *Journal of Applied Physics* 73.3 (Feb. 1993), pages 1480–1484. DOI: `10.1063/1.353222`.

[26] H. Ito, F. Nakajima, T. Furuta, and T. Ishibashi. “Continuous THz-wave generation using antenna-integrated uni-travelling-carrier photodiodes”. In: *Semiconductor Science and Technology* 20.7 (June 2005), S191–S198. DOI: `10.1088/0268-1242/20/7/008`.

[27] T. Göbel, D. Stanze, B. Globisch, R. J. B. Dietz, H. Roehle, and M. Schell. “Telecom technology based continuous wave terahertz photomixing system with 105 decibel signal-to-noise ratio and 35 terahertz bandwidth”. In: *Optics Letters* 38.20 (Oct. 2013), pages 4197–4199. DOI: `10.1364/ol.38.004197`.

[28] S. Preu, F. H. Renner, S. Malzer, G. H. Döhler, L. J. Wang, M. Hanson, A. C. Gossard, T. L. J. Wilkinson, and E. R. Brown. “Efficient terahertz emission from ballistic transport enhanced n-i-p-n-i-p superlattice photomixers”. In: *Applied Physics Letters* 90.21 (May 2007), page 212115. DOI: `10.1063/1.2743400`.

[29] E. Rouvalis, C. C. Renaud, D. G. Moodie, M. J. Robertson, and A. J. Seeds. “Traveling-wave Uni-Traveling Carrier Photodiodes for continuous wave THz generation”. In: *Optics Express* 18.11 (May 2010), pages 11105–11110. DOI: `10.1364/oe.18.011105`.

[30] A. J. Deninger, A. Roggenbuck, S. Schindler, and S. Preu. “2.75 THz tuning with a triple-DFB laser system at 1550 nm and InGaAs photomixers”. In: *Journal of Infrared, Millimeter, and Terahertz Waves* 36.3 (Dec. 2014), pages 269–277. DOI: `10.1007/s10762-014-0125-5`.

[31] Y. Jiang, K. Vijayraghavan, S. Jung, F. Demmerle, G. Boehm, M.-C. Amann, and M. A. Belkin. “External cavity terahertz quantum cascade laser sources based on intra-cavity frequency mixing with 1.2–5.9 THz tuning range”. In: *Journal of Optics* 16.9 (Sept. 2014), page 094002. DOI: `10.1088/2040-8978/16/9/094002`.

[32] M. Larson, A. Bhardwaj, W. Xiong, Y. Feng, X. d. Huang, K. Petrov, M. Moewe, H. Ji, A. Semakov, C. Lv, S. Kutty, A. Patwardhan, N. Liu, Z. Li, Y. Bao, Z. Shen, S. Bajwa, F. Zhou, and P. C. Koh. “Narrow linewidth sampled-grating distributed Bragg reflector laser with enhanced side-mode suppression”. In: *Optical Fiber Communication Conference*. The Optical Society, 2015. DOI: `10.1364/ofc.2015.m2d.1`.

[33] Y. Matsui, D. Mahgerefteh, Xueyan Zheng, Xiong Ye, K. McCallion, H. Xu, M. Deutsch, R. Lewén, J. O. Wesström, R. Schatz, and P. J. Rigole. "Widely tuneable modulated grating Y-branch Chirp Managed Laser". In: *2009 35th European Conference on Optical Communication*. Volume 2009-Supplement. 2009, pages 1–2.

[34] S. Paul, C. Gierl, J. Cesar, Q. T. Le, M. Malekizandi, B.Kögel, C. Neumeyr, M. Ortsiefer, and F. Küppers. "10-Gb/s Direct Modulation of Widely Tunable 1550-nm MEMS VCSEL". In: *IEEE Journal of Selected Topics in Quantum Electronics* 21.6 (Nov. 2015), pages 436–443. DOI: `10.1109/jstqe.2015.2418218`.

[35] TOPTICA Photonics. *DFB pro: Distributed-feedback laser*. 2017. URL: `http://www.toptica.com/products/tunable-diode-lasers/ecdl-dfb-lasers/dfb-pro/` (visited on 06/15/2017).

[36] M. T. Haidar, S. Preu, S. Paul, C. Gierl, J. Cesar, A. Emsia, and F. Küppers. "Widely tunable telecom MEMS-VCSEL for terahertz photomixing". In: *Optics Letters* 40.19 (Sept. 2015), pages 4428–4431. DOI: `10.1364/ol.40.004428`.

[37] S. Al-Daffaie, O. Yilmazoglu, F. Küppers, and H. L. Hartnagel. "1-D and 2-D Nanocontacts for Reliable and Efficient Terahertz Photomixers". In: *IEEE Transactions on Terahertz Science and Technology* 5.3 (May 2015), pages 398–405. DOI: `10.1109/tthz.2015.2399772`.

[38] K. J. Ebeling and R. Michalzik. *Lecture notes on Optoelectronic Communication Technology*. Institute of Optoelectronics, Ulm University, summer term, pages 110–114. 2009.

[39] R. Michalzik. *"VCSEL Fundamentals"*, Chapter 2 in *VCSELs-Fundamentals, Technology and Applications of Vertical-Cavity Surface-Emitting Lasers*. Edited by R. Michalzik. Berlin: Springer-Verlag, 2013. DOI: `10.1007/978-3-642-24986-0`.

[40] S. W. Corzine, R. S. Geels, J. W. Scott, R. H. Yan, and L. A. Coldren. "Design of Fabry-Perot surface-emitting lasers with a periodic gain structure". In: *IEEE Journal of Quantum Electronics* 25.6 (June 1989), pages 1513–1524. DOI: `10.1109/3.29288`.

[41] S. W. Corzine, R. H. Yan, and L. A. Coldren. "A tanh substitution technique for the analysis of abrupt and graded interface multilayer dielectric stacks". In: *IEEE Journal of Quantum Electronics* 27.9 (1991), pages 2086–2090. DOI: `10.1109/3.135163`.

[42] D. I. Babic and S. W. Corzine. "Analytic expressions for the reflection delay, penetration depth, and absorptance of quarter-wave dielectric mirrors". In: *IEEE Journal of Quantum Electronics* 28.2 (1992), pages 514–524. DOI: `10.1109/3.123281`.

[43] L. A. Coldren and S. W. Corzine. *Diode Lasers and Photonic Integrated Circuits*. Edited by K. Chang. John Wiley & Sons, Inc., 1995. ISBN: 0–471–11875–3.

[44] P. P. Baveja, B. Kögel, P. Westbergh, J. S. Gustavsson, Å. Haglund, D. N. Maywar, G. P. Agrawal, and A. Larsson. "Assessment of VCSEL thermal rollover mechanisms from measurements and empirical modeling". In: *Optics Express* 19.16 (July 2011), pages 15490–15505. DOI: `10.1364/oe.19.015490`.

[45] D. Derickson. *Fiber Optic Test and Measurement*. PRENTICE HALL, Oct. 11, 1997. 642 pages. ISBN: 0135343305.

[46] T. Okoshi, K. Kikuchi, and A. Nakayama. "Novel method for high resolution measurement of laser output spectrum". In: *Electronics Letters* 16.16 (1980), page 630. DOI: `10.1049/el:19800437`.

[47] C. H. Henry. "Theory of the linewidth of semiconductor lasers". In: *IEEE Journal of Quantum Electronics* 18.2 (Feb. 1982), pages 259–264. DOI: `10.1109/jqe.1982.1071522`.

[48] K. Kikuchi. "Effect of 1/f-type FM noise on semiconductor-laser linewidth residual in high-power limit". In: *IEEE Journal of Quantum Electronics* 25.4 (Apr. 1989), pages 684–688. DOI: `10.1109/3.17331`.

[49] L. B. Mercer. "1/f frequency noise effects on self-heterodyne linewidth measurements". In: *Journal of Lightwave Technology* 9.4 (Apr. 1991), pages 485–493. DOI: `10.1109/50.76663`.

[50] N. Hodgson and H. Weber. *Optical Resonators: Fundamentals, Advanced Concepts and Applications*. Springer, 1997.

[51] B. E. A. Saleh and M. C. Teich. *Fundamentals of Photonics*. John Wiley & Sons, Inc., Apr. 11, 2007. 1200 pages. ISBN: 978-0-471-35832-9.

[52] I. Suemune. "Theoretical study of differential gain in strained quantum well structures". In: *IEEE Journal of Quantum Electronics* 27.5 (May 1991), pages 1149–1159. DOI: `10.1109/3.83371`.

[53] W. Hofmann. "High-Speed Buried Tunnel Junction Vertical-Cavity Surface-Emitting Lasers". In: *IEEE Photonics Journal* 2.5 (Oct. 2010), pages 802–815. DOI: `10.1109/jphot.2010.2055554`.

[54] S. Arafin, A. Bachmann, and M.-C. Amann. “Transverse-Mode Characteristics of GaSb-Based VCSELs With Buried-Tunnel Junctions”. In: *IEEE Journal of Selected Topics in Quantum Electronics* 17.6 (Nov. 2011), pages 1576–1583. DOI: `10.1109/jstqe.2011.2107571`.

[55] G R. Hadley, K. L. Lear, M. E. Warren, K. D. Choquette, J. W. Scott, and S. W. Corzine. “Comprehensive numerical modeling of vertical-cavity surface-emitting lasers”. In: *IEEE Journal of Quantum Electronics* 32.4 (Apr. 1996), pages 607–616. DOI: `10.1109/3.488833`.

[56] M. Ortsiefer, S. Baydar, K. Windhorn, G. Böhm, J. Rosskopf, R. Shau, E. Ronneberg, W. Hofmann, and M.-C. Amann. “2.5-mW single-mode operation of 1.55-µm buried tunnel junction VCSELs”. In: *IEEE Photonics Technology Letters* 17.8 (Aug. 2005), pages 1596–1598. DOI: `10.1109/lpt.2005.850905`.

[57] C. Grasse, M. Müller, G. Böhm, R. Enzmann, Y. Xu, M. Görblich, R. Meyer, M. Ortsiefer, and M.-C. Amann. “Planarization of overgrown tunnel junctions for InP-based VCSEL by MOVPE”. In: *European MOVPE Workshop*. 2009.

[58] C. Gierl. “Mikromechanisch weit abstimmbare Oberflächen-emittierende Laser mit Vertikalresonator”. Ph.D. dissertation. Technische Universität Darmstadt, Fachbereich Elektrotechnik und Informationstechnik, 2012.

[59] S. Jatta. “Plasmaunterstützende Abscheidung von dielektrischen Schichten zur Entwicklung von mikromechanisch abstimmbaren optischen Komponenten”. Ph.D. dissertation. Technische Universität Darmstadt, Fachbereich Elektrotechnik, 2010.

[60] P. Tayebati, P. Wang, D. Vakhshoori, C. C. Lu, M. Azimi, and R. N. Sacks. “Half-symmetric cavity tunable microelectromechanical VCSEL with single spatial mode”. In: *IEEE Photonics Technology Letters* 10.12 (Dec. 1998), pages 1679–1681. DOI: `10.1109/68.730467`.

[61] G. D. Cole, E. S. Bjorlin, Q. Chen, C. Y. Chan, S. Wu, C. S. Wang, N. C. MacDonald, and J. E. Bowers. “MEMS-tunable vertical-cavity SOAs”. In: *IEEE Journal of Quantum Electronics* 41.3 (Mar. 2005), pages 390–407. DOI: `10.1109/jqe.2004.841496`.

[62] P. Debernardi, B. Kögel, K. Zogal, P. Meissner, M. Maute, M. Ortsiefer, G. Böhm, and M.-C. Amann. “Modal Properties of Long-Wavelength Tunable MEMS-VCSELs With Curved Mirrors: Comparison of Experiment and Modeling”. In: *IEEE Journal of Quantum Electronics* 44.4 (Apr. 2008), pages 391–399. DOI: `10.1109/jqe.2007.914773`.

[63] M. C. Larson. “Microelectromechanical wavelength-tunable vertical-cavity light emitters and lasers”. Ph.D. dissertation. Stanford University, 1996.

[64] B. Kögel, M. Maute, H. Halbritter, F. Riemenschneider, G. Böhm, M.-C. Amann, and P. Meissner. “Long-wavelength MEMS tunable vertical-cavity surface-emitting lasers with high sidemode suppression”. In: *Journal of Optics A: Pure and Applied Optics* 8.7 (June 2006), S370–S376. DOI: `10.1088/1464-4258/8/7/s13`.

[65] C. Gierl, T. Gründl, S. Paul, K. Zogal, M. T. Haidar, P. Meissner, M.-C. Amann, and F. Küppers. “Temperature characteristics of surface micromachined MEMS-VCSEL with large tuning range”. In: *Optics Express* 22.11 (May 2014), pages 13063–13072. DOI: `10.1364/oe.22.013063`.

[66] R. S. Tucker, D. M. Baney, W. V. Sorin, and C. A. Flory. “Thermal noise and radiation pressure in MEMS Fabry-Pérot tunable filters and lasers”. In: *IEEE Journal of Selected Topics in Quantum Electronics* 8.1 (2002), pages 88–97. DOI: `10.1109/2944.991403`.

[67] C. Chen, P. O. Leisher, A. A. Allerman, K. M. Geib, and K. D. Choquette. “Temperature Analysis of Threshold Current in Infrared Vertical-Cavity Surface-Emitting Lasers”. In: *IEEE Journal of Quantum Electronics* 42.10 (Oct. 2006), pages 1078–1083. DOI: `10.1109/jqe.2006.881828`.

[68] B. Kögel, H. Halbritter, M. Maute, G. Böhm, M.-C. Amann, and P. Meissner. “Singlemode and Polarization Stable MEMS-VCSEL with Broadband Tuning Characteristics around 1.55 µm”. In: *2006 European Conference on Optical Communications*. Institute of Electrical and Electronics Engineers (IEEE), Sept. 2006. DOI: `10.1109/ecoc.2006.4801075`.

[69] T. B. Gabrielson. “Mechanical-thermal noise in micromachined acoustic and vibration sensors”. In: *IEEE Transactions on Electron Devices* 40.5 (May 1993), pages 903–909. DOI: `10.1109/16.210197`.

[70] B. Kögel, K. Zogal, S. Jatta, C. Grasse, M.-C. Amann, G. Cole, M. Lackner, M. Schwarzott, F. Winter, and P. Meissner. “Micromachined tunable vertical-cavity surface-emitting lasers with narrow linewidth for near infrared gas detection”. In: *Proceedings of SPIE*. Volume 7266. Nov. 2008, 72660O–72660O–6. DOI: `10.1117/12.816272`.

[71] G. M. Rebeiz. *RF MEMS: Theory, Design, and Technology*. John Wiley & Sons, Inc., Feb. 11, 2003. 512 pages. ISBN: 0471201693.

[72] T. J. Kippenberg and K. J. Vahala. “Cavity Optomechanics: Back-Action at the Mesoscale”. In: *Science* 321.5893 (Aug. 2008), pages 1172–1176. DOI: `10.1126/science.1156032`.

[73] W. Yang, S. A. Gerke, K. W. Ng, Y. Rao, C. Chase, and C. J. Chang-Hasnain. "Laser optomechanics". In: *Scientific Reports* 5 (Sept. 2015), page 13700. DOI: `10.1038/srep13700`.

[74] W. M. Siebert. *Circuits, Signals, and Systems*. MIT PR, Sept. 11, 1985. 672 pages. ISBN: 0262690950.

[75] J. R. Vig and Y. Kim. "Noise in microelectromechanical system resonators". In: *IEEE Transactions on Ultrasonics, Ferroelectrics and Frequency Control* 46.6 (Nov. 1999), pages 1558–1565. DOI: `10.1109/58.808881`.

[76] F. Mohd-Yasin, D. J. Nagel, and C. E. Korman. "Noise in MEMS". In: *Measurement Science and Technology* 21.1 (Nov. 2009), page 012001. DOI: `10.1088/0957-0233/21/1/012001`.

[77] H. Halbritter, C. Sydlo, B. Kögel, F. Riemenschneider, H. L. Hartnagel, and P. Meissner. "Impact of Micromechanics on the Linewidth and Chirp Performance of MEMS-VCSELs". In: *IEEE Journal of Selected Topics in Quantum Electronics* 13.2 (2007), pages 367–373. DOI: `10.1109/jstqe.2007.894062`.

[78] D. Huber, P. Corredoura, S. Lester, V. Robbins, and L. Kamas. "Reducing Brownian Motion in an Electrostatically Tunable MEMS Laser". In: *Journal of Microelectromechanical Systems* 13.5 (Oct. 2004), pages 732–736. DOI: `10.1109/jmems.2004.836290`.

[79] Y. Zhao, M. Mao, R. Horowitz, A. Majumdar, J. Varesi, P. Norton, and J. Kitching. "Optomechanical uncooled infrared imaging system: design, microfabrication, and performance". In: *Journal of Microelectromechanical Systems* 11.2 (2002), pages 136–146. DOI: `10.1109/84.993448`.

[80] H. Halbritter, F. Riemenschneider, B. Kögel, E. Feldmeier, and P. Meissner. "Optical channel switching algorithm for continuously tunable lasers". In: *Electronics Letters* 40.24 (2004), page 1536. DOI: `10.1049/el:20047039`.

[81] S. Schilt, K. Zogal, B. Kögel, P. Meissner, M. Maute, R. Protasio, and M.-C. Amann. "Spectral and modulation properties of a largely tunable MEMS-VCSEL in view of gas phase spectroscopy applications". In: *Applied Physics B* 100.2 (Feb. 2010), pages 321–329. DOI: `10.1007/s00340-010-3898-9`.

[82] A. S. Pine, R. D. Suenram, E. R. Brown, and K. A. McIntosh. "A Terahertz Photomixing Spectrometer: Application to SO_2 Self Broadening". In: *Journal of Molecular Spectroscopy* 175.1 (Jan. 1996), pages 37–47. DOI: `10.1006/jmsp.1996.0006`.

[83] Y. C. Chung and Y. H. Lee. "Spectral characteristics of vertical-cavity surface-emitting lasers with external optical feedback". In: *IEEE Photonics Technology Letters* 3.7 (July 1991), pages 597–599. DOI: `10.1109/68.87925`.

[84] D. D. John, C. B. Burgner, B. Potsaid, M. E. Robertson, B. K. Lee, W. J. Choi, A. E. Cable, J. G. Fujimoto, and V. Jayaraman. “Wideband Electrically Pumped 1050-nm MEMS-Tunable VCSEL for Ophthalmic Imaging”. In: *Journal of Lightwave Technology* 33.16 (Aug. 2015), pages 3461–3468. DOI: `10.1109/jlt.2015.2397860`.

[85] A. L. Schawlow and C. H. Townes. “Infrared and Optical Masers”. In: *Physical Review* 112.6 (Dec. 1958), pages 1940–1949. DOI: `10.1103/physrev.112.1940`.

[86] S. Preu, G. H. Döhler, S. Malzer, L. J. Wang, and A. C. Gossard. “Tunable, continuous-wave Terahertz photomixer sources and applications”. In: *Journal of Applied Physics* 109.6 (Mar. 2011), page 061301. DOI: `10.1063/1.3552291`.

[87] M. Tani, O. Morikawa, S. Matsuura, and M. Hangyo. “Generation of terahertz radiation by photomixing with dual- and multiple-mode lasers”. In: *Semiconductor Science and Technology* 20.7 (June 2005), S151–S163. DOI: `10.1088/0268-1242/20/7/005`.

[88] E. R. Brown. “THz Generation by Photomixing in Ultrafast Photoconductors”. In: *International Journal of High Speed Electronics and Systems* 13.02 (June 2003), pages 497–545. DOI: `10.1142/s0129156403001818`.

[89] A. Semenov, O. Cojocari, H. W. Hübers, F. Song, A. Klushin, and A. S. Müller. “Application of Zero-Bias Quasi-Optical Schottky-Diode Detectors for Monitoring Short-Pulse and Weak Terahertz Radiation”. In: *IEEE Electron Device Letters* 31.7 (2010), pages 674–676. DOI: `10.1109/led.2010.2048192`.

[90] A. Roggenbuck, H. Schmitz, A. Deninger, I. C. Mayorga, J. Hemberger, R. Güsten, and M. Grüninger. “Coherent broadband continuous-wave terahertz spectroscopy on solid-state samples”. In: *New Journal of Physics* 12.4 (Apr. 2010), page 043017. DOI: `10.1088/1367-2630/12/4/043017`.

[91] D. M. Slocum, E. J. Slingerland, R. H. Giles, and T. M. Goyette. “Atmospheric absorption of terahertz radiation and water vapor continuum effects”. In: *Journal of Quantitative Spectroscopy and Radiative Transfer* 127 (Sept. 2013), pages 49–63. DOI: `10.1016/j.jqsrt.2013.04.022`.

[92] Y. Xia, P. Yang, Y. Sun, Y. Wu, B. Mayers, B. Gates, Y. Yin, F. Kim, and H. Yan. “One-Dimensional Nanostructures: Synthesis, Characterization, and Applications”. In: *Advanced Materials* 15.5 (Mar. 2003), pages 353–389. DOI: `10.1002/adma.200390087`.

[93] M. E. Toimil Molares, A. G. Balogh, T. W. Cornelius, R. Neumann, and C. Trautmann. “Fragmentation of nanowires driven by Rayleigh instability”. In: *Applied Physics Letters* 85.22 (Nov. 2004), pages 5337–5339. DOI: `10.1063/1.1826237`.

[94] N. Silvis-Cividjian, C. W. Hagen, P. Kruit, M. A. J. v.d. Stam, and H. B. Groen. "Direct fabrication of nanowires in an electron microscope". In: *Applied Physics Letters* 82.20 (May 2003), pages 3514–3516. DOI: `10.1063/1.1575506`.

[95] R. DuHamel and D. Isbell. "Broadband logarithmically periodic antenna structures". In: *IRE International Convention Record*. Volume 5. Institute of Electrical and Electronics Engineers (IEEE), Mar. 1957, pages 119–128. DOI: `10.1109/irecon.1957.1150566`.

[96] A W. Maijenburg, M. G. Maas, E. J. B. Rodijk, W. Ahmed, E. S. Kooij, E. T. Carlen, D. H. A. Blank, and J. E. ten Elshof. "Dielectrophoretic alignment of metal and metal oxide nanowires and nanotubes: A universal set of parameters for bridging prepatterned microelectrodes". In: *Journal of Colloid and Interface Science* 355.2 (Mar. 2011), pages 486–493. DOI: `10.1016/j.jcis.2010.12.011`.

[97] H. A. Pohl. "The Motion and Precipitation of Suspensoids in Divergent Electric Fields". In: *Journal of Applied Physics* 22.7 (July 1951), pages 869–871. DOI: `10.1063/1.1700065`.

[98] R. Pethig. "Review Article—Dielectrophoresis: Status of the theory, technology, and applications". In: *Biomicrofluidics* 4.2 (June 2010), page 022811. DOI: `10.1063/1.3456626`.

[99] J. J. Boote and S. D. Evans. "Dielectrophoretic manipulation and electrical characterization of gold nanowires". In: *Nanotechnology* 16.9 (June 2005), pages 1500–1505. DOI: `10.1088/0957-4484/16/9/015`.

[100] M. Dimaki and P. Bøggild. "Dielectrophoresis of carbon nanotubes using microelectrodes: a numerical study". In: *Nanotechnology* 15.8 (June 2004), pages 1095–1102. DOI: `10.1088/0957-4484/15/8/039`.

[101] W. Ahmed, E. S. Kooij, A. van Silfhout, and B. Poelsema. "Quantitative Analysis of Gold Nanorod Alignment after Electric Field-Assisted Deposition". In: *Nano Letters* 9.11 (Nov. 2009), pages 3786–3794. DOI: `10.1021/nl901968e`.

[102] H. Morgan and N. G. Green. "Dielectrophoretic manipulation of rod-shaped viral particles". In: *Journal of Electrostatics* 42.3 (Dec. 1997), pages 279–293. DOI: `10.1016/s0304-3886(97)00159-9`.

[103] R. H. M. Chan, C. K. M. Fung, and W. J. Li. "Rapid assembly of carbon nanotubes for nanosensing by dielectrophoretic force". In: *Nanotechnology* 15.10 (Aug. 2004), S672–S677. DOI: `10.1088/0957-4484/15/10/028`.

[104] Y. Liu, J. H. Chung, W. K. Liu, and R. S. Ruoff. "Dielectrophoretic Assembly of Nanowires". In: *The Journal of Physical Chemistry B* 110.29 (July 2006), pages 14098–14106. DOI: `10.1021/jp061367e`.

[105] C. Celle, C. Mayousse, E. Moreau, H. Basti, A. Carella, and J. P. Simonato. "Highly flexible transparent film heaters based on random networks of silver nanowires". In: *Nano Research* 5.6 (May 2012), pages 427–433. DOI: `10.1007/s12274-012-0225-2`.

[106] M. T. Haidar, S. Al-Daffaie, O. Yilmazoglu, A. S. Hajo, and F. Küppers. "CW THz photomixers at 850 nm and 1550 nm using dielectrophoretic alignment of Ag-nanowire". In: *2016 41st International Conference on Infrared, Millimeter, and Terahertz waves (IRMMW-THz)*. Institute of Electrical and Electronics Engineers (IEEE), Sept. 2016. DOI: `10.1109/irmmw-thz.2016.7758754`.

[107] M. R. Kaspers, A. M. Bernhart, F. J. Meyer zu Heringdorf, G. Dumpich, and R. Möller. "Electromigration and potentiometry measurements of single-crystalline Ag nanowires under UHV conditions". In: *Journal of Physics: Condensed Matter* 21.26 (June 2009), page 265601. DOI: `10.1088/0953-8984/21/26/265601`.

[108] B. Stahlmecke, L. I. Chelaru, F. J. Meyer zu Heringdorf, and G. Dumpich. "Electromigration in Gold and Single Crystalline Silver Nanowires". In: *AIP Conference Proceedings*. AIP Publishing, 2006. DOI: `10.1063/1.2173533`.

[109] R. P. Gupta. "Theory of electromigration in noble and transition metals". In: *Physical Review B* 25.8 (Apr. 1982), pages 5188–5196. DOI: `10.1103/physrevb.25.5188`.

[110] B. Stahlmecke, F. J. Meyer zu Heringdorf, L. I. Chelaru, M. Horn von Hoegen, G. Dumpich, and K. R. Roos. "Electromigration in self-organized single-crystalline silver nanowires". In: *Applied Physics Letters* 88.5 (Jan. 2006), page 053122. DOI: `10.1063/1.2172012`.

[111] J. Plateau. *Statique expérimentale et théorique des liquides soumis aux seules forces moléculaires*. Volume 2. Gauthier-Villars, 1873.

[112] S. Karim, M. E. Toimil-Molares, A. G. Balogh, W. Ensinger, T. W. Cornelius, E. U. Khan, and R. Neumann. "Morphological evolution of Au nanowires controlled by Rayleigh instability". In: *Nanotechnology* 17.24 (Nov. 2006), pages 5954–5959. DOI: `10.1088/0957-4484/17/24/009`.

[113] M. Rauber, F. Muench, M. E. Toimil-Molares, and W. Ensinger. "Thermal stability of electrodeposited platinum nanowires and morphological transformations at elevated temperatures". In: *Nanotechnology* 23.47 (Nov. 2012), page 475710. DOI: `10.1088/0957-4484/23/47/475710`.

[114] B. J. Inkson, G. Dehm, and Y. Peng. "Dynamical growth of Cu–Pt nanowires with a nanonecklace morphology". In: *Nanotechnology* 18.41 (Sept. 2007), page 415601. DOI: `10.1088/0957-4484/18/41/415601`.

[115] Lord Rayleigh. “On The Instability Of Jets”. In: *Proceedings of the London Mathematical Society* s1-10.1 (Nov. 1878), pages 4–13. DOI: `10.1112/plms/s1-10.1.4`.

[116] S. Karim, M. E. Toimil-Molares, W. Ensinger, A. G. Balogh, T. W. Cornelius, E. U. Khan, and R. Neumann. “Influence of crystallinity on the Rayleigh instability of gold nanowires”. In: *Journal of Physics D: Applied Physics* 40.12 (June 2007), pages 3767–3770. DOI: `10.1088/0022-3727/40/12/031`.

[117] H. H. Khaligh and I. A. Goldthorpe. “Failure of silver nanowire transparent electrodes under current flow”. In: *Nanoscale Research Letters* 8.1 (2013), page 235. DOI: `10.1186/1556-276x-8-235`.

[118] S. Preu, M. Mittendorff, H. Lu, H. B. Weber, S. Winnerl, and A. C. Gossard. “1550 nm ErAs:In(Al)GaAs large area photoconductive emitters”. In: *Applied Physics Letters* 101.10 (2012), page 101105. DOI: `10.1063/1.4750244`.

Own Publications

Journals

[1] M. T. Haidar, S. Preu, S. Paul, C. Gierl, J. Cesar, A. Emsia, and F. Küppers. "Widely tunable telecom MEMS-VCSEL for terahertz photomixing". In: *Optics Letters* 40.19 (Oct. 2015), pages 4428–4431. DOI: `10.1364/OL.40.004428`.

[2] S. Paul, M. T. Haidar, J. Cesar, M. Malekizandi, B. Kögel, C. Neumeyr, M. Ortsiefer, and F. Küppers. "Far-field, linewidth and thermal characteristics of a high-speed 1550-nm MEMS tunable VCSEL". In: *Optics Express* 24.12 (June 2016), pages 13142–13156.

[3] C. Gierl, T. Gründl, S. Paul, K. Zogal, M. T. Haidar, P. Meissner, M. C. Amann, and F. Küppers. "Temperature characteristics of surface micromachined MEMS-VCSEL with large tuning range". In: *Optics Express* 22.11 (May 2014), pages 13063–13072. DOI: `10.1364/oe.22.013063`.

[4] V. S. Lyubopytov, A. P. Porfirev, S. O. Gurbatov, S. Paul, M. F. Schumann, J. Cesar, M. Malekizandi, M. T. Haidar, M. Wegener, A. Chipouline, and F. Küppers. "Simultaneous wavelength and orbital angular momentum demultiplexing using tunable MEMS-based Fabry-Perot filter". In: *Optics Express* 25.9 (Apr. 2017), pages 9634–9646. DOI: `10.1364/oe.25.009634`.

Conference Proceedings

[1] M. T. Haidar, E. Polat, S. Paul, J. Cesar, C. Gierl, A. Chipouline, and F. Küppers. "SOA-Based Tunable Fiber Ring Laser With Intracavity MEMS-Tunable Fabry-Pérot Filter". In: *Conference on Lasers and Electro-Optics*. The Optical Society, 2016, SM2P.7. DOI: `10.1364/CLEO_SI.2016.SM2P.7`.

[2] M. T. Haidar, S. Paul, C. Gierl, S. Preu, and F. Küppers. "Ultra-broadband telecom MEMS-VCSEL for frequency-tunable terahertz generation with photomixers". In: *2014 39th International Conference on Infrared, Millimeter, and Terahertz waves (IRMMW-THz)*. Institute of Electrical and Electronics Engineers (IEEE), Sept. 2014. DOI: `10.1109/irmmw-thz.2014.6956220`.

[3] S. Paul, J. Cesar, C. Gierl, M. T. Haidar, B. Koegel, C. Neumeyr, M. Ortsiefer, and F. Kueppers. "Ultra wide mode-hop free tuning around 1550-NM telecom wavelength using high-speed MEMS-VCSELS". In: *2015 20th Microoptics Conference (MOC)*. Institute of Electrical and Electronics Engineers (IEEE), Oct. 2015. DOI: `10.1109/moc.2015.7416499`.

[4] A. S. Hajo, S. Al-Daffaie, O. Yilmazoglu, M. T. Haidar, and F. Küppers. "Zero-bias Schottky diode based THz detectors at room temperature using metallic nanowire". In: *2016 41st International Conference on Infrared, Millimeter, and Terahertz waves (IRMMW-THz)*. Institute of Electrical and Electronics Engineers (IEEE), Sept. 2016. DOI: `10.1109/irmmw-thz.2016.7758892`.

[5] M. T. Haidar, S. Al-Daffaie, O. Yilmazoglu, A. S. Hajo, and F. Küppers. "CW THz photomixers at 850 nm and 1550 nm using dielectrophoretic alignment of Ag-nanowire". In: *2016 41st International Conference on Infrared, Millimeter, and Terahertz waves (IRMMW-THz)*. Institute of Electrical and Electronics Engineers (IEEE), Sept. 2016. DOI: `10.1109/irmmw-thz.2016.7758754`.

[6] S. Paul, V. S. Lyubopytov, M. F. Schumann, J. Cesar, M. Malekizandi, M. T. Haidar, A. P. Porfirev, S. O. Gurbatov, M. Wegener, A. Chipouline, and F. Küppers. "Vortex-MEMS filters for wavelength-selective orbital-angular-momentum beam generation". In: *Complex Light and Optical Forces XI*. Edited by D. L. Andrews, E. J. Galvez, and J. Glückstad. Volume 10120. Proceedings of SPIE, Feb. 2017, 101200G–101200G–13. DOI: `10.1117/12.2252494`.

[7] J. Cesar, S. Paul, Mohammad T. Haidar, B. Corbett, A. Chipouline, and F. Küppers. "Surface Micromachined MEMS-Tunable PIN-Photodiodes around 1550-nm". In: *Conference on Lasers and Electro-Optics*. Optical Society of America, 2017, STu1N.7. DOI: `10.1364/CLEO_SI.2017.STu1N.7`.

[8] S. Paul, J. Cesar, M. Malekizandi, M. T. Haidar, N. Heermeier, M. Ortsiefer, C. Neumeyr, C. Gréus, M. H. Eiselt, I. Ibrahim, H. Schmidt, J. Schmidt, and F. Küppers. "Towards a SFP+ module for WDM applications using an ultra-widely-tunable high-speed MEMS-VCSEL". In: *Vertical-Cavity Surface-Emitting Lasers XXI*. Edited by K. D. Choquette and C. Lei. Volume 10122. Proceedings of SPIE, Feb. 2017, pages 1012209–1012209–9. DOI: `10.1117/12.2252059`.

Academic Supervisions

- E. Polat, “Wavelength tunable fiber ring laser with integrated MEMS-tunable Fabry-Pérot filter,” Bachelor Thesis **St 2227-B**, (2014).
- V. Roskin, “Linewidth measurement of MEMS-VCSEL at 1550 nm wavelength,” Bachelor Thesis **St 2244-B**, (2015).

Curriculum Vitae

Personal Data

Name: Mohammad Tanvir Haidar
Date of Birth: 12. December 1981
Place of Birth: Gopalganj, Bangladesh

Education

1986–1991 – Sarnakali School, Gopalganj
1991–1994 – Government High School, Pirojpur
1994–1998 – Barisal Cadet College (Secondary School Certificate)
1998–2000 – Barisal Cadet College (Higher Secondary Certificate)
2001–2006 – Bachelor of Science in Electrical & Electronic Engineering (B.Sc.), Bangladesh University of Engineering & Technology (BUET)
2008–2010 – Master of Science in Communications Technology (M.Sc.), Ulm University

Employment

2006–2008 – Fixed-Network Engineer, Alcatel-Lucent Bangladesh
2010–2011 – Graduate Research Assistant, Institute of Optoelectronics, Ulm University

2011–2012 –	Development Engineer, OSRAM Opto Semiconductors GmbH, Regensburg
2012–2013 –	Radio-Frequency (RF) Engineer, SinePulse GmbH, Munich
2013–2016 –	Scientific Employee, Institute for Microwave Engineering & Photonics, Technical University of Darmstadt

Weiterstadt, 21.06.2017